EXPLORING ELECTRODE MICROSTRUCTURAL IMPACT ON LITHIUM-AIR BATTERY PERFORMANCE

A Thesis

by

DICKENS LAW

Submitted to the Office of Graduate and Professional Studies of
Texas A&M University
in partial fulfillment of the requirements for the degree of

MASTER OF SCIENCE

Chair of Committee,	Partha P. Mukherjee
Committee Members,	Sarbajit Banerjee
	Hong Liang
Head of Department,	Andreas A. Polycarpou

May 2017

Major Subject: Mechanical Engineering

ABSTRACT

With diminishing fuel reserves, the world is facing quite a dire situation in terms of satisfying global energy demands in the near future. Electrochemical energy storage is going to be an essential part of this solution due to its inherently large efficiency (much higher than Carnot limit of heat – to – work conversion) and sufficiently good reversibility. These electrochemical storage devices have to match the present day fuel economy of gasoline engines for them to present an affordable and realistic solution. Lithium air chemistry is a strong contender to replace internal combustion engines due to their very high energy density (quite comparable to IC engines).

Here one of the reactants – oxygen is freely available from atmosphere and thus possess no storage needs. For Li-air cells using organic electrolyte, Li ions react with oxygen and produce insoluble lithium peroxide (Li_2O_2). Li_2O_2 being an electronic insulator, covers the electrochemically active surface of cathode and leads to cell shutdown. Alternatively, the oxygen transport from atmosphere to reaction sites could be slow enough to support desired rate of electrochemical reaction. One direction of improvement is to control morphological features of these precipitates prevent them from covering the reaction surface. On the other hand, electrode microstructure could be played with to prolong time to cell shutdown.

The electrochemical behavior of a Li-air cell is modeled using species and charge conservation. Different performance limiting modes, i.e., surface passivation and oxygen starvation, are identified. The surface passivation limits are characterized from previous

experimental studies. Various cathode architectures are realized using stochastic regeneration for different mean pore size and initial porosity. They are further abstracted in terms of porous media properties and used during electrochemical simulations. The simulations explore the effects of discharge rates, microstructural properties, separator and cathode dimensions.

ACKNOWLEDGEMENTS

CONTRIBUTORS AND FUNDING SOURCES

Contributors

Part 1, faculty committee recognition

This work was supervised by a thesis (or) dissertation committee consisting of Professor Partha Mukherjee and Professor Hong Liang of the Department of Mechanical Engineering and Professor Sarbajit of the Department of Chemistry.

Part 2, student/collaborator contributions

The electrochemical discharge code and precipitation addition code analyzed for Chapter 3 was provided by Aashutosh Mistry.

All other work conducted for the thesis (or) dissertation was completed by the student independently.

Funding Sources

TABLE OF CONTENTS

LIST OF FIGURES

LIST OF TABLES

1 INTRODUCTION

The Paris Climate Conference in December 2015 marked a turning point in modern history on the issue of climate change. The conference, amended by 195 countries, aimed to keep the increase of global temperature below 2˚C above pre-industrial level and limit temperature increase to reduce impact of climate change. The conference is crucial, as environmental consequences from previous decades of irresponsible consumption of fossil fuel base energy are beginning to show. The on-going drought in California and major hurricane seen in south eastern United States are amongst the few environmental consequence of irresponsible energy consumption.

Lawrence Livermore National Laboratory published an energy flowchart on US energy consumption in 2015 [1]. The most notable result from this flow chart is the energy dedicated and wasted in the transportation sector. Petroleum consumption for transportation sector of US is about 27.7 quad, however, only 6.74 quad is actually utilized in energy services. The remaining energy is wasted through inefficiency or frictional loss. It is clear that the need to transform energy consumption is apparent.

In recent year, the automotive industry rises to the challenge by creating more energy efficient vehicles such as hybrid vehicle, PEM fuel cell, and full electric vehicle. While hybrid and PEM fuel cell vehicle offer a more energy conscious solution, the vehicles still rely heavily on an energy intense infrastructure. PEM fuel cell would significantly reduce petroleum dependence on the transportation, but the energy requires

to maintain hydrogen and oxygen in pressurized form will outweigh the benefit. The idea, then, is reducing the necessary steps to store and utilize energy.

Lithium based secondary (rechargeable) battery is the next evolution to energy utilization and storage. Secondary battery is evolutionary due to its ability to recharge at existing electric grid and its ability to retain energy. The combined benefits allow for a mobile energy storage system that is highly energy efficient and infrastructure independent. In order to replace petroleum as a primary energy source, the secondary batteries must offer similar performances to cause considerable shift in consumer opinion. The amount of energy which a battery can hold can be defined as,

$$E = V \times q \tag{1},$$

where V represents voltage and q represents charge [2]. The idea, then, is to create a battery system that is high in voltage and high in charge capacity. Amalraj et al. created a road map for material selection within a battery system [3].

Li metal high specific capacity makes it an attractive anode material, while O_2 high potential makes it an attractive cathode material. The combination of the two materials creates a high energy battery system. O_2 as a cathode material is interesting due to its availability from air, and as such reduces the need to store active material within the battery system [4]. The reduction in mass allows a battery system to attain high energy density property. Girishkumar et al. created a chart comparing the theoretical and practical energy density of different battery types with gasoline. Li-air battery and gasoline are comparable to one another by their theoretical energy density [5].

The problem with gasoline's practical energy density, however, lies on the vehicle's tank to wheel. The average tank-to-wheel efficiency of US vehicle fleet is about 12.6%, which reduces the practical energy density to 1700 Wh/kg [6]. The practical energy for Li-air was evaluated to be the same as the practical energy of gasoline. While the estimation seem arbitrary, Girishkumar et al. justify the 14.5% energy density retention for Li-air is plausible as the leading Zn-air battery is able to retain 40 ~ 50% of its theoretical energy density [5]. The skeptical assessment suggests the plausibility of Li-air to outperform gasoline with slight improvement. These gradual improvements will increase public acceptance toward the transition of alternative energy storage method. The benefit of Li-air battery is clear, however, the systems themselves are still in development and multiple issues still plague the systems from being fully operational.

1.1 Li-air electrochemical reaction

The early consensus of Lithium-air primary discharge product were mixed. The basic assumption is electrochemical reaction between lithium metal and O_2 will yield a form of stoichiometrically balanced product. The conflict in consensus began with 2 sets of electrochemical reactions that are stoichiometrically balanced [7]:

$$2Li^+ + O_2 + 2e^- \rightarrow Li_2O_2 \qquad E^\circ = 3.10 \text{ V} \tag{2}$$

$$4Li^+ + O_2 + 4e^- \rightarrow 2Li_2O \qquad E^\circ = 2.91 \text{ V} \tag{3}$$
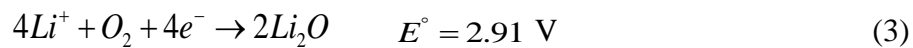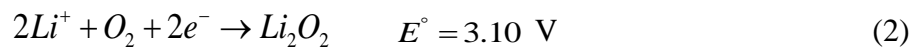
These two stoichiometrically balanced electrochemical reaction was first introduced from Abraham et al [8]. The open circuit potential (Eº) were calculated from Gibbs free energy. Li_2O was calculated with a Gibbs free energy of -134 kcal/mol and Li_2O_2 was calculated with a Gibbs free energy of -145 kcal/mol. Abraham's group created two sets of battery, one is exposed to ambient laboratory air and the other one is exposed to a flowing O_2 atmosphere.

Two distinctive differences can be observed between the two battery types, the difference between open circuit voltage, and specific discharge capacity. The Nernst equation, equation 4, dictates concentration influences the open circuit voltage of a cell [9].

$$\Delta \varepsilon_0 = \Delta \varepsilon_0^o + \frac{R \cdot T}{z \cdot F} \ln \left(\frac{C}{C_{ref}} \right) \tag{4}$$

The discrepancy of specific discharge capacity between flowing O_2 atmosphere and ambient laboratory air could attribute to foreign particle within air that help facilitate transport within the cell. The alternate theory is the final product formed for flowing O_2 atmosphere reaction is different than the final product formed for ambient laboratory air. The group, however, proves the final product form to be Li_2O_2.

Abraham et al conducted two sets of test that indicated the final discharge product from both sets of battery to be Li_2O_2 [8]. The first test involves mixing carbon electrode containing discharge product with $KMnO_4$ solution. The group observed when Li_2O_2 was mixed with $KMnO_4$ solution, the solution's purple color will disappear with evolution of

a gas [8]. The discharged carbon electrode was observed to have color change much similar to result of mixing Li_2O_2 to $KMnO_4$. The same phenomenon, however, cannot be observed when $KMnO_4$ solution was mixed with Li_2O or an undischarged electrode. This result is important because it established two fundamental relationships:

1. The un-discharged carbon electrode is not responsible for the change in color of KMnO4 solution

2. Li_2O_2 is solely responsible for the change of color to $KMnO_4$, and component with similar chemical makeup but different stoichiometry will not trigger color change with the solution

The second test involve the use of Raman spectroscopy. The discharge carbon electrode had a notable absorption peak at 795 cm^{-1}. This absorption peak is a known characteristics of O - O stretching in Li_2O_2 as opposed to Li_2O absorption peak of 521 cm^{-1} [10]. The finding is profound for lithium air as researcher can narrow their scope on the development of the battery system to maximize Li_2O_2 formation within the cell.

1.2 Li-air battery system

The conventional understanding of a battery system is composing of negative electrode, separator/electrolyte, and positive electrode [11]. The situation for Li-air battery, however, is far from conventional. Since Li-air battery is open to atmosphere, interaction between water moisture and lithium metal causes a parasitic corrosion [12].

The same concern applies to electrolyte employ within the battery. This created a situation where electrolytes and concern for lithium corrosion dictates the design of battery systems. This resulted in four different configurations of battery system: non-aqueous (aprotic), aqueous, hybrid (non-aqueous/aqueous), and solid-state electrolyte system. Non-aqueous electrolyte system is much similar to conventional battery and is composing of lithium metal anode, organic electrolyte, and a porous carbon based cathode. Aqueous electrolyte system separates lithium and aqueous electrolyte via Li-ion conducting ceramic film (ie. LiSICON). The film is particularly important due to its ability to prevent aqueous electrolyte from interacting with lithium metal directly and facilitate the transport of Li^+ ion. Hybrid electrolyte system is a combination of non-aqueous electrolyte and aqueous electrolyte system. Solid electrolyte separator separates organic electrolyte and aqueous electrolyte. The solid electrolyte separator also prevents water vapor from aqueous electrolyte to diffuse to lithium metal. Solid state electrolyte system employ solid electrolytes, inorganic ceramic or organic polymer, which is able to facilitate Li+ ion and prevent water vapor diffusion [13].

1.2.1   Non-aqueous electrolyte system

Non-aqueous electrolyte species reduce the need of complex procedures to produce cells, however, stability of non-aqueous organic electrolytes are not guaranteed. Muhammed et al. suggested that during discharge, carbon electrode in dimethyl

sulphoxide (DMSO) or tetraethylene glycol dimethyl ether (tetraglyme) is prone to side reaction that form Li_2CO_3 and requires voltage up to 4 ~ 4.2V to oxidize [14-17]. Oxidization of Li_2CO_3 by the application of high voltage also causes electrolyte decomposition within the cell. High voltage application essentially created a cycle of Li_2CO_3 oxidation in the carbon electrode and Li_2CO_3 formation at the electrolyte - electrode interface [Bruce 2013]. The problem with the proposed theory was the ability to distinguish carbon species between carbon electrode and the electrolytes. The solution was composing carbon electrode with carbon isotope ^{13}C to create contrast against carbon based species found in DMSO and tetraglyme [18]. An initial fourier transform infrared spectroscopy (FTIR) was performed on the discharged state and charged state of the carbon electrode with DMSO, and the carbon electrode with tetraglyme.

The absorption peaks for both electrodes on discharge are similar and confirms the formation of products such as Li_2O_2, Li_2CO_3, HCO_2Li, and CH_3CO_2Li [17]. The absorption peak for both electrode on charge, however, only detect the oxidation of Li_2CO_3 and CH3CO2Li. Muhammed et al. also noted the possibility of HCO_2Li existence during charge due to the overlaps of absorption peaks between HCO_2Li and CH_3CO_2Li [14]. In order to quantify the amount of Li_2CO_3 formed, acid treatments on both electrodes at different stages of charge and discharge were conducted. During the treatment, mass spectroscopy detects whether the CO_2 oxidized correspond to $^{12}CO_2$ (electrolyte) or $^{13}CO_2$ (carbon electrode). Aside from quantifying the amount of Li_2CO_3 present within the carbon electrode, Fenton reagent was introduced after the acid treatment to quantify the amount of CH_3CO_2Li within the carbon electrode. The treated electrode, will once again

undergo mass spectroscopy to determine amount of CH_3CO_2Li within the electrode from the amount of CO_2 evolved.

It is evident that electrolyte decomposition is more prevalent than carbon electrode decomposition during the first charge. Both carbon electrode cycle with DMSO or tetraglyme shows a steady increase of $^{12}CO2$, however, moles of $^{13}CO_2$ overtakes the moles of $^{12}CO_2$ in carbon electrode cycled with DMSO after the first cycle.

An extended study was conducted with differential electrochemical mass spectroscopy (DEMS) to detect CO_2 evolution during electrochemistry. The method allows recording of CO_2 evolution during charging continuously.

At low charging voltage, a constant flux of $^{13}CO_2$ and $^{12}CO_2$ can be observed which suggest both $^{13}CO_2$ and $^{12}CO_2$ were oxidizing and forming at the same time. At high charging voltage, however, decomposition of electrolyte occur faster than oxidation the two species. The increase rate of electrolyte decomposition resulted in an increasing rate of CO_2 flux.

Aside from electrolyte decomposition, Muhammed et al. contribute hydrophobicity and hydrophilicity as another source of Li_2CO_3 formation. The group prepared one set of carbon electrode treated with 5 mole of HNO_3 to form a hydrophilic surface, one set of carbon electrode heated in an Ar: H2 mixture at 900ºC and a set of pristine carbon electrode.

Hydrophilic carbon have much high content of $^{12}CO_2$ detected from evolution of CH_3CO_2Li compared to untreated electrode and hydrophobic electrode. All three

demonstrates a decrease in detection of $^{12}CO_2$ as charge continues, which suggest decrease in the formation of CH_3CO_2Li. The content of $^{12}CO_2$ detected are relatively close, however, the rate of $^{12}CO_2$ detected were different. Untreated carbon electrode and hydrophobic electrode first exhibited oxidation of Li_2CO_3, however, decomposition of electrolyte begin to increase and causes an increased rate of CO_2 detection. The hydrophilic electrode differ from the others with a continuous decrease in CO_2 detection. The decrease represent oxidation of Li_2CO_3 occur at a rate faster than decomposition of electrolyte. The content of $^{13}CO_2$ for all sets of electrode were rising and signified carbon electrode decomposition.

Muhammed et al. work pointed out multiple problems with employing organic electrolyte in non-aqueous battery system. Increase overpotential to oxidize side reaction products causes electrolyte decomposition and formation of new side reaction products. The phenomenon eventually render the cell inoperable. Non-aqueous battery system, however, is not entirely non-functional, researcher simply need to choose the right combination of electrolyte to minimize side reaction.

1.2.2   Aqueous and hybrid electrolyte system

Aqueous electrolyte system is more complex and different comparing to non-aqueous system. These complexities and differences must be discussed within the components of the cell. It was known that aqueous solutions reacted violently with lithium metal and the

accepted remedy to the issue was introduction of polymer/ceramic film. The film primary functions are preventing contact between lithium metal and aqueous electrode, and providing Li^+ transport. The problem with polymer/ceramic film is twofold; low ionic conductivity associated with solid electrolyte material and instability with lithium metal (ie. NASICON). Manthiram et al identified groups of solid electrolyte currently employed in research; presented in table 1 [19].

Table 1. Summary of solid electrolyte currently employed for research for aqueous batteries. Adapted from Manthiram *et al*. [19].

Name	Type	Typical Composition	Ionic Conductivity (S cm^{-1}, RT)	Stability with Li Metal	Chemical Stability
NASICON	Glass ceramics	Li_2O-Al_2O_3-TiO_2-P_2O_5	1.3×10^{-3}	No	Stable in air, mild acids, and bases
NASICON	Crystalline	$Li_{1.3}Al_{0.3}Ti_{1.7}(PO_4)_3$	Bulk 3×10^{-3}	No	Stable in air
NASICON	Crystalline	$Li_{1.15}Y_{0.15}Zr_{1.85}(PO_4)_3$	Bulk 1.4×10^{-4}	Yes	Stable in air
Garnet	Crystalline	$Li_{7-x}La_3Zr_{2-x}Ta_xO_{12}$	1.0×10^{-3}	Yes	Stable in air, LiCl saturated water
Perovskite	Crystalline	$Li_{3x}La_{(2/3)-x}\square_{(1/3)-2x}TiO_3$	Bulk 1.5×10^{-3}	No	Stable in air, water
LISICON	Crystalline	$Li_{14}ZnGe_4O_{16}$	1.0×10^{-6}	No	Not stable in air
Si Wafer	Single Crystal	Si	6.0×10^{-7}	No	Stable in air

1.2.2.1 Polymer electrolyte between lithium metal and solid electrolyte

While the aqueous electrolyte system shows direct contact between solid electrolyte and lithium metal, a polymer based lithium conducting electrolyte layer should be placed between solid electrolyte and lithium metal. The polymer based lithium conducting electrolyte serves as a buffer zone that prevents instability between lithium metal and solid electrolyte. The problem is particularly alarming for solid electrolyte material such as NASICON [20]. There are multiple problems that plague polymer based lithium conducting electrolyte, but the most pressing issues are low ionic conductivity and lithium dendrite penetration.

Wang et al. proposed using $PEO_{18}LiTFSI$ - xN - methyl - N - propylpiperdinium bis (fluorosulfonyl)imide (PP13FSI), a polymer based lithium conducting electrolyte, as a buffer between NASICON and lithium metal [21]. The polymer electrolyte $PEO_{18}LITFSI$-xPP13FSI was compared with $PEO_{18}LITFSI$-xPP13TFSI in the study. The group addressed the issue of low ionic conductivity with addition of room temperature ionic liquid, N-alkyl-N-methyl-pyrrolidinuium bis (trifluoromethanesulfonyl) imide ($PYR_{1A}TFSI$). Two samples of polymer electrolyte were prepared, $PEO_{18}LiTFSI$ and $PEO_{18}LiTFSI$ – 1.44PP13FSI. Under optical photography the addition of PP13FSI into $PEO_{18}LiTFSI$ allow ionic liquid to fill in isolated regions.

The group suggested ionic liquid act as a bridge for ion transport in $PEO_{18}LiTFSI$ domain [21]. Immersion of ionic liquid decreases the length of travel for the ionic species

in polymer electrolyte structure. The reduction in tortuosity increases the overall diffusivity of the ionic liquid within the polymer electrolyte. An impedance test was also conducted to quantify the effect of adding 1.44PP13FSI in $PEO_{18}LiTFSI$. The polymer electrolyte was sandwiched between 2 gold foil electrodes and the cell's impedances were measure at a frequency range from 0.1 Hz to 1 MHz.

The addition of 1.44PP13FSI effectively reduced the grain boundary resistance of $PEO_{18}LiTFSI$ from 3086 Ω cm^2 to 354 Ω cm^2. The decrease in grain boundary resistance supports the phenomenon observed in optical photography. The reported ionic conductivity for $PEO_{18}LiTFSI$ at 25 ℃ is 1.3 x 10^{-6} S cm^{-1}, for $PEO_{18}LiTFSI$ – 1.44PP13FSI at 25 ℃ is 7.7 x 10^{-6} S cm^{-1}, and $PEO_{18}LiTFSI$ – 1.44PP13TFSI at 25 ℃ is 5.3 x 10^{-6} S cm^{-1} [22]. While the addition of 1.44PP13TFSI to $PEO_{18}LiTFSI$ increases the value of ionic conductivity, the ionic conductivity of the polymer electrolytes remain three orders lower than the ionic conductivity of the NASICON film. Until ionic conductivity can be significantly increase, transport resistance will continue to plague aqueous electrolyte battery system. On the issue of lithium dendrite growth, the group also reported the addition of 1.44PP13TFSI to $PEO_{18}LiTFSI$ significantly reduce initiation time of dendrite growth within the cell [21]. The polymer electrolytes were sandwiched between two lithium plates at current density of 0.1 mA cm^{-2} and temperature of 60 ℃.

A significant lithium penetration can be observed when the cell was exposed to aforementioned condition for 210 hours. The addition of 1.44PP13FSI in $PEO_{18}LiTFSI$, however, significantly delayed lithium dendrite formation. Minimal dendrite growth when the cell was exposed to the same current density and temperature at 256 hours. Observable

lithium dendrite growth was observed at 334 hours for $PEO_{18}LiTFSI – 1.44PP13FSI$ cell. Wang et al did attempt to quantify lithium growth time, however, the calculated time differ significantly from experimental time. The group contributed the discrepancy to lithium metal surface defects and impurities [23, 24]. The group also suggest mechanism behind dendrite growth will require further investigation.

1.2.3   Solid electrolyte

Solid electrolyte faces the same issues as polymer electrolyte. The lack of selection for solid electrolyte, however, narrows the choices to resolve the issues. Table 1 suggest that few option of solid electrolyte could be employed in an aqueous electrolyte battery system. $Li_2O-Al_2O_3-TiO_2-P_2O_5$, a glass ceramic NASICON, was discussed at the previous section. Glass ceramic solid electrolyte is known to be unstable when it is placed in contact with lithium metal, however, ease of manufacturing allows glass ceramic solid electrolyte to stay viable. Once sintered, the glass ceramic solid electrolyte reduce to $Li_{1+x}Al_xTi_{2-x}$ $(PO_4)_3$ [25]. NASICON is able to conduct lithium due to cavities created between TiO_6 octahedra and PO_4 tetrahedra when assemble in a three dimensional structure [26]. The resulting glass ceramic NASICON is able to attain an ionic conductivity of 1.3×10^{-3} S cm^{-1}.

The second NASICON solid electrolyte introduced was $Li_{1.3}Al_{0.3}Ti_{1.7}(PO_4)_3$. This particular solid electrolyte was first studied by Aono et al [27]. The study was based on

$Li_{1+x}M_xTi_{2-x}$ $(PO_4)_3$ single phase system. The M within the single phase system is substituted with Al, Cr, Ga, Fe, and Sc as a dopant for the system. These elements are selected for their ionic radius most closely associated with Ti^{4+} [28]. The first comparison was conducted on correlating the different element's effect on stoichiometry, porosity and ionic radius of Ti^{4+}.

One can observed Cr with stoichiometry of 0.3 has a similar ionic radius with Ti and correlate to a high porosity for the solid electrolyte. While Cr could be a perfect candidate to single phase system, the high porosity is concerning. High porosity may lead to reduction of conductivity and the possibility of aqueous electrolyte crossover. The two factors fundamentally challenge the existence of a solid electrolyte. Aono et al. then compared stoichiometry of each material to the logarithmic scale of the electro-conductivity.

It can be observed that while Cr fits well for a single phase system, its high porosity significantly reduces electro-conductivity at 0.3 for stoichiometry. Amongst the materials, Sc and Al displays the highest electro-conductivity.

Sc and Al both fall within functional trend between ionic radius and porosity of $Li_{1+x}M_xTi_{2-x}$ $(PO_4)_3$ single phase system. Both elements exhibit a significantly lower porosity, which explains the increase of their electro-conductivity. The combination of high electro-conductivity and abundancy of aluminum are mostly likely why the final composition ended with $Li_{1.3}Al_{0.3}Ti_{1.7}(PO_4)_3$.

The third NASICON solid electrolyte introduced was $Li_{1.15}Y_{0.15}Zr_{1.85}(PO_4)_3$. This particular solid electrolyte differs from the previous two as it is stable when place in contact with Li metal. $LiZr_2(PO_4)_3$ is a stable NASICON compound when put in contact with lithium. The material was reported to undergo phase transition at 310K and transitioned from triclinic phase to rhombohedral phase [29]. The transition drastically increases Li^+ conductivity from 5×10^{-8} S cm^{-1} to 1×10^{-5} S cm^{-1} [30, 31].The group proposed Y^{3+}, a dopant that forces rhombohedral phase change to increases conductivity of the solid electrolyte. Two techniques on preparing $Li_{1+x}Y_xZr_{2-x}(PO_4)_3$ were studied, spark plasma sintering (SPS) and pressureless sintering. It can be observed in that impedance of SPS reduced significantly comparing to pressureless sintering.

The diffusivity value of SPS is also significantly greater compared to pressureless sintering. The behavior between temperature and ionic conductivity through Arrhenius equation:

$$\sigma T = A \exp(-E_a / kT) \tag{5}$$

The ionic conductivity is represented by σ and activation energy is represented by E_a. The activation energy values for SPS and pressureless sintering are 0.39 eV and 0.40 eV respectively [32, 33]. At 25°C, the total conductivity for $Li_{1.15}Y_{0.15}Zr_{1.85}(PO_4)_3$ treated with pressureless sintering was 0.31×10^{-4} S cm^{-1} and the total conductivity for $Li_{1.15}Y_{0.15}Zr_{1.85}(PO_4)_3$ treated with SPS was 0.71×10^{-4} S cm^{-1}. At 25°C, the bulk conductivity for $Li_{1.15}Y_{0.15}Zr_{1.85}(PO_4)_3$ treated with pressureless sintering was 1.4×10^{-4} S cm^{-1}.

1.2.4 Aqueous electrolyte

Chemical reactions for aqueous electrolyte system are [19]:

$$4Li + O_2 + 4H^+ \rightarrow 4Li^+ + 2H_2O \qquad\qquad E_0 = 4.27 \text{ V} \qquad\qquad (5)$$

$$4Li + O_2 + 2H_2O \rightarrow 4LiOH \qquad\qquad E_0 = 3.44 \text{ V} \qquad\qquad (6)$$

The problems associated with aqueous electrode differ from non-aqueous battery system. Discharge products of aqueous electrolyte system are soluble in cathode electrolyte and usually mix with supporting salt and cathode electrolyte. The choice of cathode electrolyte can be separated into acidic and alkaline.

1.2.4.1 Acidic and alkaline cathode electrolyte

Acidic cathode electrolyte is a combination of water, acid, and supporting salt that facilitate reaction. The problem with utilizing acidic cathode electrolyte is the need to increase acid concentration in order to increase energy density of the electrolyte. Increase acid concentration significantly corrodes solid electrolyte such as NASICON ($Li_{1+x+y}Al_xTi_{2-x}Si_yP_{3-y}O_{12}$ or LTAP). Hasegawa et al first conducted a study of immersing LTAP in aqueous solution of distilled water, $LiNO_3$, LiOH, and HCl [34]. The group created an initial benchmark by immersing LTAP to distilled water. One sample was immersed for 1 month, another was immersed for 8 months. The two samples were

examined through XRD. The results of the XRD suggested water had minimal effect to the corrosion of LTAP.

It can be observed that no changes occurred in the XRD patterns with LTAP submerged for 8 months comparing to pristine LTAP. This is an important result because decomposition effect from water is decoupled. LTAP is then submerged in $LiNO_3$, LiOH, and HCl. The XRD pattern for LTAP submerged in HCl displayed an extra peak at 22 ° of 2θ.

The extra peak was identified as Li_3PO_4. The decomposition of LTAP suggests that even at low concentration of acid, solid electrolyte is prone to decomposition [35, 36]. The decomposition created a situation which the system's energy density is severely limited.

The group also submerged sample of LTAP into 1 M of LiOH for one week [34]. The test was conducted to observe the behavior of LTAP when placed with alkaline electrolyte. An extra diffraction peak was detected at 23 ° of 2θ. The decrease in decomposition time raises the question, if LTAP is fundamentally flaw and will not perform under the system specification.

The traditional technique to decrease the pH level of the catholyte is the addition of supporting salts or discharge product to the strong acids [37]. The high concentration of support salt, however, reduces cathode's ability to accept discharge products through cell reaction. The technique severely undermines cell's energy density. Low dissociation constant of strong acids maintain low pH value of the catholyte regardless of supporting

salt concentration. Li et al introduced the method of neutralizing strong acids with the addition of imidazole [38]. Imidazole and HCl combination was shown to maintain a value of 7.0 for dissociation constant [39]. The high dissociation value suggest ease of acid-dissociation for HCl and imidazole. The group plotted the pH value of catholyte as a function of imidazole concentration with the suggested dissociation value.

At a ratio 1 mole of HCl to 1.01 mole of imidazole, catholyte achieves pH level of 5. An asymptotic relation can be observed for the system at 1:1.01 ratio. In order to gauge the viability of the technique, SEM images of different samples were examined. Both structure show no signs of degradation or decomposition when compared to pristine LTAP. The cell was able to achieve discharge capacity of 136 mAh $g_{catholyte}^{-1}$ with 0.2 ml of catholyte under 0.5 mA cm^{-2} current density. This may prove high concentration acidic catholyte is still worthy for exploration.

1.2.5   Solid state system

As discussed in the previous section, solid electrolyte conductivity is significantly lower compared to electrolyte maintained in liquid phase. While solid ceramic electrolyte such as NASICON was able to facilitate charge transfer within aqueous electrolyte system, its application in solid state system is questionable. The ability of solid state system to avoid electrochemical reaction between active materials and electrolyte becomes an issue.

Hassoun et al proposed the use of poly(ethylene oxide) – lithium triflate (PEO - LiCF$_3$SO$_3$) polymer electrolyte in solid state system as a substitute for ceramic solid electrolyte [40]. LiCF$_3$SO$_3$ stability against nucleophiles such as O$_2^-$, O$_2^{2-}$, and O^{2-} and PEO polymer structure's inclination to accommodate ion are amongst several advantages proposed. These advantages suggest a cell capable of avoiding electrochemical reaction between active material and electrolyte. The solid electrolyte cell was discharged and charged with potentiodynamic cycling with galvanostatic acceleration (PCGA). The group employed PCGA due to its quasi-equilibrium property for describing electrochemical processes [41]. PCGA controls cycling of cell through a stepwise potentiodynamic state. The cell increases and decreases its voltage in a step pattern according to a prescribed current condition.

One can observed step like pattern within the voltage and current patterns. A 400 mV voltage gap between charge and discharge can be observed. The 400 mV overpotential was the lowest value reported at 2011 for cathode structure without catalyst [40]. The low overpotential was accredited to the stability of LiCF$_3$SO$_3$ toward nucleophiles under low current densities.

Hassoun's group also conducted a cyclic voltammetry to confirm electrochemical behavior. The CV was conducted at a scan rate of 100 µV s^{-1}. It can be observed CV's introduction of kinetic limitation through 100 µV s^{-1} drastically alter the curve compared with PCGA measurements. Reduction potential decreased while oxidation potential increased. The group attributed the shift in potential value to interphase resistance. The resistance most likely induced an ohmic overpotential during the forward and backward

scan. Kinetic limitation also changed the slope of the CV as opposed to quasi-equilibrium slope of the PCGA. The 400 mV peak separation was the only phenomenon remain unchanged. The group suggested altering binding matrix for better compatibility with PEO, or increasing electrode porosity could possibly solves the issue.

Since the introduction of polymer solid electrolyte, multiple groups began to explore methods to improve its electrochemical performance. Kim et al introduced a new gel-polymer electrolyte (GPE) that utilizes poly-vinylidene-flouride (PVDF) as host material [42]. PVDF's electrical stability in the presence of an electron withdrawing group and high dielectric constant (large dissolution of salt) were major reasons for its selection as host material [43, 44]. Aside from the selection of PVDF, the group also suggested the use of p-benzoquinone (pBQ) as a redox mediator to reduce overpotential during charge.

An increase in current was observed when the group conducted CV test on the cell with pBQ added. The primary reason to the increase in current for reduction and oxidation lies in the electrochemical reaction between lithium, pBQ, and oxygen [45].

$$pBQ_{sem} + e^- \leftrightarrow pBQ_{red} \qquad (7)$$

$$pBQ_{red} + O_2 \leftrightarrow pBQ_{red\,+}\,O_2^- \qquad (8)$$

$$O_2^- + Li \leftrightarrow LiO_2 \qquad (9)$$

$$pBQ_{sem} + LiO_2 + Li^+ \leftrightarrow pBQ_{ox} + Li_2O_2 \qquad (10)$$

$$pBQ_{ox} + e^- \leftrightarrow pBQ_{sem} \qquad (11)$$
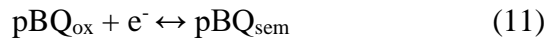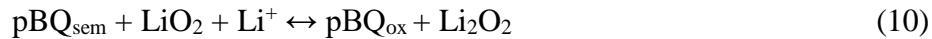
The extra electron in equation 7 and 11 reflects the increase of current seen in the CV for reduction and oxidation. In order to quantify the effect of pBQ on performance of Li-air cell, cycling test were conducted.

Three distinct behaviors can be observed from the cycling profile between PVDF GPE and PVDF/pBQ GPE: 1. increased discharge capacity, 2. decreased voltage of initial charge plateau, and 3. constant discharge capacity retention with increasing cycles. Discharge capacity increase could be accredited to increase kinetics from increase of reduction current seen in the CV. The decreased in voltage of initial charge plateau was particularly important as plateau suggested electrochemical changes. The reduction in voltage signified an early oxidation of discharge product and reflected pBQ's role as a redox mediator. The consistent discharge retention until cycle 34 reflected on pBQ's ability to breakdown insulating discharge product. Consistent decomposition ensure minimal surface passivation, thus capacity retention. The group's work reflected on previous suggestion for better polymer material selection and the need for electrocatalyst.

1.2.6 Room temperature ionic liquid

Room temperature ionic liquids (RTIL) are becoming more popular in recent years as substitutes for organic electrolytes after Muhammed et al's report on decomposition of organic electrolyte in Li-air battery [14]. The reasons for the switch are largely due to the intrinsic property that RTILs can offer. RTILs are usually quaternary ammonium salts that

maintain a low melting temperature and vapor pressure [46]. Its low vapor pressure render the electrolyte inflammable, and its low melting temperature ensure transport property remain high (fluid state). Cation such as imidazolium or pyridinium ring with alkyl group attached to carbon or nitrogen are also employing in the field [47]. Electrochemical stability of RTIL is the focal point for such drastic transition. RTILs are able to maintain stability above 4V, which is required for high energy applications. Prior to use in secondary battery system, lithium salt with same anion to ionic liquid, $[Li^+]$ $[C^-]$, should be added to ionic liquid, $[A^+]$ $[C^-]$. The addition of the two salts, under careful design, should form a new ionic liquid with composition of $[Li^+]_m$ $[A^+]_n$ $[C^-]_{m+n}$ [46]. The ionic liquid's weak lithium bond allow diffusion to occur as lithium ion travel from salt to salt until it reaches carbon cathode.

Kuboki et al tested the feasibility of utilizing ionic liquid as an electrolyte with an experiment which compared yjr discharge of ethylene carbonate (EC) and propylene carbonate (PC) with discharge of EMITFSI, EMIBETI, and MOITFSI [48]. The cell with EC/PC composition, was discharged at 0.01 mA cm^{-2}.

The resulting discharge capacity of the cell in air was about 940 mAh g^{-1} when normalized with the mass of carbon in the electrode. Ionic liquids EMITFSI, EMIBETI, and MOITFSI were only three found to be stable for several months. The stability was accredited to the formation of SEI by LiF [48]. When the group altered the electrolyte employed with EMITFSI, EMIBETI, and MOITFSI, discharge capacities dramatically increased.

It could be observed that EMITFSI and EMIBETI were able to achieve discharge capacities of 1790 mAh g^{-1} and 5360 mAh g^{-1} respectively. The exception to the case was MOITFSI, which achieved a discharge capacity of 640 mAh g^{-1}. It was observed that foamy ionic liquid leaked through opening of the cell, thus prevented oxygen diffusion into the cell. The leakage was accredited to the high viscosity of MOITFSI.

Lithium air cells provided exceptional discharge capacity in pure oxygen environment, but suffers significant discharge capacity reduction once introduced to ambient air. The reduction of discharge capacity was widely accredited to side reaction created by moisture and gases. Sankarasubramanian et al first proposed to study the electrochemical effect of water addition to ionic liquid to uncouple these effects [49]. The ionic liquid studied was N,N-diethyl-N-methyl-N-(2-methoxyethyl) ammonium bis(trifluoromethanesulfonyl)imide (DEME-TFSI) combined with deionized water. CV was conducted between DEMETFSI and water saturated DEMETFSI on glassy carbon.

For the anhydrous DEMETFSI, ORR onset occurred at 2.45V and OER onset occurred at 2.41V. For the water saturated DEMETFSI, ORR onset occurred at 2.49V and OER onset occurred at 3.65V. The difference of peak separation of anhydrous DEMETFSI was measured at 0.3V and water saturated DEMETFSI was measured at 1.35V. The increased difference was accredited to irreversibility [49]. While irreversibility maintained a primary problem, side reaction, a factor linked to irreversibility, proved to be minor. At an increasing scan rate, anodic and cathode peak remained constant. The result suggest side reaction did not significantly impacted electrochemistry of the cell. Rotating disk voltammograms measurement were also recorded at a scanning rate at 10 mV s^{-1}. The

23

reaction was primarily kinetically limited at low rpm. As rpm continues to increase, reaction essentially became mass-transport limited due to rotational dependency. These data were particularly important as they were needed to calculate rate constant of the reaction through Koutecky-Levich equation.

$$\frac{1}{i} = \frac{1}{i_k} + \frac{1}{i_L} = \frac{1}{i_k} + \frac{1}{B\sqrt{\omega}} \tag{12}$$

$$i_k = (i_L \cdot i)/(i_L - i) \tag{13}$$

$$B = 0.62nFAD^{\frac{2}{3}}v^{-\frac{1}{6}}C_b \tag{14}$$

$$i = nFAkC_b \tag{15}$$

From equation 14, F is the faraday's constant, n is the number of electron in the overall reaction, A is the disk area, D is the diffusion coefficient of O_2, v is the kinematic viscosity, and C_b is the bulk concentration of O_2. From equation 13, i_k is the kinetic current, i_L is the mass-transport current, and i is the measured current. From equation 12, ω is rotational speed. The constant B could be calculated when i^{-1} is plotted against $\omega^{-1/2}$. The rate constant of the reaction can finally be calculated by equation 15.

Water saturated DEMETFSI was able to increase rate constant of the ORR, and maintained stability within the cell. Further exploration would allow control of Li-air cell kinetics through the monitoring of moisture content within the cell. Adjustments could be implemented to increase the cell's discharge capacity and cyclability.

2 LITERATURE REVIEW OF CATHODE MICROSTRUCTURE

Multiple configurations of lithium-air cells were tested to improve discharge capacity. These configurations included alteration of electrolytes, electro-catalysts, and materials employed in lithium-air cells. The common factor that link different lithium-air cell designs together is a mesoporous positive electrode. The fundamental principle for a mesoporous positive electrode is maximizing surface area in a finite volume to reduce overall weight. The two prevalent methods for obtaining mesoporous structures are dried carbon slurry and commercially available carbon fiber paper [50, 51].

2.1 Ketjen black

Ketjen Black (KB) is a conductive carbon material which has been constantly used as foundation for many cathode structures. Researchers favor the use of KB due to its' high Brunauer-Emmett-Teller (BET) surface area: 800 - 1400 m^2/g [52]. There are skeptic, however, toward further use of KB as cathode material. Perfectly optimized materials were seldom solutions to increase discharge capacity [50]. Zhang et al proposed a study to optimize lithium-air performance based on current density employed and oxygen flux (ambient air) needed to enhance discharge capacity. The group first tabulated parameters, table 2, required to support reaction at specific current densities.

Table 2. Comparison of polymer membranes' minimal physical parameters required to support function at specific current densities. Adapted from Zhang *et al*. [50].

Membrane	Current Density (mA cm^{-2})	Film Thickness (μm)	Oxygen Partial Pressure (atm)	Required Minimum O$_2$ flow (mol m^{-2} s^{-1})	Membrane O$_2$ flow at 25°C / 0.21 atm (mol m^{-2} s^{-1})	Measured O$_2$ permeability of membrane (cm^3 m^{-2} day^{-1} atm^{-1})
ML[a]	0.1	20	0.21	2.16 x 10^{-7}	7.79 x 10^{-7}	71.8
ML[a]	0.05	20	0.21	1.08 x 10^{-7}	7.79 x 10^{-7}	71.8
ML[a]	0.05	30	0.21	1.08 x 10^{-7}	5.25 x 10^{-7}	48.4
MSE-HDPE[b]	0.1	25	0.21	2.16 x 10^{-7}	5.67 x 10^{-7}	5224
Blue-HDPE[c]	0.1	50	0.21	2.16 x 10^{-7}	6.36 x 10^{-7}	5857
MSE-HDPE[b]	0.05	50	0.21	1.08 x 10^{-7}	2.80 x 10^{-7}	2577
Blue-HDPE[c]	0.05	46	0.21	1.08 x 10^{-7}	5.49 x 10^{-7}	5055

[a] Melinex 301 H, DuPoint Teijin Films
[b] Mid South Extrusion, Inc.
[c] Blueridge Films, Inc.

At current density of 0.05 to 0.1 mA cm^{-2}, minimum O$_2$ flow of 1.08 to 2.16 x 10^{-7} mol m^{-2} s^{-1} were needed to support maximum discharge capacity. Once kinetic limitation was eliminated, the group proposed substituting DARCO® G-60 carbon with KB. The substitution with KB increases mesoporous volume which increases discharge capacity [50]. The discharge capacity, of the new cell with KB substituted, was discharged and compared against the traditional G-60 carbon.

As expected, KB based air electrode achieved a discharge capacity significantly higher than that of G-60. Zhang's group, however, realized the increased discharge capacity was at a cost of reduced specific energy.

Since specific energy is largely dependent on active material such as carbon and lithium, the disproportion weight percentage of electrolyte would reduce specific energy. The disproportion of weight distribution within the cell was attributed to the overly high mesoporous volume property of KB which generated a dry electrode structure with a bulk porosity of 88.7%. Lithium-air precipitate generally react in the oxygen - electrolyte - carbon particle interface, thus an ultrahigh bulk porosity will generate inactive void within the porous structure. The retention of electrolyte in these inactive void are the primary reason for the drop in specific energy. Ketjen Black is still an excellent material to use as cathode material, however, proper control of its bulk porosity during the casting of the electrode will be paramount to the retention of lithium-air specific energy.

2.2 Super p carbon

Another popular material employed as foundation for cathode structure is the Super P carbon. The use of Super P carbon is limited in recent years as it cannot compete against property of new cathode materials. For example, Super P carbon has a BET surface area of 69.3 m^2 g^{-1} when Ketjen Black has a BET surface area of 800-1400 m^2 g^{-1}; a difference in two order of magnitude. The differences between Super P carbon and K carbon, table 3, are as follow [53].

Table 3. Comparison of electrodes casted with SP carbon, K-carbon, and CuFe catalyzed K-carbon. Adapted from Ren *et al.* [53].

	SP-carbon	K-carbon	CuFe catalyzed K-carbon
Graphitic basal plane d-spacing / Å	3.573	3.722	3.620
Crystallite size parallel to basal plane / Å	39.6	20.8	30.2
BET surface / $m^2\,g^{-1}$	69.3	1413	751
Total pore vol @ > 20 Å dia. / $cm^3\,g^{-1}$	0.14	2.06	1.23
Electrode porosity by solvent method [a]	$77.3 \pm 1.8\%$	$90.8 \pm 0.5\%$	$86.8 \pm 0.7\%$
Electrode pore vol., [b] / $cm^3\,g^{-1}_{carbon}$	1.89	5.46	3.64
Electrode porosity by thickness method [a]	$75.3 \pm 2.2\%$	$90.9 \pm 1.1\%$	$87.9 \pm 1.5\%$
Li/air cell discharge capacity, mAh g^{-1}_{carbon}			
@0.05 / $mA\,cm^{-2}$	531	1286	1339
@0.20 / $mA\,cm^{-2}$	356	761	817
@0.50 / $mA\,cm^{-2}$	205	430	597
@1.00 / $mA\,cm^{-2}$	-	165	390

[a]   Average and standard deviation from measurement of 6 samples.
[b]   Calculated from electrode porosity by solvent method.

Super P carbon has an electrode pore volume three times lower than K-carbon. The reduced electrode pore volume is important since the material could prevent potential inactive void during casting. The reduced inactive void decreases non-reactive electrolyte retention and increases specific energy of lithium-air cell. The electrode pore volume could be observed with a proportional reduction in bulk electrode porosity by solvent method (77.3%), and by thickness method (75.3%). Although the reduction of electrode pore volume and bulk porosity are integral to improve discharge capacity, BET surface area/active surface area is the primary factor to improve discharge capacity.

At a discharge current of 0.2 mA cm^{-2}, lithium air battery with air electrode of Super P carbon achieved a discharge capacity of 356 mAh g^{-1}, and Ketjen Black carbon achieved a discharge capacity of 761 mAh g^{-1}. At a discharge current of 0.05 mA cm^{-2}, lithium air battery with air electrode of Super P carbon achieved a discharge capacity of 531 mAh g^{-1}, and Ketjen Black carbon achieved a discharge capacity of 1286 mAh g^{-1}. The discharge capacity of Ketjen Black at 0.05 mA cm^{-2} reported by Ren's group is almost the same as Zhang's group reported value [50]. From these data, it could be said that active surface area should be optimized prior to porosity volume or bulk porosity. Super P carbon, in general, would be a great material to utilize to reduce bulk porosity.

2.3 Carbon fiber

Carbon fiber is an interesting structure for investigation compared to fine carbon powder such as Ketjen Black and Super P carbon. While fine carbon powder form mesoporous structure, carbon fiber, as the name suggests, form wire like structure within a confine space. Fiber structure is convenient since thread structure is unable to induce inactive void through material enclosure or increase bulk porosity. Bulk porosity could be controlled through the increase of threads within a finite volume. Active surface area would largely depend on surface area of each thread. Aside from physical property, reproducibility is another important parameter. Majority of these carbon fiber structure are produce in a uniform scale from a fixed procedure thus variation of carbon electrode

compared to those created with different laboratories, equipment, procedure and human error may be lower. McCloskey et al's investigation of a solvent's role in nonaqueous lithium air battery, figure 1, allows a comparison of performance between carbon fiber electrode and mesoporous carbon electrode [51].
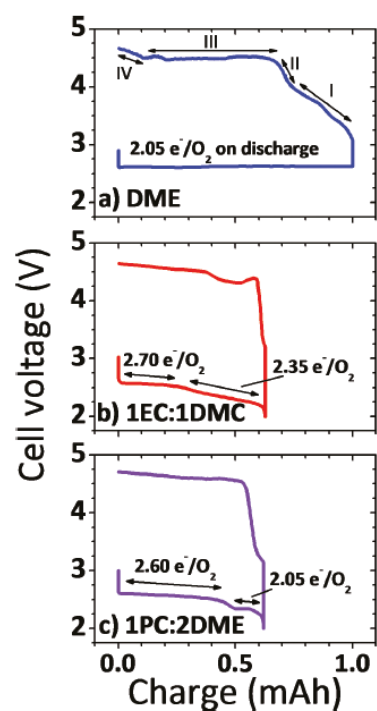
Figure 1. McCloskey et al's discharge-charge curve at 0.09 mA cm^{-2} for lithium-air cell with DME (top), 1EC:1DMC volume ratio (middle), and 1PC:2DME volume ratio (bottom). Adapted from McCloskey *et al*. [51].

McCloskey's group study of 90% porous Avcarb P50 carbon electrodes with various electrolyte which subjected to a current density of 0.09 mA cm^{-2} yielded a discharge capacity between 0.6 mAh and 1.0 mAh. The discharge capacity after calculation correspond to specific discharge capacity between 742.77 mAh g$_{carbon}^{-1}$ and 1237.95 mAh g$_{carbon}^{-1}$ with the prescribed dimension of the electrode that a mass of 8.077*10^{-4} gram of carbon was employed. A comparison could be made against the result proposed by Ren et al's Ketjen Black air electrode due to the similarity in bulk porosity of the air electrode. Even at a higher current density, McCloskey's group achieved a specific discharge capacity equivalent to Ketjen Black carbon electrode. It is recognized that Ren's lithium air battery employed PC – Tris(2,2,2-trifluoroethyl) phosphate (TFP), and McCloskey's lithium air battery employed DME, 1EC:1DMC, and 1PC:2DME, which may impact the kinetics of the cell. Their testing environment, pure oxygen, eliminated the factor of oxygen starvation. This signify the cell will most likely achieve its maximum discharge through the influence of microstructure effect. The result implicitly implied the inherent strength of carbon fiber structure.

2.4 Mesoporous structure (experiment)

It was suggested the capacity of Lithium-air battery is proportional to the electrode's pore volume because pore volume allow precipitate growth [54]. The result from Ren et al, however, suggested a balance between electrode surface area and pore

volume is needed. Increase of carbon loading to compensate or increase surface area is a solution, however, could also drastically decreases discharge capacity of lithium-air battery [55]. Xiao et al constructed a study to quantify the balance between surface area, pore volume, and carbon loading. The group investigated few sets of commercial carbons: BP2000, Calgon, Denka, Ketjen Black EC600JD, ball-milled Ketjen Black, and a self-assembled mesoporous carbon electrode (JMC). The surface area of the materials was analyzed through BET, and the pore volume and pore size distribution were evaluated through Barrett-Joyner-Halenda (BJH) method. The materials, table 4, demonstrated a wide range in values for surface area, pore volume, and BJH pore size.

Table 4. Comparison of surface area, pore volume, and BJH pore size of various conductive carbon electrode (adapted from Xiao *et al*. [55])

	Surface Area ($m^2 g^{-1}$)	Pore Volume ($cm^3 g^{-1}$)	BJH pore size (nm)	Microstructure from XRD
KB	2672	7.6510	2.217 – 15 nm	Poor Crystalline Graphite
Ballmilled KB	342.4	0.4334	No clear peak in size distribution	Amorphous
BP2000	1567	0.8350	No clear peak in size distribution	Poor Crystalline Graphite
Calgon	1006	0.5460	No clear peak in size distribution	Crystalline Graphite
Denka Black	102.0	0.5355	2.511 and 6 nm	Poor Crystalline Graphite
JMC	548.7	0.2376	3-3.8 nm	Amorphous with ordered mesopores

The materials were assembled into uniform coin cells then discharged to 2V at 0.05 mA cm^{-2}. Discharge terminates when current density falls below 0.01 mA cm^{-2}. The specific discharge capacity for the cells, suggested combination between surface area, pore volume, and BJH pore size could severely increase or reduce specific discharge capacity.

2.4.1   Surface area effect on discharge capacity

Surface area of the materials investigated decrease in the following order: Ketjen Black, BP2000, Calgon, JMC, ball milled Ketjen Black, and Denka Black. The traditional expectation would be a decrease in specific discharge capacity with the same order. There is, however, a huge discrepancy on the theory that surface area dictated specific discharge capacity. The specific discharge capacity decreased in the following order: Ketjen Black, Calgon, Ball milled Ketjen Black, BP2000, JMC, and Denka Black. When Ball milled Ketjen Black achieved a discharge capacity similar to BP2000, the assumption which surface area dictated specific discharge capacity is fallible.

2.4.2   Pore volume effect on discharge capacity

Pore volume of the materials investigated decrease in the following order: Ketjen Black, BP2000, Calgon, Denka Black, ball milled Ketjen Black, and JMC. Previous

discussion suggested the need for balancing pore volume and surface area since the increase of pore volume also increases bulk porosity. Bulk porosity increase would significantly increase inactive surface area available for reaction, whereas drastic decrease of bulk porosity would decrease active surface area available for reaction.

2.4.3   Pore size effect on discharge capacity

Only three sets of material yield noticeable result for BJH pore diameter: KB, Denka Black, and the self-assembled JMC. JMC being the most consistent in pore size ranges when compared to either KB or Denka Black. While the three materials offer minimal similarity for comparison, a comparison could be made against ball milled Ketjen Black. Ball milled Ketjen Black similarity with Denka Black on parameters such as BET surface area and pore volume allowed a base line for comparison. Denka Black's poor performance for specific discharge capacity was attributed to the increase of bulk porosity through wide variation in BJH pore diameter. The lack of consistency most likely increased bulk porosity of the electrode [54].

2.4.4 Carbon loading effect on discharge capacity.

It can be inferred that a dependent relationships exist between active surface area, pore volume, and pore diameter. Increase carbon loading is the most direct method to improve the three parameters. As addressed before, constant increase to the input of active material will eventually lead to degradation of specific discharge capacity. One form of degradation is the loss of inactive porous void for precipitation growth. Xiao's group was able to determine the relationships of carbon loading, specific capacity, and area specific capacity.

With an initial carbon loading of 5 mg cm^{-2}, Xiao's configuration of lithium air cell achieved a specific discharge capacity of 1400 mAh g^{-1}. Subsequence increase in carbon loading causes a steady decline in specific discharge capacity, however, there are sets of carbon loading ranges with minimal decline in specific discharge capacity. Carbon loading between 11 mg cm^{-2} and 15 mg cm^{-2}, and carbon loading between 18 mg cm^{-2} and 21 mg cm^{-2} shows minimal loss to specific capacity. These gaps are essential for occasion such as bulk porosity reduction or the increase of specific surface area. The increase of carbon loading shows an increasing trend for area specific capacity from 5 mg cm^{-2} to 16 mg cm^{-2} and a drastic decrease from 16 mg cm^{-2} to 26 mg cm^{-2}. The sudden shift at 16 mg cm^{-2} suggests active material largely replaced the inactive void within the microstructure. The increase of active surface area, in turn, increases area specific discharge capacity.

Carbon loading is inherently dependent on microstructural parameters such as active surface area, pore volume, bulk porosity, and pore size. Balance between the four independent variables is essential to maximize specific discharge capacity or area specific discharge capacity.

2.5 Fiber structure (experiment)

Due to the wire like structure of carbon paper (fiber), problem such as pore volume and pore size can be avoided with ease. The main control toward bulk porosity essentially falls on carbon loading. Since carbon papers are primarily used as gas diffusion layer for application such as fuel cell or flow cell, variation in porosity and its effect on the discharge capacity were seldom studied.

2.6 Discharge product morphology

Microstructural parameters are primary factors which influence discharge capacity. The reason to optimize microstructural parameter is to maximize active surface area while maintaining specific energy density through management of carbon loading and porosity. Microstructural parameters, however, only influence the governing system of electro-chemical energy storage unit. Input to the system could also influences the

output (discharge capacity) of the system. Applied current density is the primary input to the system which increase gradients of species diffusion and charge migration. Griffith et al conducted a series of experiment to correlate discharge capacity of the battery with discharge product morphology [56].
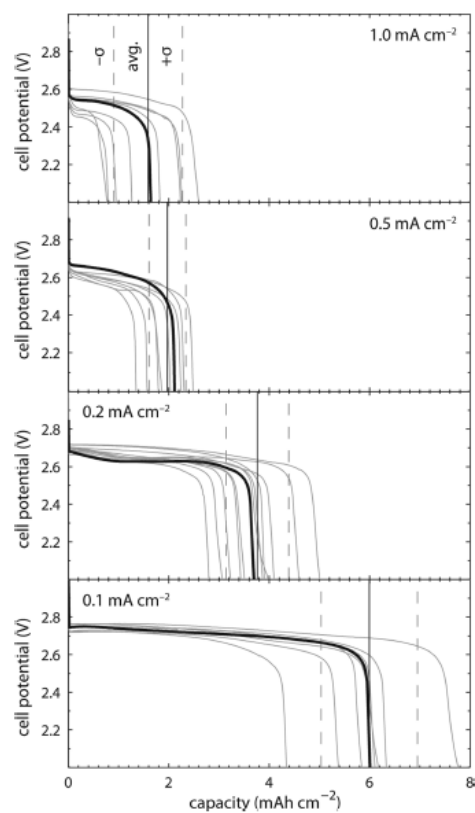
Figure 2. Performance curves of lithium air battery precipitate (Li_2O_2) at multiple discharge rates. Adapted from Griffith *et al*. [56].

The discharge capacity of Giffith's group experiment, figure 2, corresponded to the data observed in other literatures which suggested the increase of current density has an inverse effect on discharge capacity. The decrease on discharge capacity was accredited to the increase in kinetic with the electro-chemical energy storage system. The increased kinetic of species diffusion may have overwhelmed oxygen diffusion kinetics, thus created an oxygen limiting reaction [Griffith 2015]. Increasing tortuosity within the microstructure further impede oxygen's ability to diffuse through electrolyte. The inability to support current density within the battery causes termination of cell voltage. Upon the termination of cell voltage, the precipitate within the air electrode of the battery was investigated via scanning electron microscopy (SEM), figure 3.
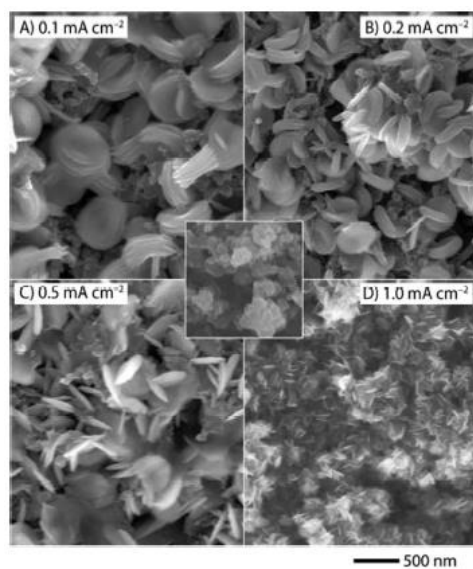
Figure 3. Griffith et al's SEM of lithium air battery precipitate (Li_2O_2) at multiple discharge rates. Adapted from Griffith *et al*. [56].

The SEM image of Li_2O_2 at 0.1 mA cm^{-2} showed a toroidal shaped morphology, whereas the SEM image at 1 mA cm^{-2} showed a needle shaped morphology. The group tabulated the variation in particle size and physical parameters in table 5.

Table 5. Variation of Li_2O_2 in particle size, physical parameter, discharge capacity and cumulative volume with respect to apply current density. Adapted from Griffith *et al.* [56].

Rate (mA cm^{-2})	Particle diameter (nm)	Particle height (nm)	Particle volume (x 10^5 nm^3)	Surface-to-volume ratio (x 10^{-2} nm^{-1})	Number of particles (x 10^{12})	Total product volume (mm^3)	Discharge capacity (mAh cm^{-2})
0.1	415 ± 47	188 ± 44	254 ± 72	2.0 ± 0.5	0.22 ± 0.07	5.7 ± 0.9	6.0 ± 1.0
0.2	346 ± 41	88 ± 24	83 ± 26	3.4 ± 1.0	0.43 ± 0.16	3.6 ± 0.6	3.8 ± 0.6
0.5	334 ± 51	65 ± 19	57 ± 21	4.3 ± 1.4	0.33 ± 0.13	1.9 ± 0.4	2.0 ± 0.4
1.0	18.6 ± 4.8	109 ± 17	0.30 ± 0.12	23.3 ± 7.0	51 ± 29	1.5 ± 0.6	1.6 ± 0.7

Number of particles and total product volume are estimated using the mean particle volume and the density of bulk crystalline Li_2O_2

At a glance, the initial hypothesis on the variation of morphology to many would be a direct correlation between morphology and discharge capacity. Griffith's group, however, reported a lack of information for such correlation. The group explained that free energy at the expense of cell potential was needed in order to generate the observed morphology, thus it is more likely morphology shares a relationship with voltage than capacity.

While the relationship between morphology and capacity requires further investigation, the growth of morphology has a direct impact on microstructure parameter. As precipitate growth increases, porosity of the air electrode decreases and causes an increase in tortuosity. The change in microstructural parameter alter the effective parameter employed within the governing equation with respect to time. Current state of

research suggests applied current density (input) influence microstructural parameter explicitly and discharge capacity implicitly.

2.7 Mesoporous structure (simulation)

Electrochemical storage in general is governed by mathematical relations such as species conservation and charge conservation. Although the governing conservation law is the same, the model applied to diffusion, products formation, and microstructural effect could be different. A general consensus could be made: the accuracy of the modeling program can be controlled through advances in the mathematical model. Models of discharge behavior also reaffirm observation seen in experiments. Andrei et al model the physical parameter lithium-air battery through Bruggeman correlations [57]. The correlation uses porosity of the structure to recalculate the effective physical parameter within a mesoporous structure. Species conservation and charge conservation in electrolyte phase would calculate electrolyte potential. Charge conservation in solid would calculate solid potential. The overpotential generated from these terms essentially terminate voltage as species continue to diffuse and electron continue to migrate. Butler-Volmer, a constitutive equation, summate the perspective overpotential and reiterate the current density driving species diffusion and electron migration. Both cathode and separator have an initial porosity of 0.75. Contrast against experimental work is nearly

impossible due to the lack of information on surface area or the structure's shape. Correlation on current density, figure 4, is at least agreeable.
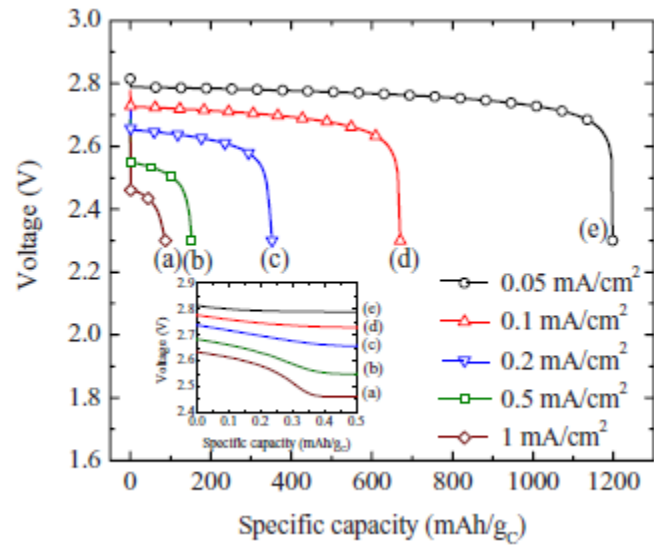
Figure 4. Comparison of current density on specific discharge capacity v. voltage. Adapted from Andrei *et al*. [57].

As current density increases, specific discharge capacity decreases. The trend is similar to previous work on characterizing current density [56].

The problem with earlier model is the lack of information regarding the description microstructure. Experimental results at least provided basic information such as BET

surface area, pore volume, and carbon loading. The strict reliance on modeling microstructure parameter with Bruggeman's relationship when porosity is changing with respect to time signified an improper application of boundary. Until microstructure parameter could be characterize with time, the governing equation employed will be flawed.

3   METHODOLOGY

The primary purpose of this thesis is exploring electrode microstructural impact on lithium-air battery. Current literatures on modeling lithium-air battery discharge behavior, as mention in previous chapter, lacks microstructure parameters for accurate description or depiction of the electrode employed in current experiment. Pore size, fiber diameter, active surface area, and carbon loading are parameters essential to depicting microstructure. Other than microstructural parameters, utilization of Bruggeman's relationship to characterize effective physical parameter within a microstructure is fundamentally flawed. For example, Andrei's group characterize effective diffusivity with function 16,

$$D_{species,effective} = \varepsilon^{\beta_{species}-1} \cdot D_{species} \tag{16}.$$

$D_{species,effective}$ is the effective diffusivity, ε is the initial porosity of the microstructure, and $\beta_{species}$ is a constant. The problem with the following approximation is the value, 0.75, used for ε. As discharge progress, precipitate would continuously deposit on active surface area of the air electrode. The increasing precipitate will continuously occupy porous void, thus the assumption that ε is a constant is flawed. The change in porosity as precipitate grow would change the value of tortuosity as well which implies tortuosity is a function with respect to porosity.

3.1 Solution

In order to generate a function that monitor the change of porosity in the air electrode, a parametric study to microstructure growth will be warranted. The problem many literature encountered was the need to simplify their microstructure model primarily due to the inability to generate microstructure [57] [58]. Commercial software program, GeoDict, was able to solve this problem. The program offered the ability to create complex electrode including mesoporous structure created with carbon powder and fiber structures. Aside from physical shape, the program also allow the control of porosity, material composition, pore size, fiber diameter, fiber length, domain size and resolution of the structure. Parametric generation of pristine electrode with be a fundamental milestone toward the study electrode microstructural impact on lithium-air battery.

Precipitation addition will be a critical milestone for to understanding electrode microstructural impact. The parametric deposition of precipitate essentially provide a time table to microstructural parameter changes. An in-house C-code was generated to add and control precipitate within the pristine structure.

Discharge air electrodes will be characterized through two in-house C-code: 1. Characterization of the effective conductivity, and 2. Characterization of tortuosity. The values generated from characterization of microstructure parameter with increasing precipitation volume fraction will help construct a non-linear function correlating multiple factors. These functions will then be used to characterize precipitate growth. These non-

linear functions will be critical to simulation of porosity change and calculation of discharge capacity.

3.2 Parameter selection

In the previous chapter, two categories of microstructure were discussed: 1. Mesoporous electrode, and 2. Fiberous electrode. Due to the uniformity and availability of carbon paper the following study will be concentrated on fiberous electrode. From literature review, porosity of most structure stay within the range of 60% - 90%. From commercial specification data, fiber diameter stay within 8-10 µm. Table 6 tabulated the parameter used for parametric generation of pristine carbon fiber electrode.

Table 6. Physical parameter used for parametric study of pristine carbon fiber electrode

Porosity	60% 70% 80% 90%
Li_2O_2 (Precipitate) volumetric addition	10% 20% 30% 40%
Mean Fiber diameter	0.01 µm, 0.1 µm, 1 µm, 10 µm
Mean Fiber length	500 µm
Voxel Size	10
Voxel Length	1 µm
Domain Size	100 µm x 100 µm x 100 µm
Precipitate Deposition Preference Coefficient	0.2 0.4 0.6 0.8
Applied Current Density	1 A m^{-2} 2 A m^{-2} 5 A m^{-2} 10 A m^{-2}

The pristine structures are presented in figure 5.

a

b

c

d
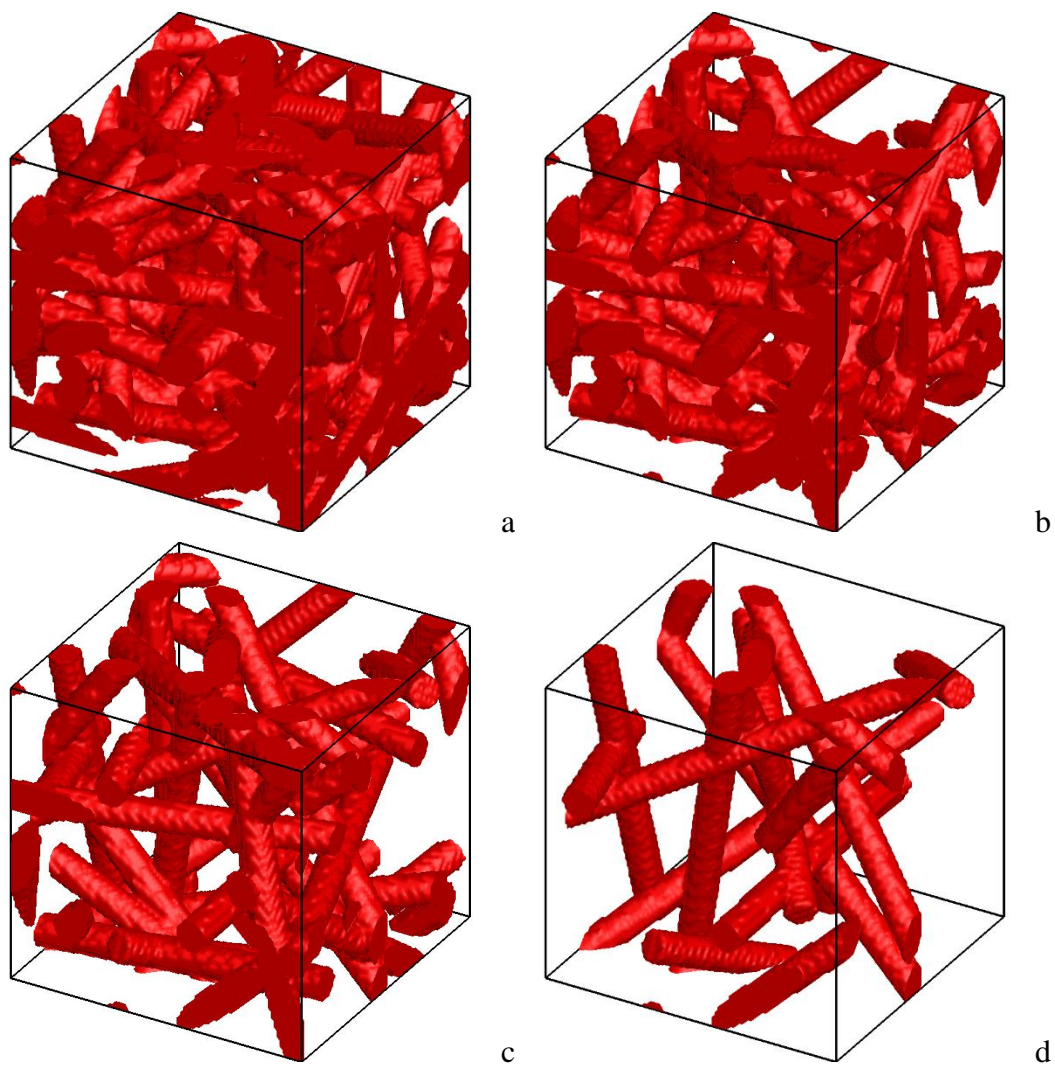
Figure 5. Pristine fiber structure with fiber diameter of 10 μm, fiber length of 500 μm, and porosity of (a) 60% (b) 70% (c) 80% and (d) 90%.

3.3 Precipitate addition

The execution of the C-code for precipitate addition requires several input parameters, which are domain lengths in x, y, z-direction, precipitation deposition preference coefficient, simultaneous precipitation deposition site, and volume percentage of secondary phase that will be generated. Precipitation deposition preference coefficient is created to address the morphology change due to current density [56]. Simultaneous precipitation deposition site is created to address the randomness of deposition within each loop.

3.3.1   Precipitation deposition preference coefficient

The precipitation deposition preference coefficient value was created to address the morphological change observed with current density change. Precipitation deposition preference coefficient is an input value normalized at $0 < \omega < 1$. The value act as a modifier to increase or decrease the likeliness that a precipitate will deposit on carbon surface or other precipitate. Low ω value signify precipitate is more willing to deposit on an active carbon surface, while high w value signify a precipitate is more willing to deposit on precipitate. Figure 6 illustrates the differences in microstructure when changing w value was applied to the precipitate addition code.

49
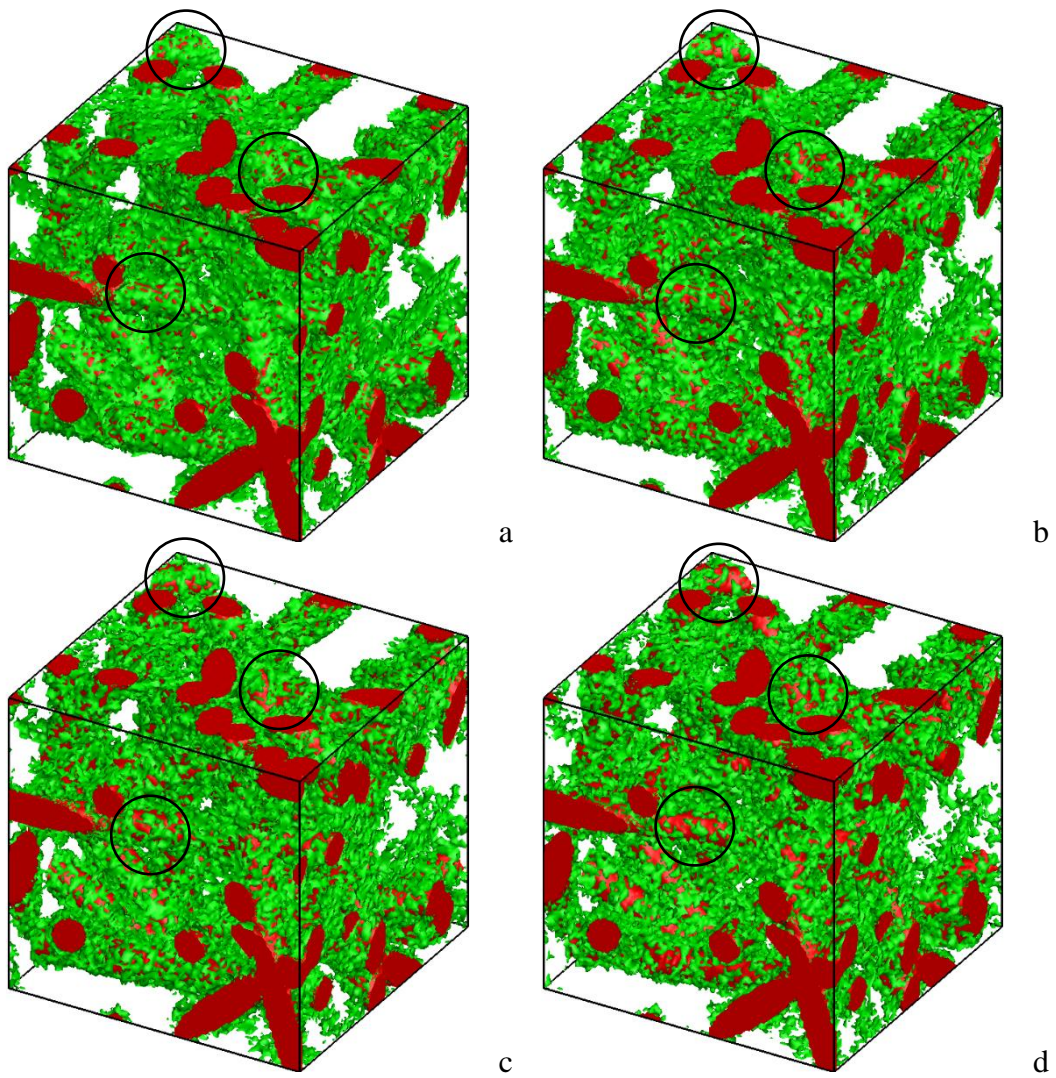
Figure 6. Microstructure representation after 10% volumetric deposition in 80% porous fiber structure with precipitation deposition preference coefficient: (a) 0.2 (b) 0.4 (c) 0.6 and (d) 0.8.

With increasing w value, surface area of the fiber (red) is more apparent. The functionality of precipitation deposition preference coefficient is bolster by the increase in non-dimensional surface area of microstructure, table 7.

Table 7. Non-dimensional interfacial area of microstructure with increasing precipitate deposition preference coefficient

Precipitate Deposition Preference Coefficient	01 area	porosity	active material	secondary
0.2	0.045014	70.3232	20.6045	9.0723
0.4	0.1000555	70.1275	20.6045	9.2680
0.6	0.1597006	70.0551	20.6045	9.3404
0.8	0.2341968	70.0560	20.6045	9.3395

The increase deposition of precipitate (green) onto itself affirms the behavior observed in literature (Griffith 2015). The limit to the model is the inability to distinguish exact shape Griffith et al observe, however, serves the intended purpose at a macroscopic level.

3.3.2 Simultaneous precipitation deposition site value

Simultaneous precipitation deposition site is an input value used to ensure only a fix number of sites within each loop have the potential to turn into precipitate. This ensure randomness within each loop is not overwhelmingly small or large. The value also act as a condition to terminate the loop. Function 17 calculates the value of simultaneous precipitation deposition site.

$$N_{\text{simultaneous}} = M_x \cdot M_y \cdot M_z / F \tag{17}$$

$N_{\text{simultaneous}}$ is the value of simultaneous precipitation deposition site, M_x is the domain size in the x-direction, M_y is the domain size in the y-direction, M_z is the domain size in the z-direction, and F is the simultaneous precipitation deposition factor. It is not necessary that the amount of site turn into precipitation is equal to the value of simultaneous precipitation deposition site. The random number generator may generate value that matches none of the values in cumulative energy function. An alternative scenario would be the random number generator generate a value that was generated previously. Both conditions reduce the amount of deposition site reaching the amount of simultaneous precipitation deposition site.

3.3.3 Precipitation C-code function

The in-house precipitate addition C-code first initialize a loop which transform the three-dimensional coordinate of each cell into one-dimensional coordinate. The C-code then read the data file created from GeoDict which interpret void space with value of 0 and active material (carbon) with value of 1.

Loop for deposition of precipitate begins with the initial coordinate of the box. The code then searches the value of the coordinate near its current coordinate. Two boundary conditions were implemented to prevent potential consideration of site: 1. site that is surround by inactive void on all six direction, 2. Site that is surrounded by active material on all six direction. The only method which precipitation, value 2, would replace a void, value 0, is the coordinate has a maximum of five directions or minimum of one direction with a value of 1 or 2. Each void coordinate is then assigned with a value that represent an energy threshold. Function calculating the energy threshold of a void coordinate that is next to either carbon or precipitate is different. The function which calculate energy of the coordinate adjacent to active area is designated as:

$$Energy = Energy^o + \frac{1-w}{6} \tag{18},$$

and the function which calculate energy of coordinate adjacent to precipitate is designated as:

$$Energy = Energy^o + \frac{w}{6} \tag{19}.$$

The loop will continue until the entire domain is scanned.

Initial rationale for the selection of deposition site was normalizing the energy value of all coordinate with the highest energy value found within the loop. The problem with this approach was the irregularity of the function with consecutive loops. To establish a one to one function, cumulative energy relation was implemented. Energy of subsequent coordinates are summated, which generates a linear profile with a one to one relationship.

The decision to whether a porous void site turns into a precipitate was determine by a random number generator. The random number generator creates a cumulative energy value and searches for a site with the same cumulative energy value. An extra step was implemented to ensure the cumulative energy of the site before is less than or equal to the cumulative energy value generated. When the boundary conditions are satisfied, the porous void value of 0 change to 2.

The process continue until the number of simultaneous precipitation deposition site value was reached. It is not necessary that number of site chosen is equivalent to the simultaneous precipitation deposition site value. Two scenarios can cause the difference between simultaneous precipitation deposition site value and actual precipitate deposition. First scenario is the mismatch of cumulative energy value with random number generator generated energy value. Value significantly higher than the maximum value will simply be recorded as no result, thus forgoing potential precipitation deposition chances. Second scenario is repeated match of cumulative value with number generator generated energy

value. With enough opportunity, the chances which random number generator generates the same value multiple times will increase.

3.4 Tortuosity calculation

The calculation of tortuosity is conducted after the precipitate addition C-code was executed. The new file generated by precipitate now includes the value of 2, which represents the precipitate Li_2O_2.

The tortuosity C-code first required an input to the diffusivity values of porous void, active material, and precipitate. Since tortuosity measures the true path to travel between a fixed distances with obstacle, porous void, would be the primary measurement to estimate the value of tortuosity. By using the input one for diffusivity of porous void, zero for diffusivity of active material, and zero for the diffusivity of precipitate, non-dimensonaility and general properties of Fick's law (function 20), could be satisfied.

$$J = -D\frac{\varepsilon}{\tau_n}\frac{\partial c}{\partial n} = -D\frac{\varepsilon}{\tau_n}\left(\frac{c(n=1)-c(n=0)}{1-0}\right) \tag{20}$$

D represents the diffusivity value of the inquired species, ε is the porosity of the microstructure, τ is the tortuosity of the microstructure, c is the concentration of the inquired species, and the domain of the microstructure is designated from n = 0 to n = 1. Diffusivity value, domain size, and porosity are three values satisfied.

In order to solve for tortuosity, governing equation(s) and boundary conditions must be instituted. Conservation of charge dictate the directional flux of Fick's law must be zero, thus a general governing equation, function 21, is established.

$$\nabla \cdot (D \nabla c) = 0 \qquad (21)$$

By evaluating function 21 one direction at a time, tortuosity in each direction can be calculated. In order to impose a unidirectional governing equation, boundary conditions of species diffusion in the other two directions must be zero. Concentration at $n = 0$ is set to be 1 and concentration at $n = 1$ is set to be 0. The difference in value ensure the existence of concentration gradient. Table 8 tabulated the boundary conditions to solve tortuosity.

Table 8. Boundary conditions needed to solve tortuosity

Boundary conditions
$C(n = 0) = 1$
$C(n = 1) = 0$
$\dfrac{\partial c}{\partial n} = 0$

When the boundary conditions are applied to the microstructure, figure 7, a microstructure of porous void would be generated.

80% Initial Porosity   0.2 Precipitation Deposition Preference Coefficient
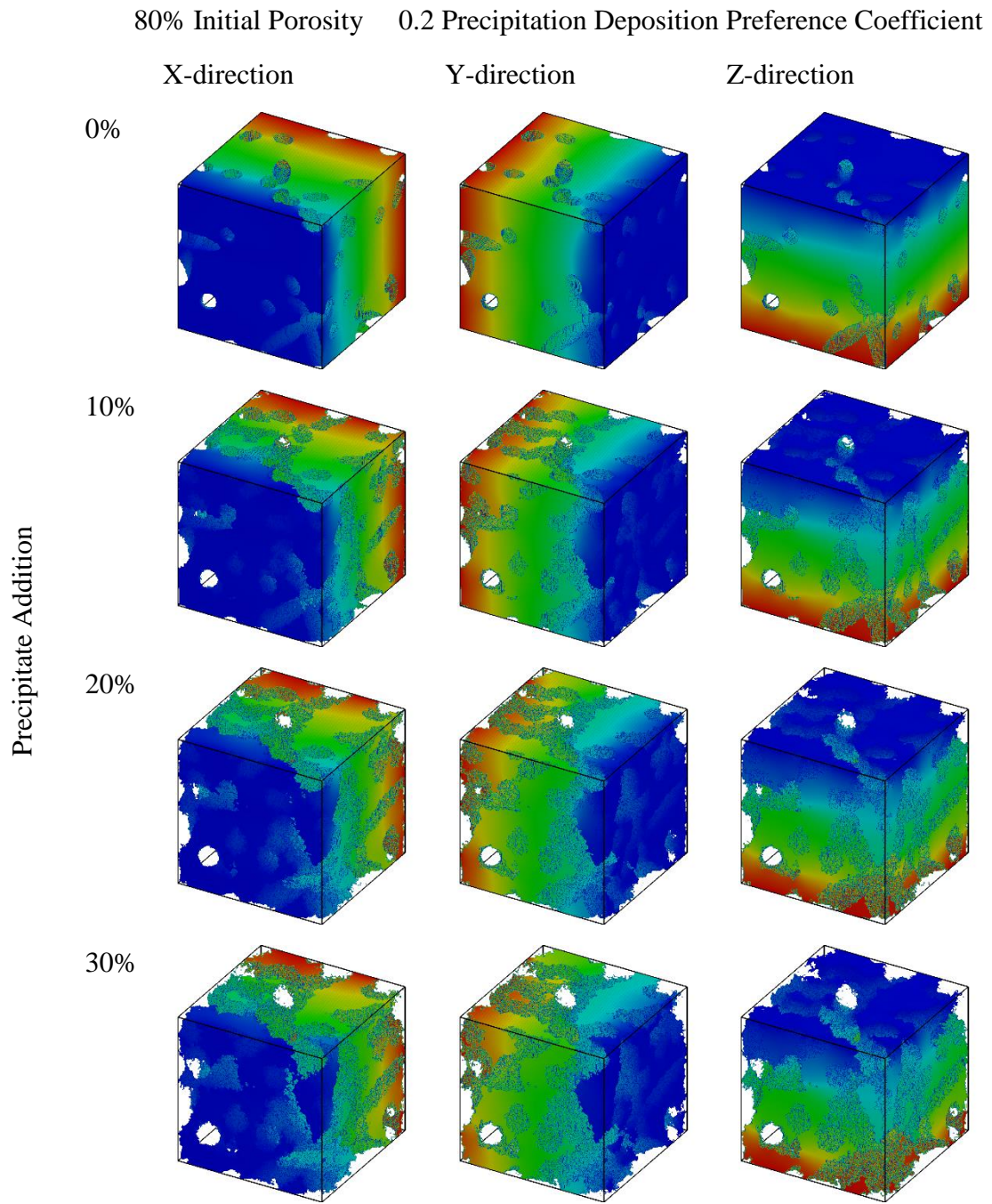
Figure 7. Concentration gradient of microstructure with increasing precipitate deposition in x, y, z direction.

The color red presents concentration of 1 and color blue represent concentration of 0 in figure 7. Initially the structure is extremely porous, thus it can be observed that the microstructure seems like a solid. As precipitate deposition increases, void within the concentration profile increases and the microstructure straies from a perfect solid.

Traditionally the governing equation would be discretized with finite difference method, however, there is a limitation to finite difference method. If a void coordinate under investigation is adjacent to one or more active material, diffusivity value will not be the same for the three coordinates. The condition requires a different analytical method. Figure 8, illustrates one of the condition that finite difference method could not solve.
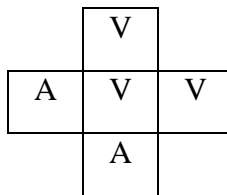
Figure 8. Microstructure orientations which limit finite difference method from solving the flux of species transport. 1 is active material (carbon) and 0 is porous void.

Since the diffusivity value of void is designated as one, the finite difference method would not be able to solve coordinates of active material. Finite volume method is

introduced to resolve the limit that finite difference method had. Instead of solving the governing equation with the diffusivity value of each coordinate, diffusivity value at the interface of active area and void would be used. Function 22 calculates the interfacial diffusivity value between two coordinates,

$$D_{interface} = \frac{2.0 \cdot D_a \cdot D_b}{D_a + D_b + tol} \tag{22}$$

Instead of a uniform diffusivity value, interfacial diffusivity can be applied to adjacent coordinate for evaluation. The variable $D_{interface}$ is the interfacial diffusivity value, D_a is the diffusivity value of the inquired coordinate, D_b is the diffusivity value of the coordinate adjacent to the inquired coordinate, and tol is a tolerance value. The tolerance value was added for the following scenario,
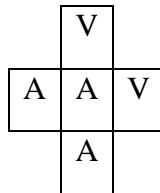
Figure 9. Microstructure orientations which limit interfacial diffusivity value. A is active material (carbon) and V is porous void.

Interface between active material and active material would render $D_{interfeace}$ to 0/0, thus the addition of a significantly small tolerance value would avoid an undefined diffusivity value.

At this point, only the concentration C and τ_n are unknown. The lack of information regarding concentration and tortuosity makes the matrix impossible to solve with traditional linear algebra technique (ie. Matrix inversion). A different mathematical technique, biconjugate gradients stabilized method (BiCGSTAB), is applied to solve the value of tortuosity. The initial guesses for concentration is created by approximating concentration of a complete porous structure in one direction. The approximation essentially generates a linear profile for concentration with the boundary equation mentioned previously. The linear profile would present the necessary data points to initialize the loop.

Once the concentration gradient of the microstructure was calculated, tortuosity of the direction being analyze could be solved. The same method is repeated for other direction of the microstructure.

3.5 Conductivity calculation

The calculation of conductivity is similar to the calculation of tortuosity. The conductivity C-code require an input for the pseudo-conductivity values of porous void, active material, and precipitate. Since conductivity measures the path which allow the

movement of electron, active material and electronically conductive material would be the primary materials to measure conductivity. Precipitate (Li_2O_2) is an insulating material and porous voids do not conduct electricity, therefore only active material will be assigned a pseudo-conductivity value. In order to maintain non-dimensionality of the model, the input for active material's pseudo-conductivity value is one. General properties of charge conservation, function 23, is also satisfied.

$$J = -\sigma_n \frac{\partial \phi}{\partial n} = -\sigma_n \left(\frac{\phi(n=1) - \phi(n=0)}{1-0} \right) \tag{23}$$

The variable σ_n represents the directional-conductivity value of the active material and ϕ represents the electro-potential. The domain of the microstructure is designated from $n = 0$ to $n = 1$. Compared to the tortuosity code, directional conductivity value is variable that still needs to be solved. Since non-dimensionality is implemented, the pseudo-conductivity value of one assigned to active material acts as a multiplication factor to potential gradient.

In order to solve for conductivity, governing equation(s) and boundary conditions must be instituted. Conservation of charge dictate the directional flux of potential gradient must be zero, thus a general governing equation, function 24, is established.

$$\nabla \cdot (\sigma \nabla \phi) = 0 \tag{24}$$

By evaluating function 24 one direction at a time, conductivity in each direction can be calculated. In order to impose a unidirectional governing equation, boundary conditions of potential gradient in the other two directions need to be set to zero. Potential

at n = 0 is set to be 1 and potential at n = 1 is set to be 0. The difference in value ensure the existence of potential gradient. Table 9 tabulated the boundary conditions to solve tortuosity.

Table 9. Boundary conditions needed to solve conductivity

Boundary conditions
$\varphi(n = 0) = 1$
$\varphi\,(n = 1) = 0$
$\dfrac{\partial \phi}{\partial n} = 0$

When the boundary conditions are applied to the microstructure, figure 10, a microstructure of active material and conductive material would be generated.

80% Initial Porosity   0.2 Precipitation Deposition Preference Coefficient
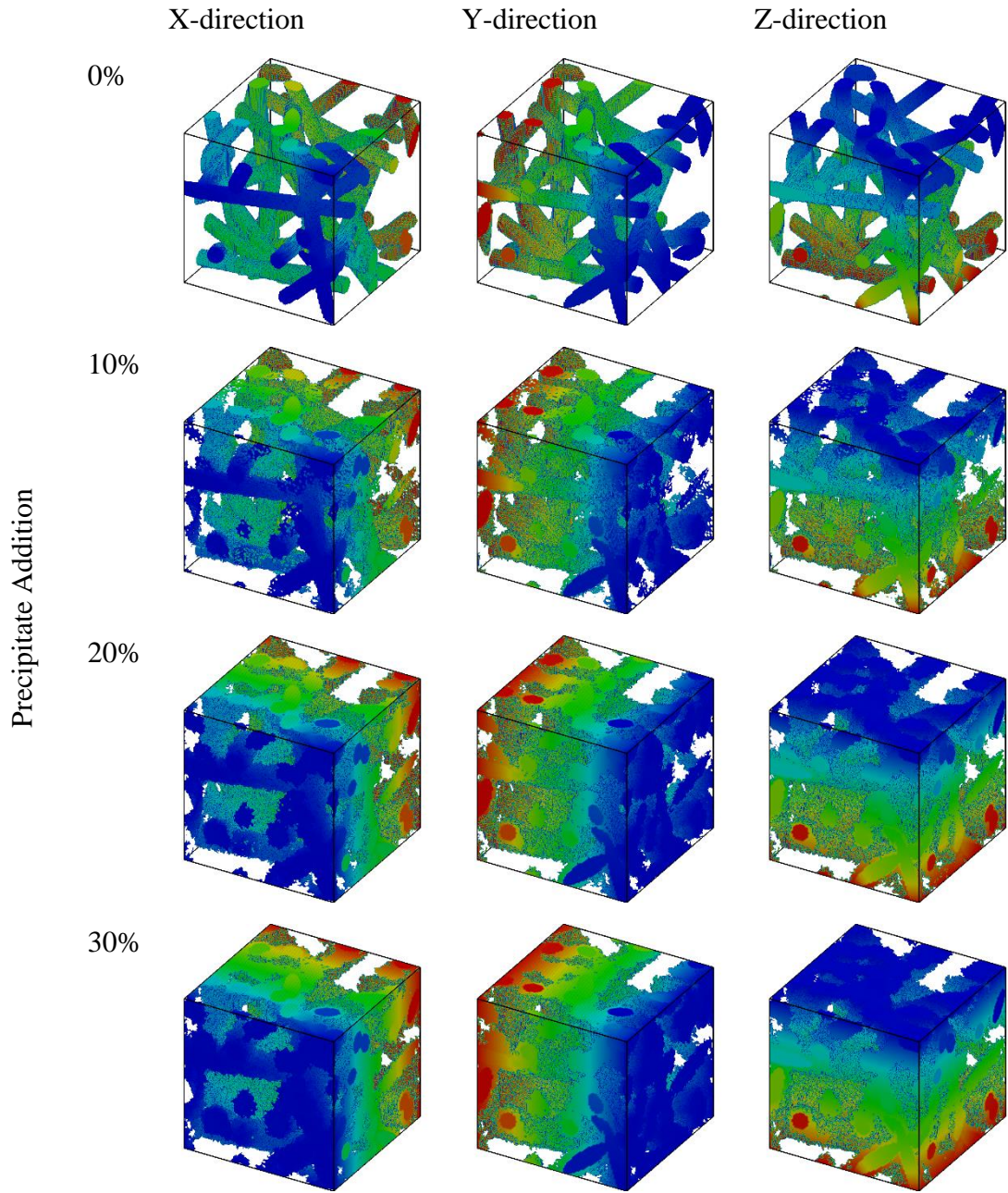
Figure 10. Potential gradient of microstructure with increasing precipitate deposition in x, y, z direction.

The color red presents potential of 1 and color blue represent potential of 0 in figure 10. Initially the structure is only composed with fiber. As precipitate deposition increases, a combination of precipitate and fiber can be seen. Upon close inspection, figure 11, it can be observed that color varies in certain part of the microstructure.
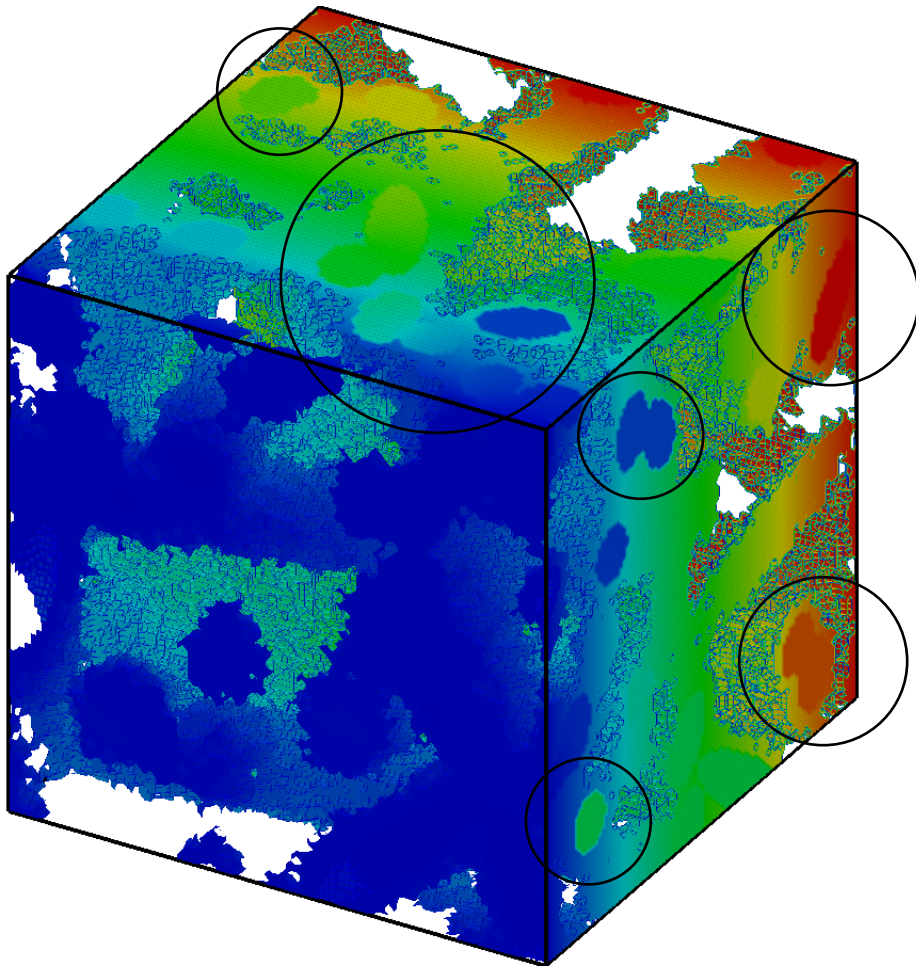
Figure 11. Observable color variation within potential gradient of microstructure of 80% initial porosity, 0.2 precipitation deposition preference coefficient, and 30% precipitation addition.

The color variation stem from difference of conductivity value in boundary condition, function 25.

$$-\sigma_A \frac{\partial \phi}{\partial n} = -\sigma_P \frac{\partial \phi}{\partial n} \tag{25}$$

The variable σ_A represent conductivity of the active material, and variable σ_p represents the conductivity of the precipitate. When the conductivity value of active material is divided on both side of the equation, its value essentially reduces σ_p / σ_A to zero. The lack of variation in color can be explained by lack of potential gradient.

Similar to the calculation of diffusivity value, the pseudo-conductivity value is solved through finite volume method. The interfacial pseudo-conductivity value is calculated with function 26 to avoid problem seen in figure 9.

$$\sigma_{interface} = \frac{2.0 \cdot \sigma_a \cdot \sigma_b}{\sigma_a + \sigma_b + tol} \tag{26}$$

The variables $\sigma_{p\text{-interface}}$ is the pseudo interfacial conductivity value, $\sigma_{p\text{-a}}$ is the pseudo conductivity of the inquired coordinate, $\sigma_{p\text{-b}}$ is the pseudo conductivity of coordinate adjacent to the inquired coordinate, and tol is a tolerance value. The tolerance was added to avoid problem addressed in function 22.

At this point, only the potential φ and σ_n are unknown. The lack of information regarding potential and conductivity makes the matrix impossible to solve with traditional linear algebra technique (ie. Matrix inversion). A different mathematical technique, biconjugate gradients stabilized method (BiCGSTAB), is applied to solve the value of conductivity. The initial guesses for potential is created by approximating potential of a complete porous structure in one direction. The approximation essentially generates a

linear profile for potential with the boundary equation mentioned previously. The linear profile would present the necessary data points to initialize the loop.

Once the potential gradient of the microstructure was calculated, conductivity of the direction being analyze could be solved. The same method is repeated for other direction of the microstructure.

3.6 Statistical study

Before parametric study could be generated, an initial study is conducted to confirm results generated by selected parameter is statistically accurate. Since the immense amount of physical parameters can reduce the efficiency of the study, non-dimensionalization technique is implemented in throughout the studies. All microstructures in the statistical study have 80% porosity.

3.6.1 Fiber length study

The first statistical study conducted is fiber lengths. Before the selection of fiber length, a basic voxel length should be determined. The default voxel length of 1 μm was used to determine the domain size. A discretization of 100 boxes in the x, y, and z directions generated a domain of 100 μm x 100 μm x 100 μm. Basic geometry suggest the

longest length within said box is 173 μm, thus any length beyond can assure uniformity. Six structures with lengths of 250 μm, 375 μm, 500 μm, 625 μm, 750 μm, and 1000 μm are selected. In order to increase accuracy, the microstructures are imposed with 50% precipitate deposition. The six microstructures' physical parameters are tabulated in table 10.

Table 10. Statistical Study of Fiber Length

Fiber Length	x-Tortuosity	y-Tortuosity	z-Tortuosity	Tortuosity	Porosity	Active Material	Secondary
250	3.62309	2.650734	7.521888	4.5985707	29.2034	20.0847	50.7119
375	8.531664	3.321344	3.676953	5.1766537	29.016	20.0557	50.9283
500	3.269287	4.397794	3.663241	3.776774	28.458	20.6045	50.9375
625	4.528975	4.181759	2.760719	3.8238177	28.926	20.169	50.905
750	7.638027	3.550451	4.005006	5.0644947	29.1839	20.0542	50.7619
1000	3.156721	3.705397	5.088339	3.9834857	28.9663	20.2176	50.8161

Since tortuosity is a non-dimensional number, the value can be used to gauge the selection of a fiber length with the highest accuracy. The difference in average tortuosity

value between 500 μm and 625 μm is 0.05. The value is comparatively lower than any other fiber length, thus mean fiber length of 500 μm is selected.

3.6.2 Voxel size study

Voxel size is the non-dimensional resolution of a particular image examined. Large voxel size will decrease voxel length, which refines the quality of the image or object examined. Voxel size is calculated with equation 27, where diameter of the fiber is selected as 10 μm.

$$D_{diameter} = N_{size}\Delta_{voxel} \qquad (27)$$

The problem with selecting an extremely large voxel size, is the increase of computational time. For example, a domain of 100 μm x 100 μm x 100 μm with a voxel length of 1 μm yields a computational size of 1,000,000 boxes, whereas the same domain with voxel length of 0.1 μm yields a computational size of 1000,000,000 boxes. This study will yield a voxel size that is accurate and computational efficient to the overall study. Six structures with voxel sizes 4, 8, 10, 12, 14, and 16 are selected. Figure 12 shows the six structures prior to discharge.
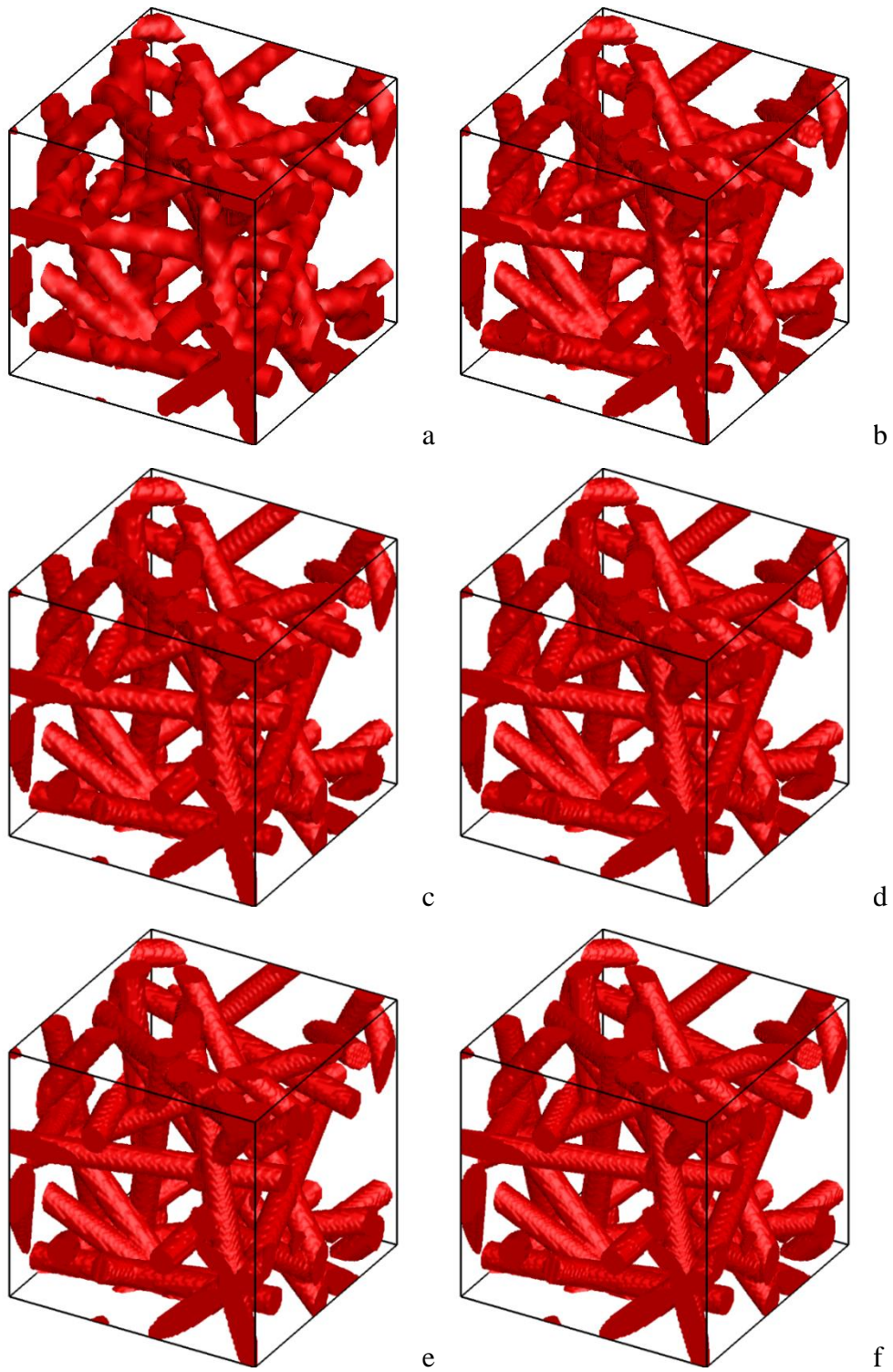
Figure 12. Microstructure with voxel size (a) 4 (b) 8 (c) 10 (d) 12 (e) 14 and (f) 16.

It can be observed that as voxel size increases, the resolution of the microstructure increases. While the pristine microstructures provide physical visualizations, the need to quantify the selection of voxel size remain. In order to increase accuracy, the microstructures are imposed with 50% precipitate deposition. The six microstructures physical parameters are tabulated in table 11.

Table 11. Statistical Study of Voxel Size

D = NΔ	x-tortuosity	y-tortuosity	z-tortuosity	tortuosity	porosity	active material	secondary
4	5.01583	5.807702	5.669862	5.497798	28.9125	20.5875	50.5
8	3.229004	4.87089	3.731486	3.9437933	28.983008	20.588086	50.428906
10	3.269287	4.397794	3.663241	3.776774	28.458	20.6045	50.9375
12	2.930129	3.889783	3.375613	3.3985083	29.033912	20.612037	50.354051
14	2.878261	3.820962	3.255433	3.3182187	28.607981	20.606487	50.785532
16	2.729861	3.686307	3.016117	3.144095	29.123315	20.609839	50.266846

Tortuosity is used to gauge the accuracy for voxel size study. The difference between voxel size 12 and 14 is 0.08, whereas the difference between voxel size 10 and 12 is 0.0.38. The obvious choice for voxel size would be 12 at this point. The problem with selecting voxel size 12 is the voxel length will most likely become an irrational number. In order to avoid such problem, voxel size 10 is selected.

3.6.3 Domain volume study

Domain volume essentially determine the amount of nodal points that will be use to analyze physical parameter of the microstructure. Domain volume has a similar problem to voxel size; overly large domain volume encompass more information at the cost of computational time. Five structures with domain volume 80 x 80 x 80 μm^3, 100 x 100 x 100 μm^3, 120 x 120 x 120 μm^3, 140 x 140 x 140 μm^3, and 160 x 160 x 160 μm^3 are selected. Figure 13 shows the five structures prior to discharge.

Figure 13. Microstructures with domain volume of (a) 80 x 80 x 80 μm^3 (b) 100 x 100 x 100 μm^3 (c) 120 x 120 x 120 μm^3 (d) 140 x 140 x 140 μm^3 and (e) 160 x 160 x 160 μm^3.

It can be observed with increasing domain size, fiber thread counts significantly increased. At the domain value of 160 x 160 x 160 μm^3, the microstructure observed is significantly more complex than the others. The next step is the physical quantification of increased microstructure complexity. In order to increase accuracy, the microstructures are imposed with 50% precipitate deposition. The six microstructures physical parameters are tabulated in table 12.
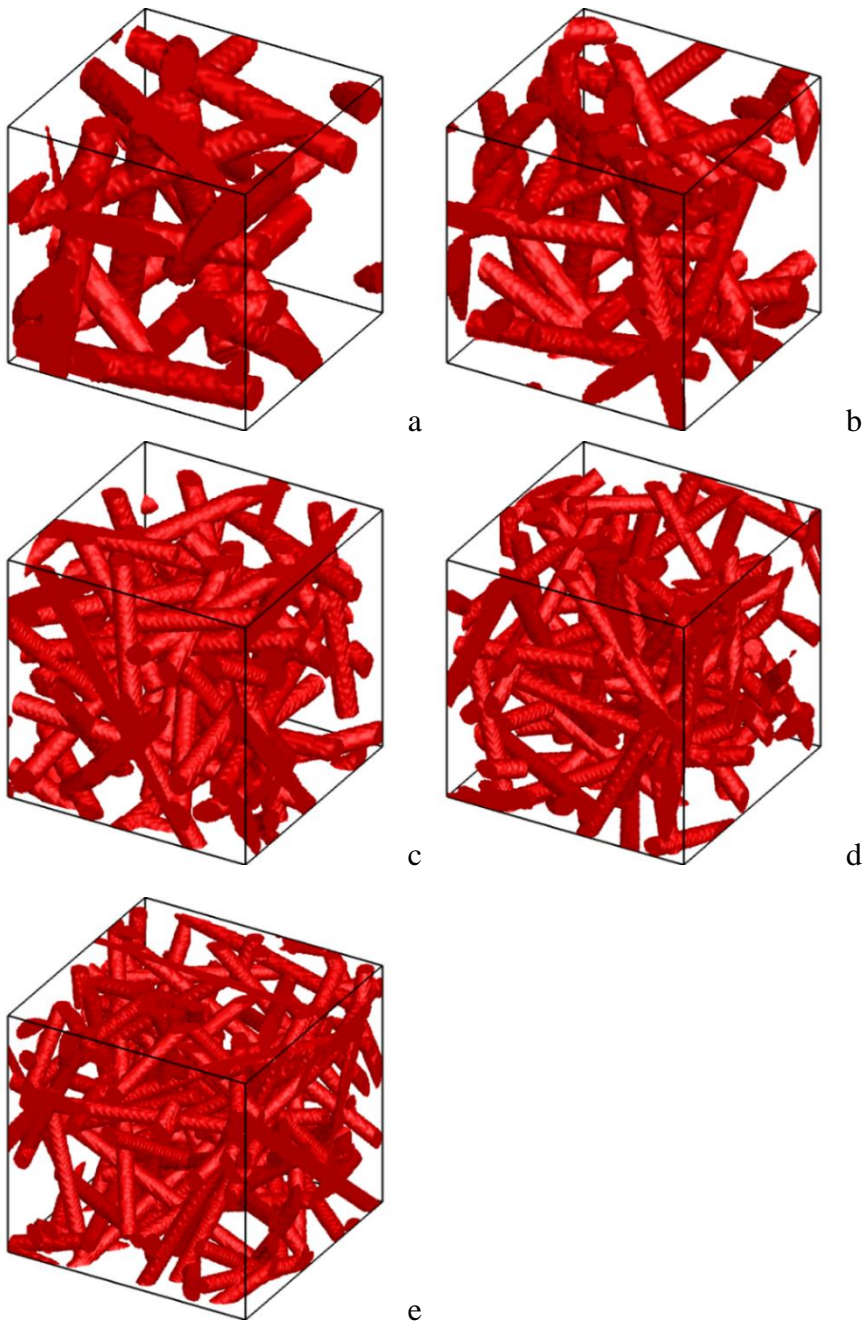
Table 12. Statistical Study of Domain Size

Domain Size	x-tortuosity	y-tortuosity	z-tortuosity	tortuostiy	porosity	active material	secondary
80	3.860448	6.066307	2.925521	4.284092	29.408789	20.567578	50.023633
100	3.269287	4.397794	3.663241	3.776774	28.458	20.6045	50.9375
120	3.60665	3.571363	4.048629	3.742214	28.814584	20.268576	50.91684
140	4.414042	3.863459	3.866841	4.048114	28.984256	20.172595	50.843149
160	5.483803	4.143612	3.80062	4.4760117	29.208252	20.109326	50.682422

Tortuosity, a non-dimensional number, is used to gauge the accuracy of domain size. The average tortuosity between 100 x 100 x 100 μm^3 and 120 x 120 x 120 μm^3 is 0.034 apart. The difference is comparatively lower than any other domain size, thus domain size of 100 x 100 x 100 μm^3 is selected.

At this point, thread length is determined to be 500 μm, voxel size is determined to be 10, and domain size is determined to be 100 x 100 x 100 μm^3.

3.6.4   GeoDict microstructure generation study

In order to dispel any error from GeoDict, a statistical study is conducted by generating seven microstructure with GeoDict. In order to increase accuracy, the microstructures are imposed with 50% precipitate deposition. The seven microstructures physical parameters are tabulated in table 13.

Table 13. Statistical Study of GeoDict Microstructure Generation

runs	x-tortuosity	y-tortuosity	z-tortuosity	tortuosity	porosity	active material	secondary
1	3.269287	4.397794	3.663241	3.776774	28.458	20.6045	50.9375
2	3.17824	4.060006	3.611389	3.616545	28.5385	20.6045	50.857
3	3.171905	4.298506	3.611893	3.6941013	28.5105	20.6045	50.885
4	3.17545	4.057298	3.517088	3.5832787	28.4857	20.6045	50.9098
5	3.139388	4.016787	3.599151	3.5851087	28.5116	20.6045	50.8839
6	3.161899	4.495747	3.585796	3.747814	28.5226	20.6045	50.8729
7	3.265216	4.01017	3.660608	3.6453313	28.4828	20.6045	50.9127

It could be observed that the values of tortuosity fluctuate between 3.776774 and 3.5832787, which correspond to an error of 5.399951%. The error is within acceptable range and reaffirms the accuracy of GeoDict package.

3.6.5   Simultaneous precipitation deposition site factor Study

Simultaneous precipitation deposition site factor is an extremely important value for precipitation addition. The value, as mention in section 3.3.2, determines the number

of site with the potential to turn into precipitate. If the factor is too low, the number of deposition sites increase. Increase to the number of deposition factor will diminish the randomness in precipitation deposition. Repeated value from random number generator will convert potential site into precipitate multiple times. The phenomenon may reduce the spread of deposition.

If the factor is too high, the number of deposition sites decreases. Decrease to the number of deposition sites will diminish the randomness in precipitation deposition in a different method. Since the potential sites drastically decrease, the possibility that every potential sites can change into precipitate significantly increase. The increase change of porous void to precipitate may cause early active area passivation.

Low simultaneous precipitation deposition site value will increase the likeliness of such a scenario. Five structures with simultaneous deposition site factor 25, 50, 100, 200, and 400 are selected. Figure 14 shows the microstructure with 50% precipitation deposition.
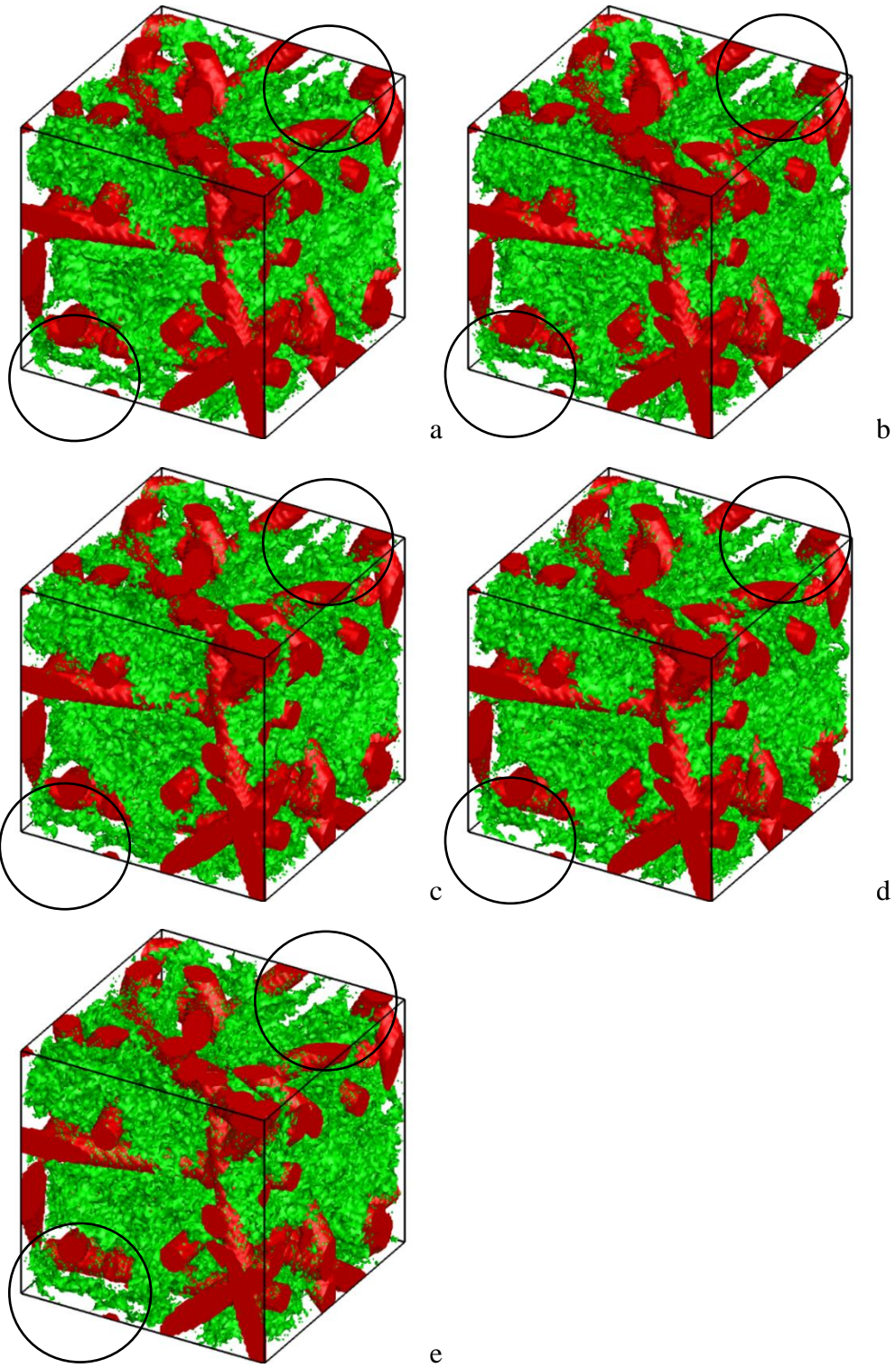
Figure 14. Microstructure with simultaneous deposition site factor of (a) 25 (b) 50 (c) 100 (d) 200 and (e) 400.

At 50% precipitate deposition, distinct feature between the five structures could be seen in the top right corner, and bottom left corner of the structure. At low deposition factor, the number of deposition sites are comparatively higher which causes a smaller void spaces in the bottom left corner. As deposition factor increases, the gap in the bottom left corner continuously decreases. The same phenomenon can be observed in the top right corner of the microstructure. The physical parameters of these five microstructures are tabulated in table 14.

Table 14. Statistical Study of simultaneous deposition site factor

Simultaneous deposition site factor	precipitate porous void interface area	x-tortuosity	y-tortuosity	z-tortuosity	tortuosity	porosity	active material	secondary
by 25	1.2841494	3.130922	4.48761	3.620266	3.746266	26.4315	20.6045	52.964
by 50	1.4432228	3.082293	4.343179	3.586713	3.6707283	28.0613	20.6045	51.3342
by 100	1.5704321	3.269287	4.397794	3.663241	3.776774	28.458	20.6045	50.9375
by 200	1.6180014	3.148344	4.336663	3.57891	3.6879723	28.9199	20.6045	50.4756
by 400	1.6493384	3.098292	4.160514	3.548304	3.60237	29.3728	20.6045	50.0227

The decrease of porous void observed in figure 14 is justified in table 14. As simultaneous deposition site factor increase, the precipitate-porous void interface area continue to increase. While physical observation is confirmed, the need to choose a simultaneous deposition site factor is still present. Similar to the previous studies, tortuosity value is utilized to gauge the accuracy of microstructure. The difference in value between simultaneous deposition factor 50 and 100 is 0.088801. The difference in value between simultaneous deposition factor 100 and 200 is 1.060457. Since the difference of simultaneous deposition factor 100 is comparatively lower, the value will be used to determine simultaneous deposition sites throughout parametric generation.

3.6.6 Precipitation addition C-code study

The last statistical study falls on the accuracy of the precipitation addition c-code. This study would dispel accuracy error associated with the code. A pristine microstructure of 80% porosity, voxel size of 10, and domain size of 100 μm x 100 μm x 100 μm is created. Seven sets of precipitation addition with simultaneous deposition site factor of 100 will be conducted on the particular pristine microstructure. The seven sets of result will yield tortuosity values that can be utilized to gauge to accuracy of the precipitation addition c-code. The physical parameters of these seven precipitation addition are tabulated in table 15.

Table 15. Statistical Study of Precipitation Addition C-Code

runs	x-tortuosity	y-tortuosity	z-tortuosity	tortuosity	porosity	active material	secondary
1	3.269287	4.397794	3.663241	3.776774	28.458	20.6045	50.9375
2	3.22953	4.466544	3.636002	3.7773587	28.5057	20.6045	50.8898
3	3.209636	4.075369	3.611815	3.6322733	28.49	20.6045	50.9055
4	3.109889	3.945238	3.62879	3.5613057	28.5223	20.6045	50.8732
5	3.244805	3.928043	3.528488	3.567112	28.4939	20.6045	50.9016
6	3.243712	4.371006	3.723793	3.7795037	28.5012	20.6045	50.8943
7	3.174143	4.453801	3.635982	3.754642	28.532	20.6045	50.8635

It could be observed that the values of tortuosity fluctuate between 3.779504 and 3.561306, which correspond to an error of 6.126909%. The error might be slightly high, however, is still within acceptable range.

3.7 Parametric generation

From the statistical study, parameters were determined for parametric generation of microstructure. These parameter can be found in table 7. Table 16, 17, 18, and 19 tabulated
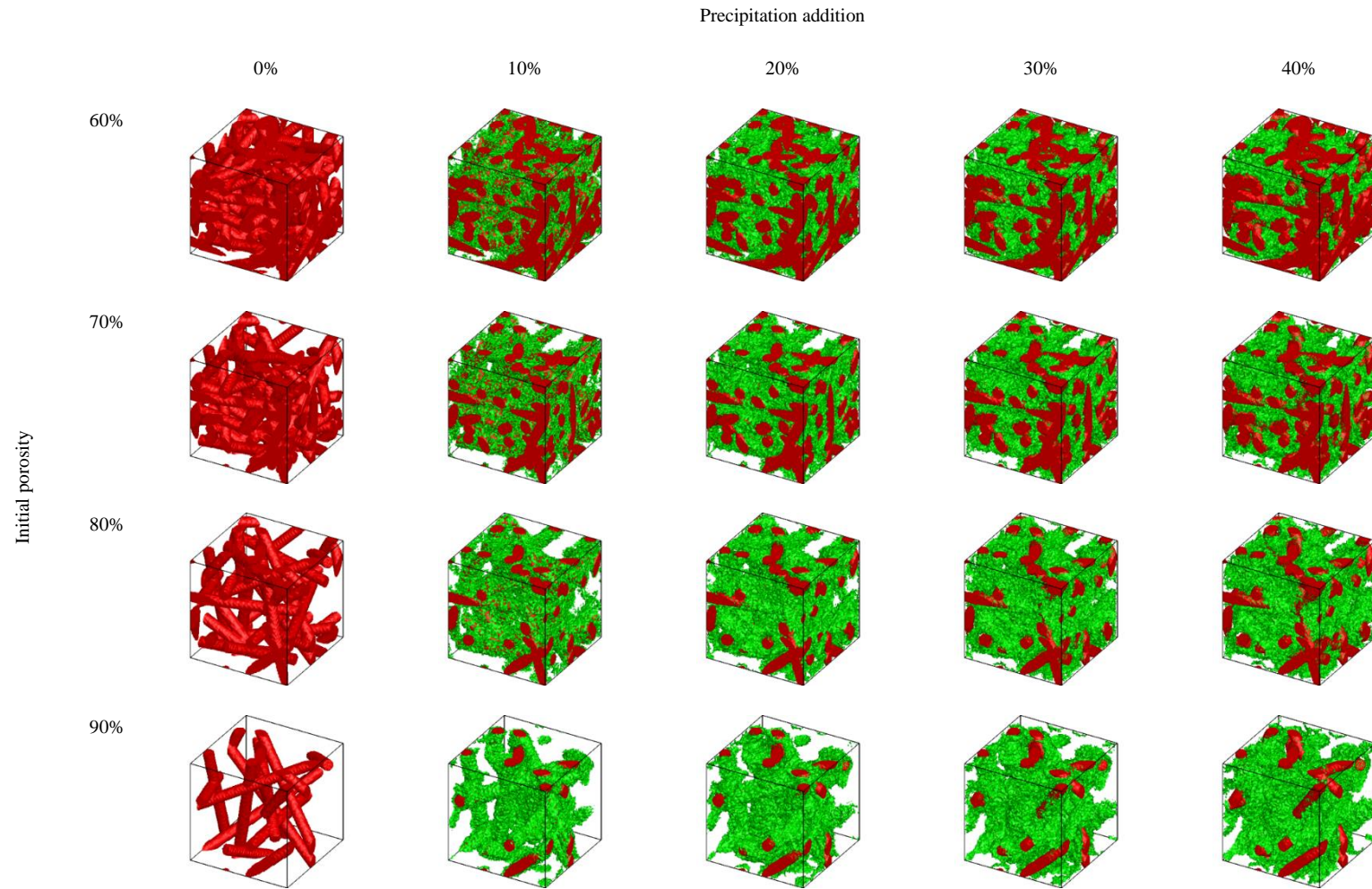
the microstructures with precipitate deposition preference coefficient of 0.2, 0.4, 0.6, and 0.8, respectively. Table 20, 21, 22, and 23 tabulated the microstructures' non-dimensional physical parameters with deposition preference coefficient of 0.2, 0.4, 0.6, and 0.8, respectively.

Variable A01 is the non-dimensional interfacial area between porous void an active material, A12 is the non-dimensional interfacial area between active area and precipitation, and A20 is the non-dimensional interfacial area between precipitate and porous void. Porosity is the difference between initial porosity and precipitate volume deposition. The values calculated for tortuosity and conductivity are the effective tortuosity and effective conductivity of the microstructure.

Table 16. Microstructures with increasing porosity and precipitate deposition of 0.2

Precipitation addition
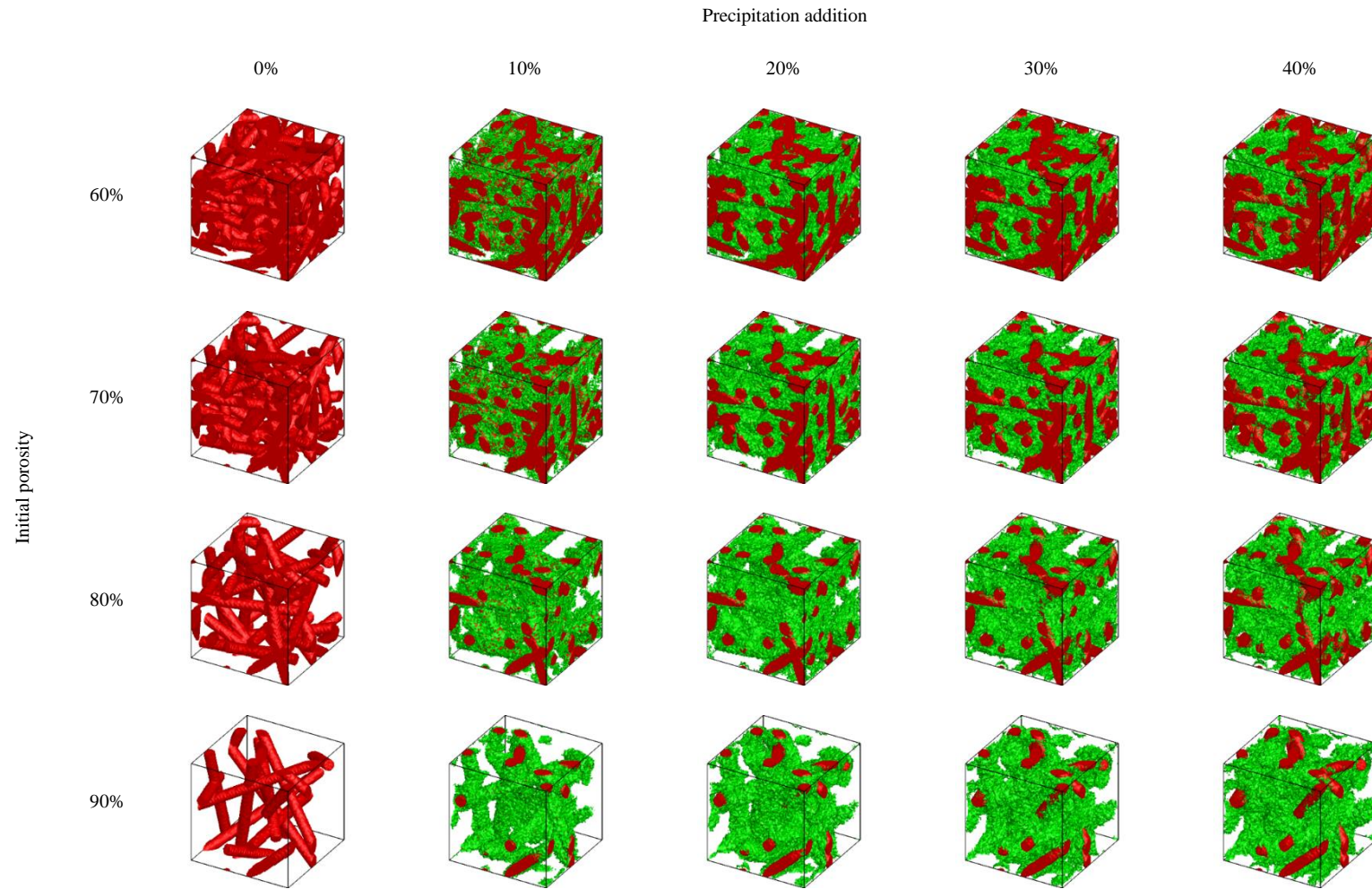
Table 17. Microstructures with increasing porosity and precipitate deposition of 0.4

Precipitation addition

Table 18. Microstructures with increasing porosity and precipitate deposition of 0.6

Precipitation addition

86
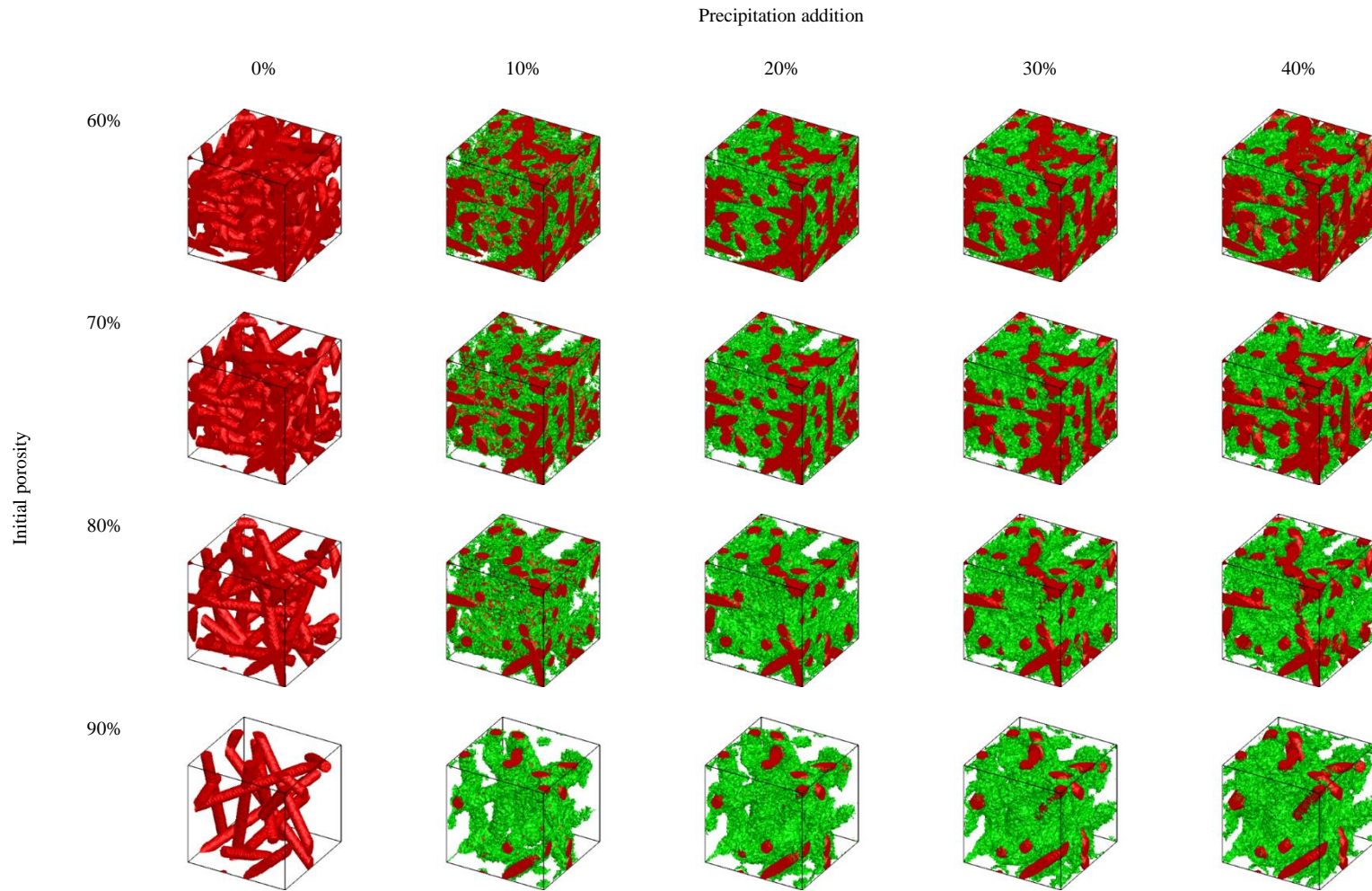
Table 19. Microstructures with increasing porosity and precipitate deposition of 0.8
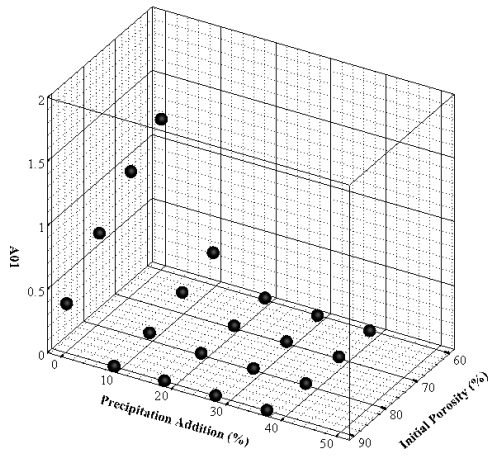
Precipitation addition
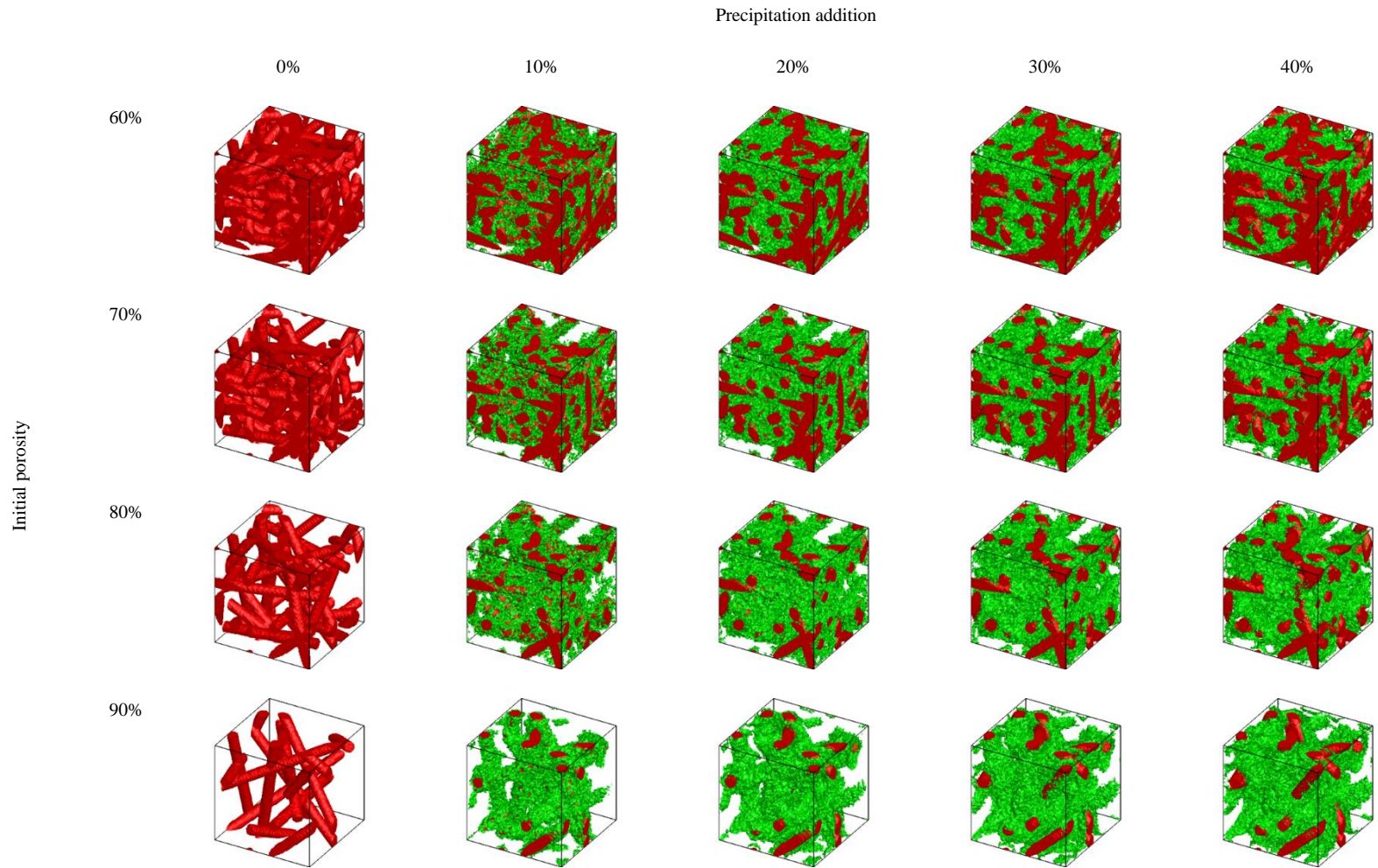
3.8 Microstructure characterization

Data from table 16 to 19 allow correlation between independent variables (porosity, precipitate volume deposition, and precipitate deposition preference coefficient) and dependent variables (active area, tortuosity, and conductivity) to be extracted. The problem with multiple independent variable is the correlation's non-linearity. In order to extract a correlation between the independent variables and dependent variable, the data must be analyze individually. The resulting correlations between individual independent variables and dependent variable would be multiplied to form a single correlation at the end.

3.8.1   Interfacial area between porous void and active material

Interfacial area between porous void and active material is dependent to porosity, precipitate volume deposition, and precipitate deposition preference coefficient. At an initial glance, figure 15, active area decreases with increasing initial porosity.
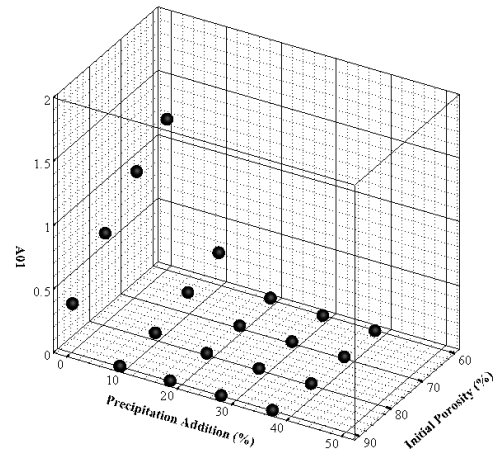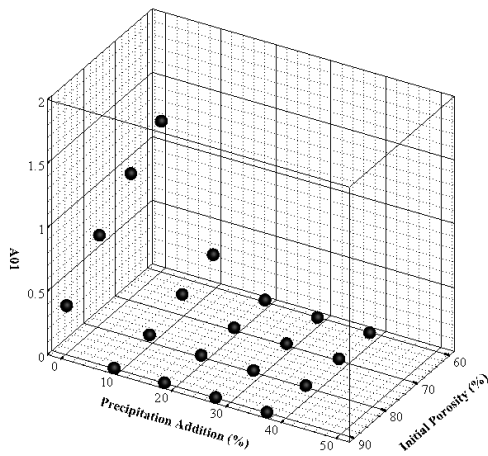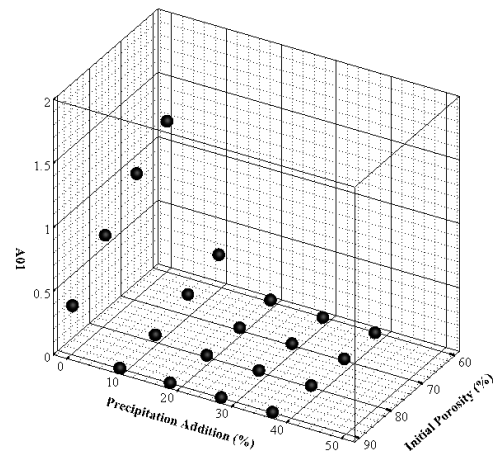
Figure 15. General trend between interfacial area and independent variables of initial porosity, precipitation, and precipitate deposition preference coefficient of (a) 0.2 (b) 0.4 (c) 0.6 and (d) 0.8.

A general polynomial trend could be observed between initial porosity and interfacial area. In order to avoid over-generalization, the correlation between initial

porosity and interfacial area is estimated to be a second order polynomial equation. The trend between precipitation addition and interfacial area is slightly more complex. The trend could be interpret as a decaying exponential function, logarithmic function, power function, and polynomial function. The proper selection of correlation will depend on two factors: dependency on precipitate deposition preference coefficient and regression value of the resulting correlation. Similar trend is also observed between interfacial area and precipitate deposition preference coefficient. Function 28, which correlate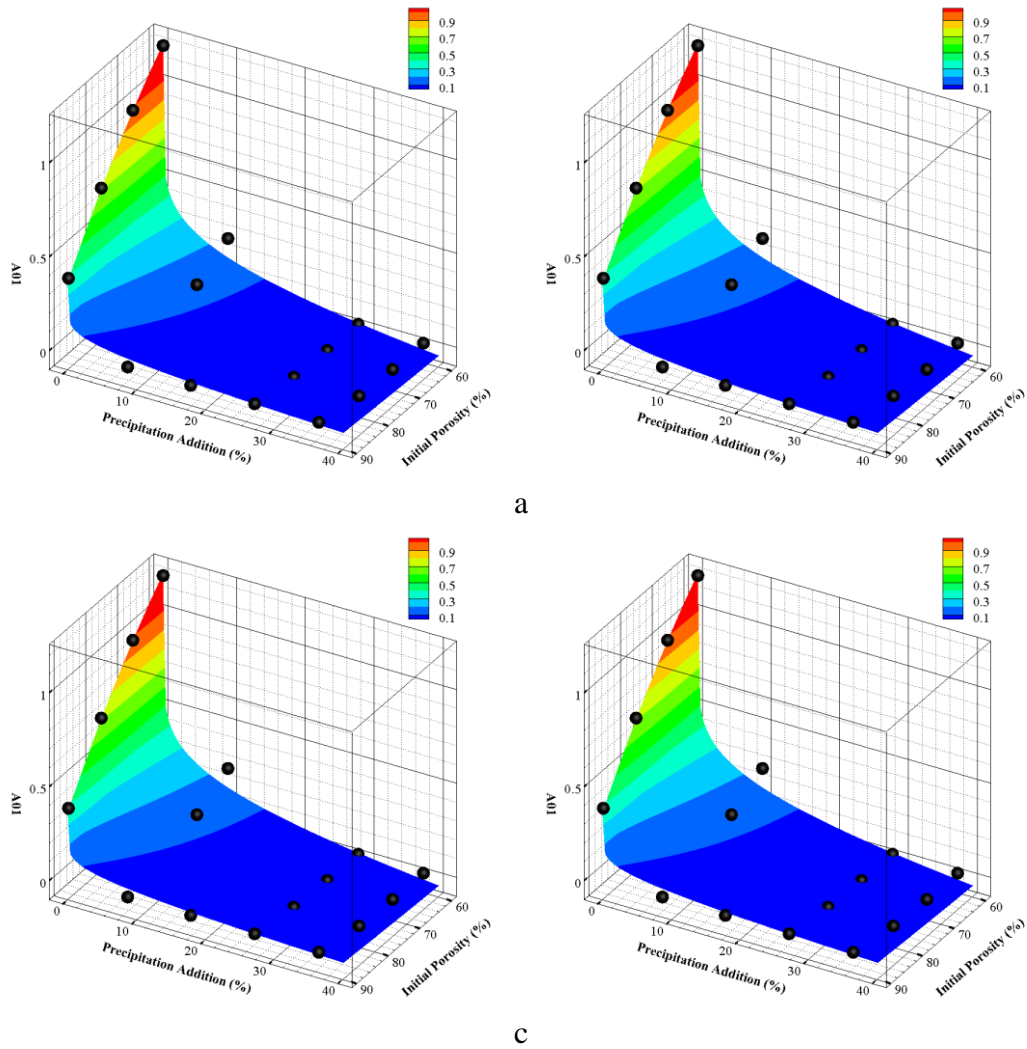 interfacial area to porosity, volume percentage of precipitate deposition, and precipitate deposition preference coefficient was determined after a few trials.

$$A_{01} = \{p_0 + [p_1(1-\varepsilon_0)] + [p_2 \cdot (1-\varepsilon_0)^2]\} \cdot \left[1 - \frac{\varepsilon_2}{p_3 + (p_4 \cdot \omega^{p_5})}\right]^{p_6} \qquad (28)$$

The variable a01 is the interfacial area between porous void and active material, ε_0 is the initial porosity of the microstructure, ε_2 is the volume percentage of precipitate added to the microstructure and ω is the precipitate deposition preference coefficient. The function ensure interfacial active area is only a function of initial porosity when volume percentage of precipitate deposition is zero. The function also ensure active area become zero when volume percentage of precipitate deposition approach its limit. When the proposed function was fitted against microstructure data, regression value (R^2) of 0.9896 was calculated. Figure 16 shows the fitted value versus the actual value.

Figure 16. Fitted value v. actual value of interfacial area between porous void and active material. Fitted trend between interfacial area and independent variables of initial porosity, precipitation, and precipitate deposition preference coefficient of (a) 0.2 (b) 0.4 (c) 0.6 and (d) 0.8.

It could be observed few actual value strayed from the predicted curve, which explains that regression value (R^2) of 0.9896.

3.8.2 Tortuosity of microstructure

Tortuosity of microstructure is dependent to porosity, precipitate volume deposition, and precipitate deposition preference coefficient. At an initial glance, figure 17, tortuosity decreases with increasing initial porosity.

Figure 17. General trend between tortuosity and independent variables of initial porosity, precipitation, and precipitate deposition preference coefficient of (a) 0.2 (b) 0.4 (c) 0.6 and (d) 0.8.

The correlation between initial porosity and tortuosity faces is difficult to comment on initially since the trend could be interpret as a decaying exponential function,

logarithmic function, power function, and polynomial function. The same problem can also be observed for correlation between tortuosity and precipitation addition. Both trend, however, exhibit polynomial like trend when initial porosity approaches 90%. The proper selection of correlation will depend on two factors: dependency on precipitate deposition preference coefficient and regression value of the resulting correlation. Function 29, which correlate tortuosity to porosity, volume percentage of precipitate deposition, and precipitate deposition preference coefficient was determined after a few trials.

$$a = t_0 + \{\varepsilon_2 \cdot [t_1 + (t_2 \cdot \varepsilon_2) + (t_3 \cdot w)]\}$$
$$b = t_4 + \{\varepsilon_2 \cdot [t_5 + (t_6 \cdot \varepsilon_2) + (t_7 \cdot w)]\} \quad\quad\quad (29)$$
$$\tau = a \cdot (\varepsilon 0 - \varepsilon 2)^b$$

The variable τ is the tortuosity of the microstructure, ε_0 is the initial porosity of the microstructure, ε_2 is the volume percentage of precipitate added to the microstructure and ω is the precipitate deposition preference coefficient. The function ensure interfacial active area is only a function of initial porosity when volume percentage of precipitate deposition is zero. The function also ensure active area become zero when volume percentage of precipitate deposition approach its limit. When the proposed function was fitted against microstructure data, regression value (R^2) of 0.9648 was calculated. Figure 18 shows the fitted value versus the actual value.
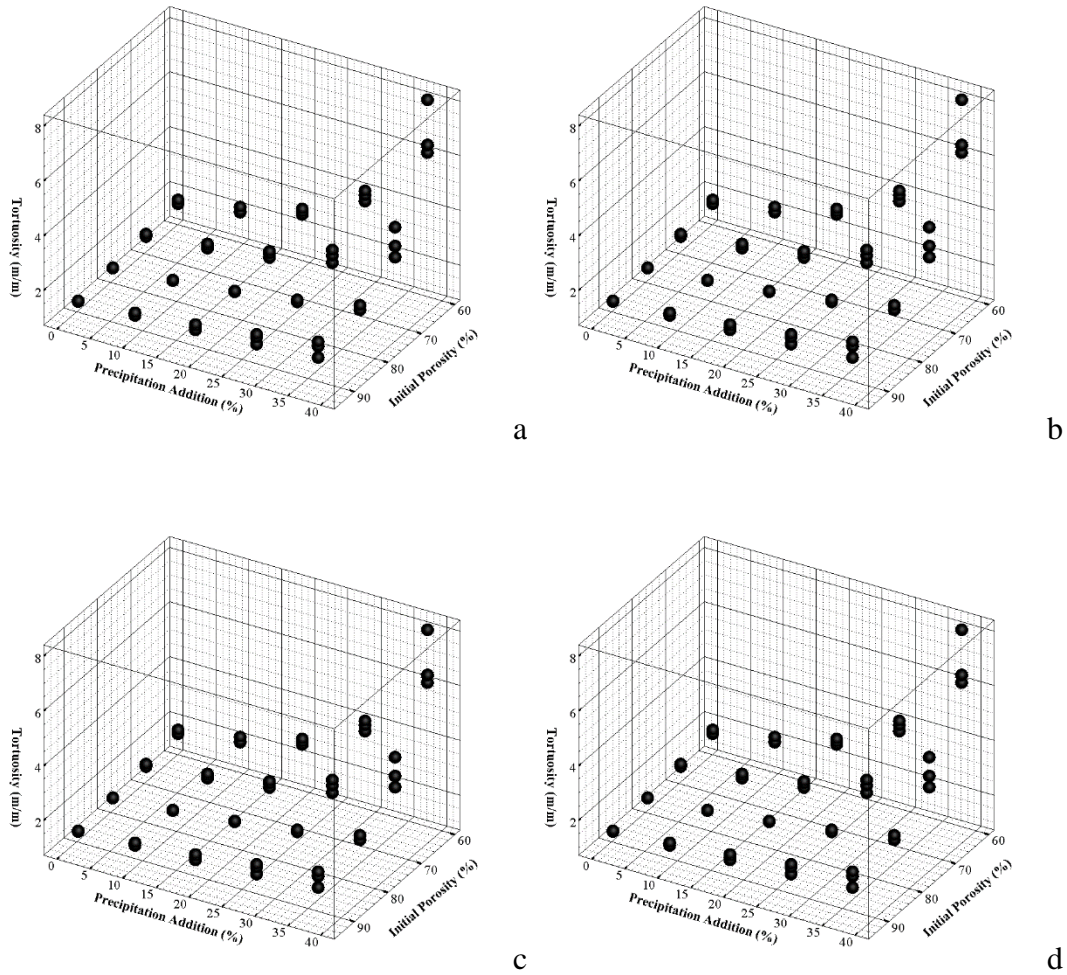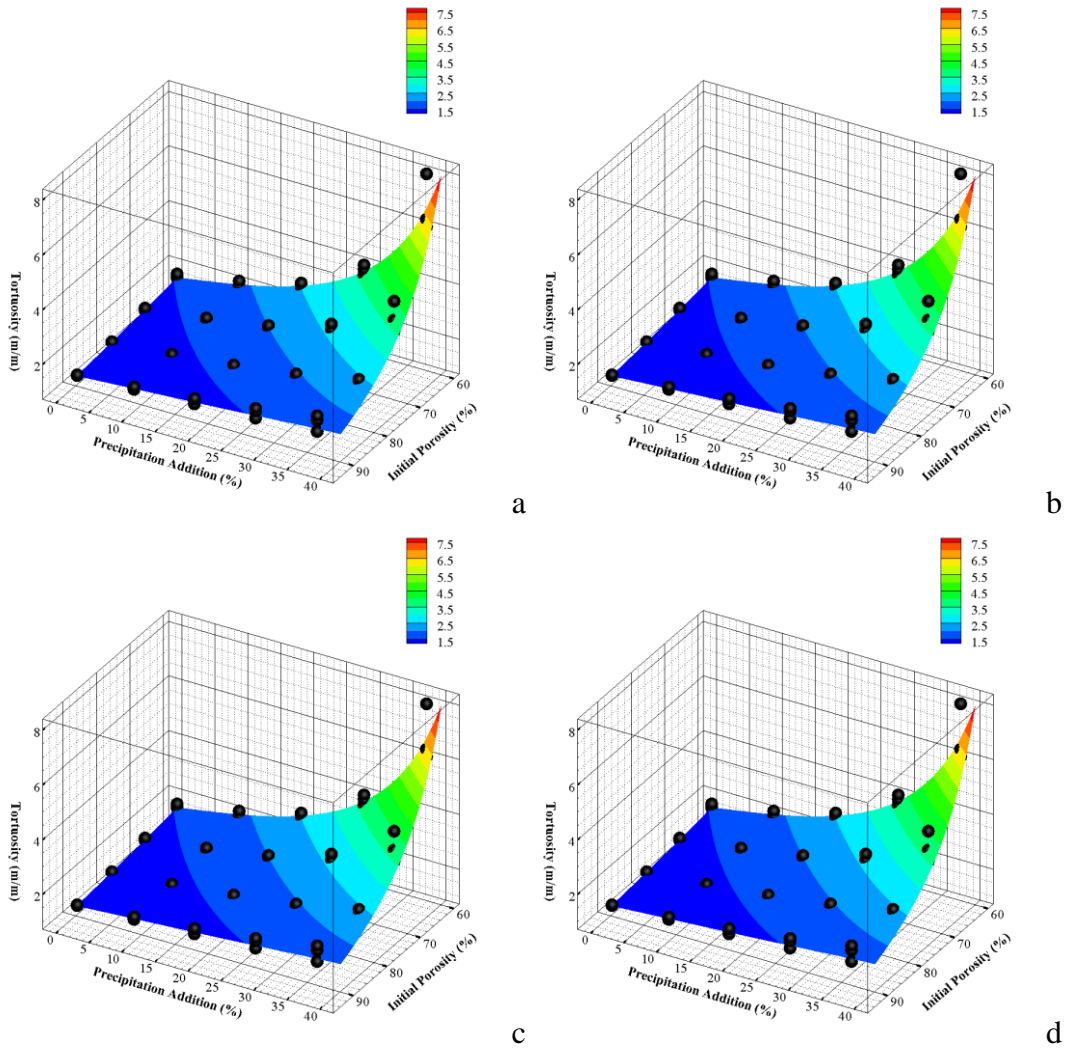
Figure 18. Fitted value v. actual value of tortuosity. Fitted trend between tortuosity and independent variables of initial porosity, precipitation, and precipitate deposition preference coefficient of (a) 0.2 (b) 0.4 (c) 0.6 and (d) 0.8.

3.8.3 Effective conductivity of microstructure

Effective conductivity of microstructure is dependent to initial porosity. Since precipitate act as an insulating material, the effective conductivity of the microstructure would not change regardless of the amount of precipitate added. At an initial glance, figure 19, no changes was observed with increasing precipitation addition.
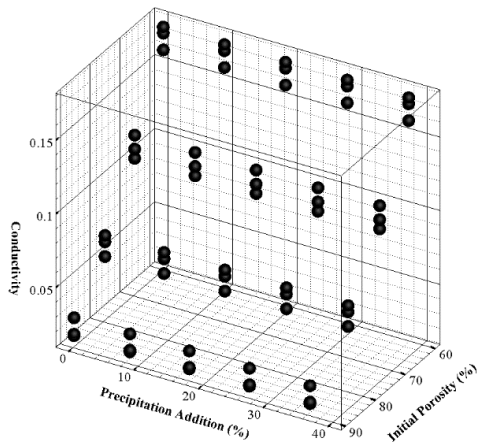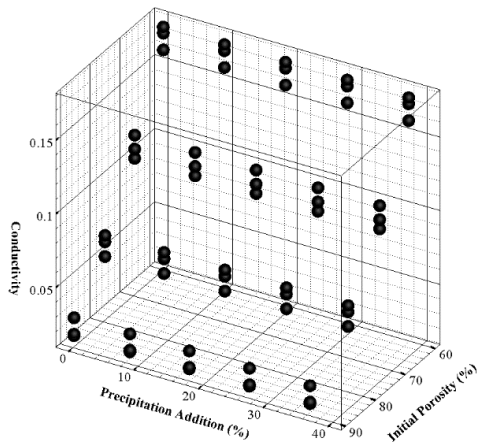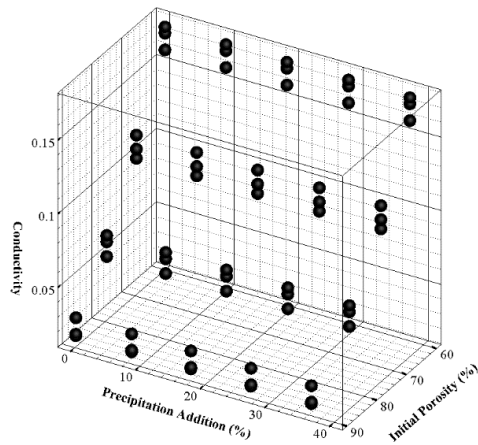
Figure 19. General trend between effective conductivity and independent variables of initial porosity, precipitation, and precipitate deposition preference coefficient of (a) 0.2 (b) 0.4 (c) 0.6 and (d) 0.8.

It can be observed that precipitate deposition preference coefficient and precipitate addition have no influence over a microstructure effective conductivity. While the

function only rely on initial porosity, no comment can be made on the functional form between initial porosity and effective conductivity. The correlation between initial porosity and tortuosity faces is difficult to comment on initially since the trend could be interpret as a decaying exponential function, logarithmic function, power function, and polynomial function. The proper selection of correlation will depend on regression value of the resulting correlation. Function 30, which correlate effective conductivity to initial porosity was determined after a few trials.

$$\sigma = \left[s_0 \cdot \left(1 - \varepsilon_0\right)^{s_1} \right] \tag{30}$$

The variable τ is the effective tortuosity of the microstructure and ε_0 is the initial porosity of the microstructure. The function ensure effective conductivity is 0 if the microstructure is completely porous. It also ensure the microstructure attain it conductivity value if the structure is a non-porous solid. When the proposed function was fitted against microstructure data, regression value (R^2) of 0.9874 was calculated. Figure 20 shows the fitted value versus the actual value.
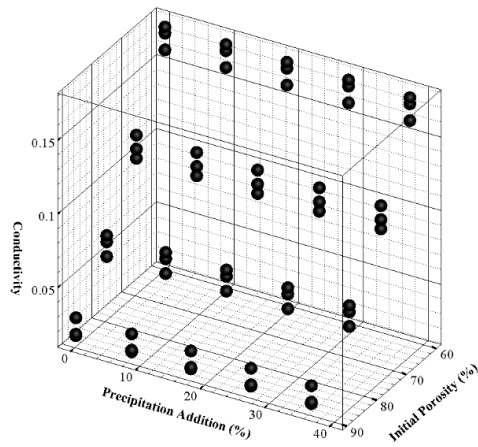
Figure 20. Fitted value v. actual value of effective conductivity. Fitted trend between effective conductivity and independent variables of initial porosity, precipitation, and precipitate deposition preference coefficient of (a) 0.2 (b) 0.4 (c) 0.6 and (d) 0.8.
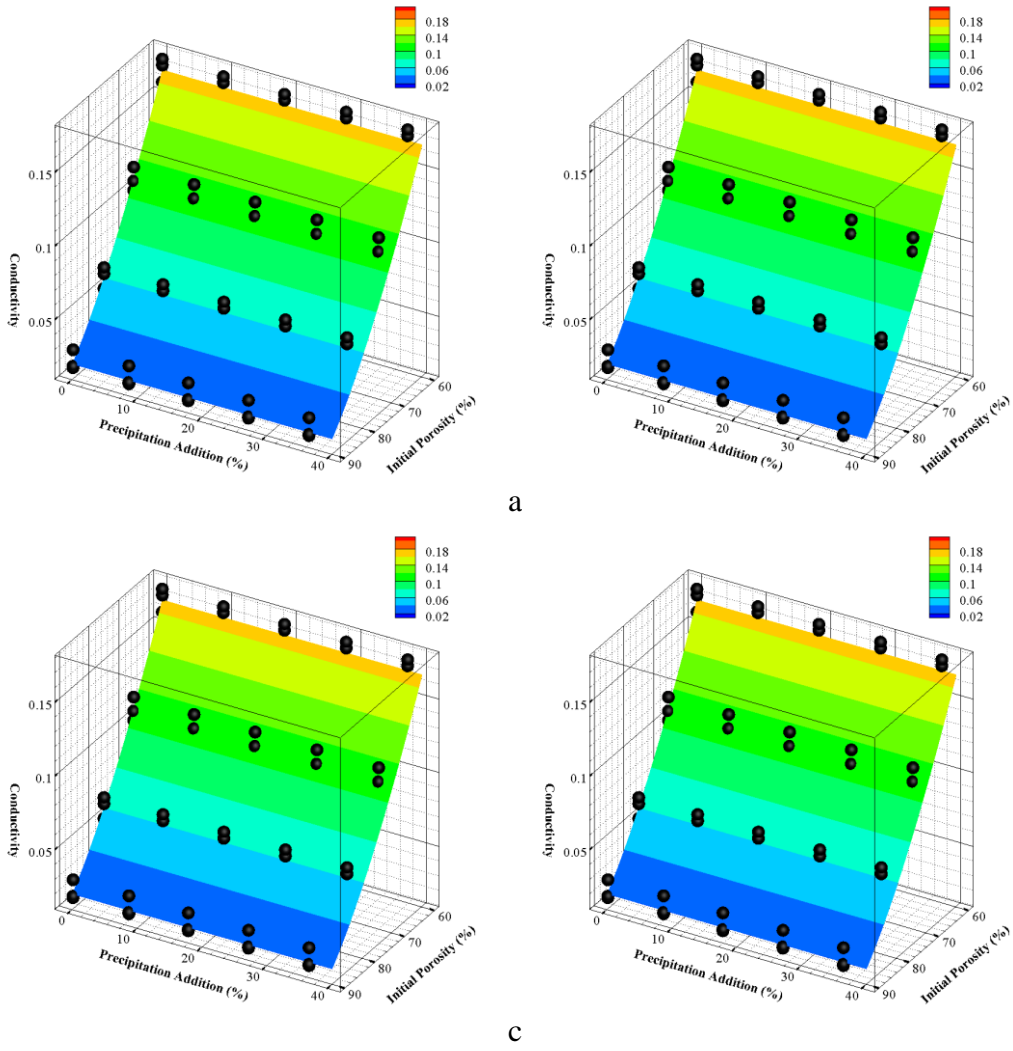
Similar to the trend observed in the actual value, the fitted values have no variation with changing precipitation addition and precipitate deposition preference coefficient.

3.9 Discharge calculation analysis

The discharge performance calculation utilized three form of governing equations and one constitutive equation which connect the three governing equation. Species conservation, function 31, account for species diffusion due to apply current density.

$$\frac{\partial}{\partial t}(\varepsilon C_i) = \frac{\partial}{\partial x}(D_i \frac{\partial C_i}{\partial x}) + \frac{\partial}{\partial x}(z_i F \frac{D_i}{RT} C_i \frac{\partial \phi_e}{\partial x}) + R_i$$
$$i = Li^+, A^-, O_{2(l)}$$
(31)

The variable ε is the porosity of the microstructure, C_i is species concentration, D_i is the effective diffusivity of the microstructure, z_i is the charge of the species, F is the faraday constant, R is the gas constant, T is the operational temperature, φ_e is the electrolyte potential, A^- is the anion of lithium salt in electrolyte, Li^+ is lithium-ion, $O_{2(l)}$ is oxygen diffused in electrolyte, and R_i is consumption of oxygen and lithium species by the system.

Charge conservation in electrolyte phase, function 32, assured charged species diffusing through separator are accounted for.

$$\sum_i \left\{ \frac{\partial}{\partial x}\left(z_i^2 F^2 \frac{D_i}{RT} C_i \frac{\partial \phi_e}{\partial x} \right) + \frac{\partial}{\partial x}\left(z_i FD_i \frac{\partial C_i}{\partial x} \right) \right\} + aj_c = 0$$
$$i = Li^+, A^-, O_{2(l)}$$
(32)

The variable C_i is species concentration, D_i is the effective diffusivity of the microstructure, z_i is the charge of the species, F is the faraday constant, R is the gas constant, T is the operational temperature, φ_e is the electrolyte potential, a is the interfacial area of the electrode, and j_c is the current density.

Charge conservation in solid phase, function 33, assured migration of electron and diffusion of charge species are accounted for.

$$\sigma_c \frac{\partial^2 \phi_c}{\partial x^2} = a j_c \tag{33}$$

The variable σ_c is the effective conductivity of the positive electrode (cathode) and ϕ_c is the cathodic potential. Porosity within the microstructure, function 34 and 35, changes over time due to apply current density. The overall change in porosity with respect to time is zero when added to rate at which volumetric precipitate generates.

$$\frac{\partial \varepsilon_{Li_2O_2}}{\partial t} = -V_{Li_2O_2} \frac{j_c}{2F} \tag{34}$$

$$\frac{\partial \varepsilon}{\partial t} + \frac{\partial \varepsilon_{Li_2O_2}}{\partial t} = 0 \tag{35}$$

Effective transport property, electrolyte potential, and species concentration are discretized with finite volume method in an implicit scheme to assure stabilization.

3.9.1 Boundary conditions

The second order nature of the three governing equations employed, will require two corresponding boundary conditions per governing equation to satisfy the solution. The boundary conditions are correlated to species diffusion and potential flux of each phases.

Figure 21 provides visualization to species diffusion path and electron migration within the lithium air battery.

$$O_{2(g)} \underset{\text{evolution}}{\overset{\text{dissolution}}{\rightleftharpoons}} O_{2(l)}$$

Li anode

Separator

Graphite cathode

Ni mesh

anode : $Li \underset{\text{charge}}{\overset{\text{discharge}}{\rightleftharpoons}} Li^+ + e^-$

cathode : $\dfrac{1}{2} Li_2O_{2(s)} \underset{\text{discharge}}{\overset{\text{charge}}{\rightleftharpoons}} Li^+ + \dfrac{1}{2} O_{2(l)} + e^-$
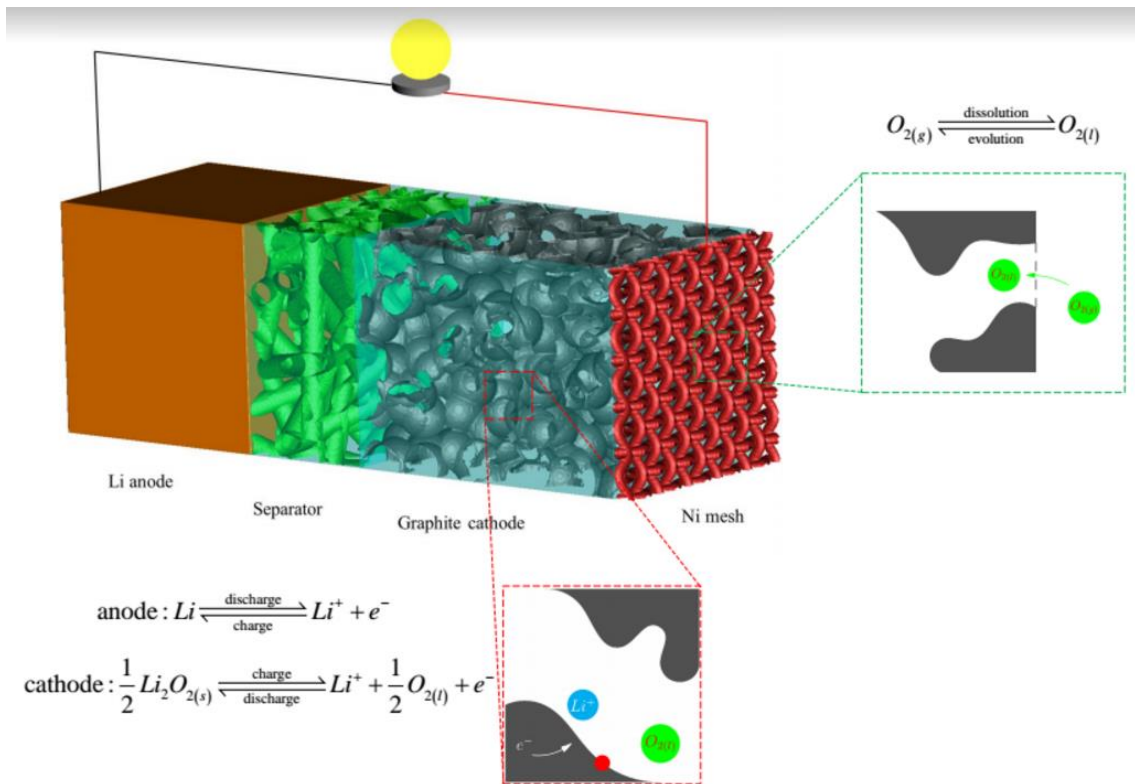
Figure 21. Schematic to lithium air battery and visualization to species diffusion path and electron migration within the lithium air battery

3.9.1.1 Lithium Anode – separator – interface

Conventional separator is made with an insulating material to prevent internal short circuit of any battery. The insulating nature of the material ensure zero current density pass through the separator. The separator, however, must be porous enough for species to diffuse. Table 20 tabulated the boundary condition at the lithium anode – separator – interface.

Table 20. Boundary condition at the lithium anode – separator – interface

Boundary Condition	
$-D^0_{Li^+} \dfrac{\varepsilon}{\tau} \dfrac{\partial C_{Li^+}}{\partial x} = \dfrac{J_{app}}{F}$	(1)
$\dfrac{\partial C_{A^-}}{\partial x} = 0$	(2)
$\dfrac{\partial C_{O_2}}{\partial x} = 0$	(3)
$\dfrac{\partial \phi_c}{\partial x} = 0$	(4)
$\dfrac{\partial \phi_e}{\partial x} = 0$	(5)

Lithium-ion diffuses through the boundary due to an apply current density which explain boundary condition 1. Since anion species is exclusive within the separator, species diffusion at the interface is zero. Oxygen is only present within the cathode-nickel mesh interface which suggest a concentration flux of oxygen is close to zero. Potential flux of cathode and potential flux of electrolyte is representative to electron migration, thus potential gradient would not exist at the interface.

3.9.1.2 Carbon paper cathode – separator – interface

The only difference between carbon paper cathode – Separator – Interface and lithium Anode – Separator – Interface is the sign of boundary condition 1 of table XX, which should be positive on the separator side since lithium is diffusing away from the boundary.

The boundary condition remain the same, however, on the cathode side of the interface.

3.9.1.3 Carbon paper cathode – current collector – interface

Boundary condition at the carbon paper cathode – current collector – interface is slightly different. Since the current collector is open to oxygen environment, oxygen diffusion is no longer zero. Another difference is the electron migration at the current

collector interface. Table 21 tabulated the boundary condition at the carbon paper cathode – current collector – interface.

Table 21. Boundary condition at the carbon paper cathode – current collector – interface

Boundary Condition	
$\dfrac{\partial C_{Li^+}}{\partial x} = 0$	(1)
$\dfrac{\partial C_{A^-}}{\partial x} = 0$	(2)
$-D_{O_2}^0 \dfrac{\partial C_{O_2}}{\partial x} = k_d(C_{O_2} - K_H p)$	(3)
$-\sigma_c \dfrac{\partial \phi_c}{\partial x} = J_{app}$	(4)
$\phi_e = 0$	(5)

Diffusion of Lithium-ion at the carbon paper cathode – current collector is zero, since precipitation occurs in the cathode region. Since anion species is exclusive within the separator, species diffusion at the interface is zero. Diffusion of oxygen depend on diffusivity of oxygen D_{O2}, kinetics of the reaction k_d, concentration of oxygen C_{O2}, and solubility of oxygen with partial pressure of atmospheric surrounding (K_H is Henry's

constant, p is partial pressure). Migration of electron from anode to the cathode suggest a dependency to apply current density. The variable σ_c is the conductivity of the carbon paper and J_{app} is the apply current density. Electrolyte potential difference is zero at the interface.

3.9.2   Initialization with current density

The calculation of lithium air battery discharge performance starts with current density. Current density is not only linked to the governing equation, it also linked to the precipitate deposition preference coefficient. This is significant to the overall model as precipitate deposition preference coefficient is linked to the interfacial area correlation, and tortuosity correlation. A correlation between precipitate deposition preference coefficient and current density is needed.

Griffith et al reported a carbon loading of 13.3 m^2 g^{-1} for the carbon electrode employed. Assuming the fiber electrode have the same density as carbon (2.25 g cc^{-1}), the equivalent interfacial area is calculated to be 2.9925 x 10^7 m^2 m^{-3}. Interfacial current density can be calculated, function 36, by dividing apply current density by interfacial area.

$$i = \frac{J_{app}}{7481.25} \qquad (36)$$

Griffith et al also reported the cumulative amount of Li_2O_2 formed with respect to discharge current density. With a known current density which correlated to ε_{Li2O2}, a correlation between precipitate deposition preference coefficient and current density can be formed. Table 22 tabulated apply current density, interfacial current density, total product volume and volume percentage of precipitate founded in the report.

**Table 22.** Precipitation volume found with respect to apply current density

Apply Current Density [A m^{-2}]	Interfacial Current Density [A m^{-2}]	Total Product Volume [mm^3]	Volume Percentage of Precipitate
1	1.336675 E -4	5.7 ± 0.9	0.0962
2	2.673350 E -4	3.6 ± 0.6	0.0626
5	6.683375 E -4	1.9 ± 0.4	0.0337
10	1.336675 E -3	1.5 ± 0.6	0.0241

Early implementation of precipitate deposition preference coefficient normalized the value between 0 and 1. Modification to volume percentage of precipitate to a value between 0 and 1 would allow a nonlinear regression. Function 39 is a correlation extracted

from nonlinear regression of independent variable interfacial current density and dependent variable precipitate deposition preference coefficient.

$$\omega = \frac{1.0688 \cdot 10^{-4}}{i} + 0.1817 \tag{37}$$

A regression value (R^2) of 0.9981 was calculated for function 37. Figure 22 shows the fitted data against actual data.
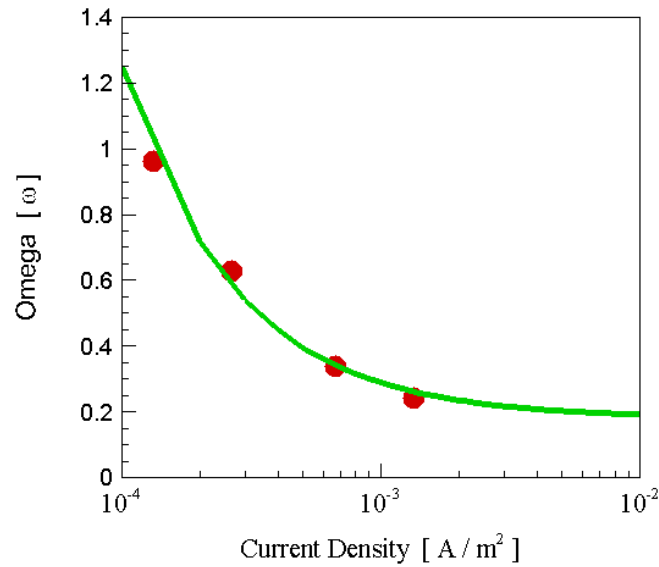
Figure 22. Fitted value v. actual value of precipitate deposition preference coefficient as a function of interfacial current density

The correlation allows an automatic calculation of precipitate deposition preference coefficient with an input of apply current density.

3.9.3   Model input condition

Input condition of the model is tabulated in table 23.

Table 23. Input condition of the model

T	[K]	300
Ja_{ref}	[A m^{-2}]	394
Ua_0	[V]	0
Jc_{ref}	[A m^{-2}]	5.69 E -6
Uc_0	[V]	2.96
K_d	[m s^{-1}]	1 E -5
K_H	[mol m^{-3}]	30.0
C_{Li}	[mol m^{-3}]	1000
C_{A-}	[mol m^{-3}]	1000
C_{O2}	[mol m^{-3}]	30.0
D_{Li}	[m^2 s^{-1}]	2.11 E -9
D_{A-}	[m^2 s^{-1}]	4 E -10
D_{O2}	[m^2 s^{-1}]	7 E -10
Z_{Li}		1
Z_{A-}		-1
Z_{O2}		0
V_{Li2O2}	[m^3 mol^{-1}]	2.1495 E -5

The variable T is the operational temperature of the cell, Ja_{ref} is the anode reference applied current density, Ua_0 is the open circuit potential of the anode, Jc_{ref} is the cathode reference applied current density, Uc_0 is the open circuit potential of the cathode, k_d is the

oxygen diffusion kinetics, K_H is Henry's constant, C_{Li} is the concentration of lithium metal, C_{A^-} is the concentration of anion salt, C_{O2} is the concentration of oxygen, D_{Li} is the diffusivity of lithium, D_{A^-} is the diffusivity of anion salt, D_{O2} is the diffusivity of oxygen, Z_{Li} is the charge of lithium, Z_{A^-} is the charge of anion salt, Z_{O2} is the charge of oxygen, and V_{Li2O2} is the molar concentration of Li_2O_2.

3.10   Discharge calculation verification

Transport property as a function of precipitate deposition preference coefficient through interfacial current density is implemented into the model. A verification model is implemented with the same microstructure property used in Griffith et al's experiment. Figure 23 overlay simulation discharge behavior to experimental discharge behavior found in figure 2.
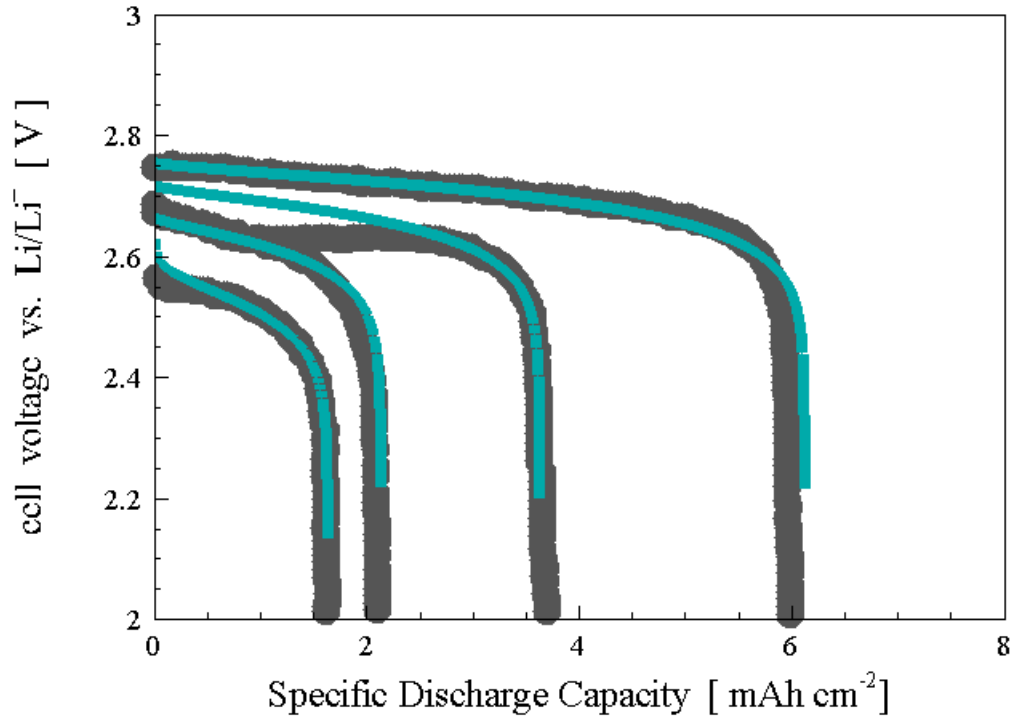
Figure 23. Comparison between simulation discharge behavior and experimental discharge behavior. Simulated data is in blue, and experimental data is in grey.

The simulation data is well fitted on the curve, except for the fit between simulation and experimental discharge capacity with an apply current density of 2 A m^{-2}. This is suffice to say the simulation is well within acceptable accuracy for stochastic study of microstructure effect on lithium-air battery discharge behavior.

4   RESULTS AND DISCUSSION

The discharge calculation verification permit a stochastic study of microstructure effect on lithium air battery discharge capacity. Early effort on non-dimensionalizing microstructure and correlating current density to precipitate deposition preference coefficient reduced the stochastic study to porosity, fiber diameter, and current density.

The fiber diameter of the electrode used in Griffith et al's experiment can be found by dividing the interfacial area by non-dimensionalized interfacial area. The strand diameter was discovered to be 22.9 nm. The value allow us to narrow a range of fiber diameter that critical to understand microstructure effect on discharge capacity. In order to cover a wide range of fiber diameter, a logarithmic scale of fiber diameter from 0.01 μm to 10 μm is implemented. Porosity is generally controlled between 60% and 90% for most fiber structure. Current densities used for the study are 1 A m^{-2}, 2 A m^{-2}, 5 A m^{-2}, and 10 A m^{-2} for uniformity, and comparability to existing research.

## 4.1 Fiber diameter effect on discharge capacity of lithium air cell

A stochastic study is conducted on fiber diameter's effect on discharge capacity. A baseline case is conducted at 80% porosity, cathode thickness of 250 μm, and current density of 1 A m^{-2}. The discharge capacity of the study is shown in figure 24.
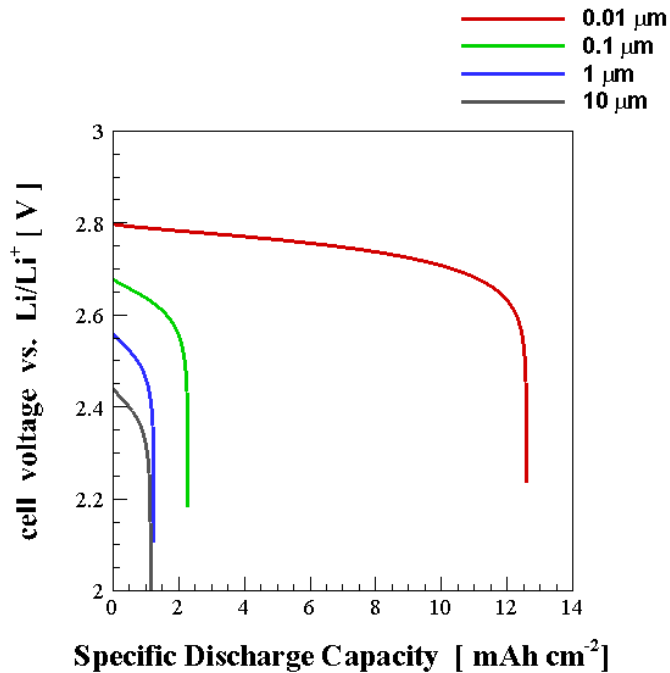
Figure 24. Baseline study of strand diameter's effect on specific discharge capacity

It can be observed that decreasing stand diameter improves specific discharge capacity of lithium-air cell. This is only possible primarily due to the increasing in interfacial area between porous void and active material. Another trend observed is the similarity in specific discharge capacity for fiber diameter of 1 μm and 10 μm. The drastic drop in specific discharge capacity is most likely due to surface passivation. Active area change across the cathode structure with increasing specific discharge capacity can be seen in figure 25.
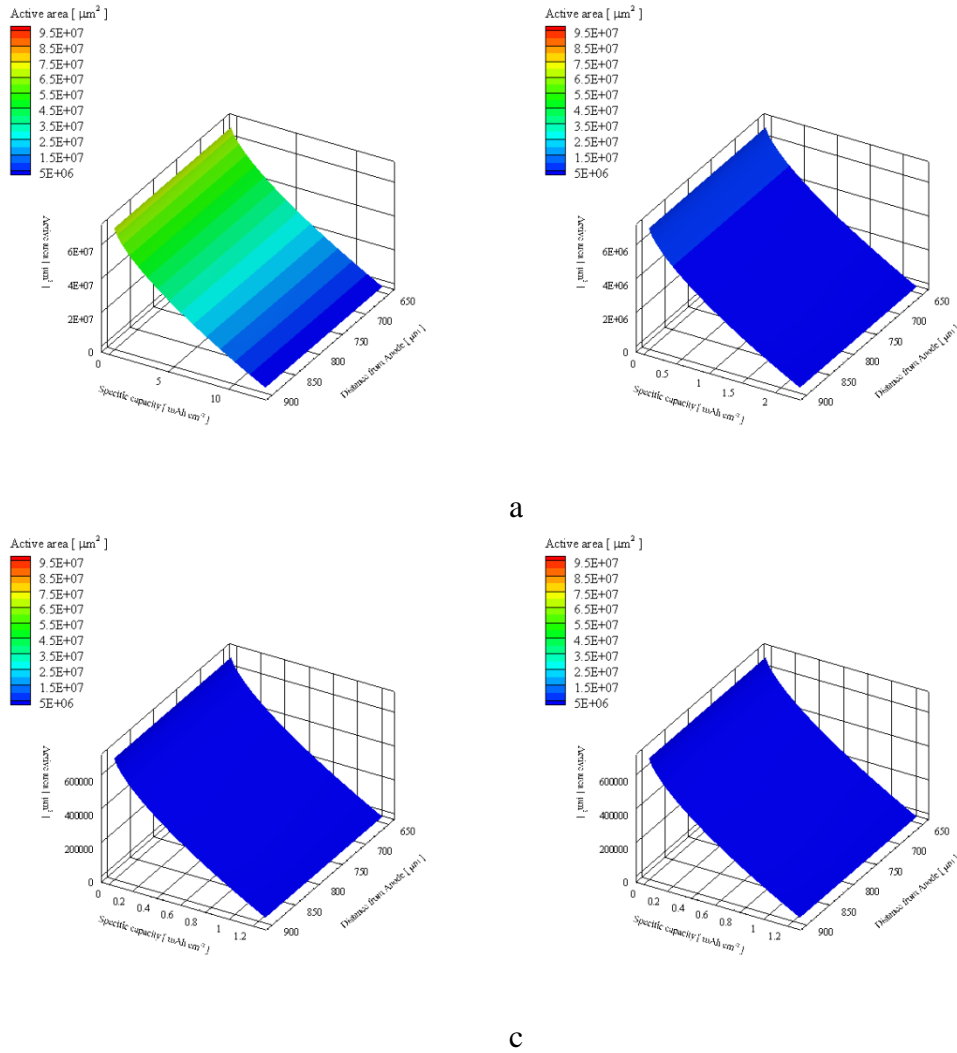
Figure 25. Interfacial area of microstructure with fiber diameter of (a) 0.01 μm (b) 0.1 μm (c) 1 μm and (d) 10 μm.

Active area of microstructure with fiber diameter of 0.01 μm shows a high initial interfacial area of 6.0 x 10^7 μm^2. The high initial interfacial area drastically increased specific discharge capacity. The initial interfacial area for fiber diameter of 1 μm and 10

μm is a little higher than 600,000 μm^2. The low initial interfacial area will definitely cause interfacial area passivation, which explains the low specific discharge capacity.

Some may argue the increase in strand diameter may cause porous void blockage as precipitate deposition occurs. Pore blockages, figure 26, is not observed in the cathode with fiber diameter of 1 μm and 10 μm.
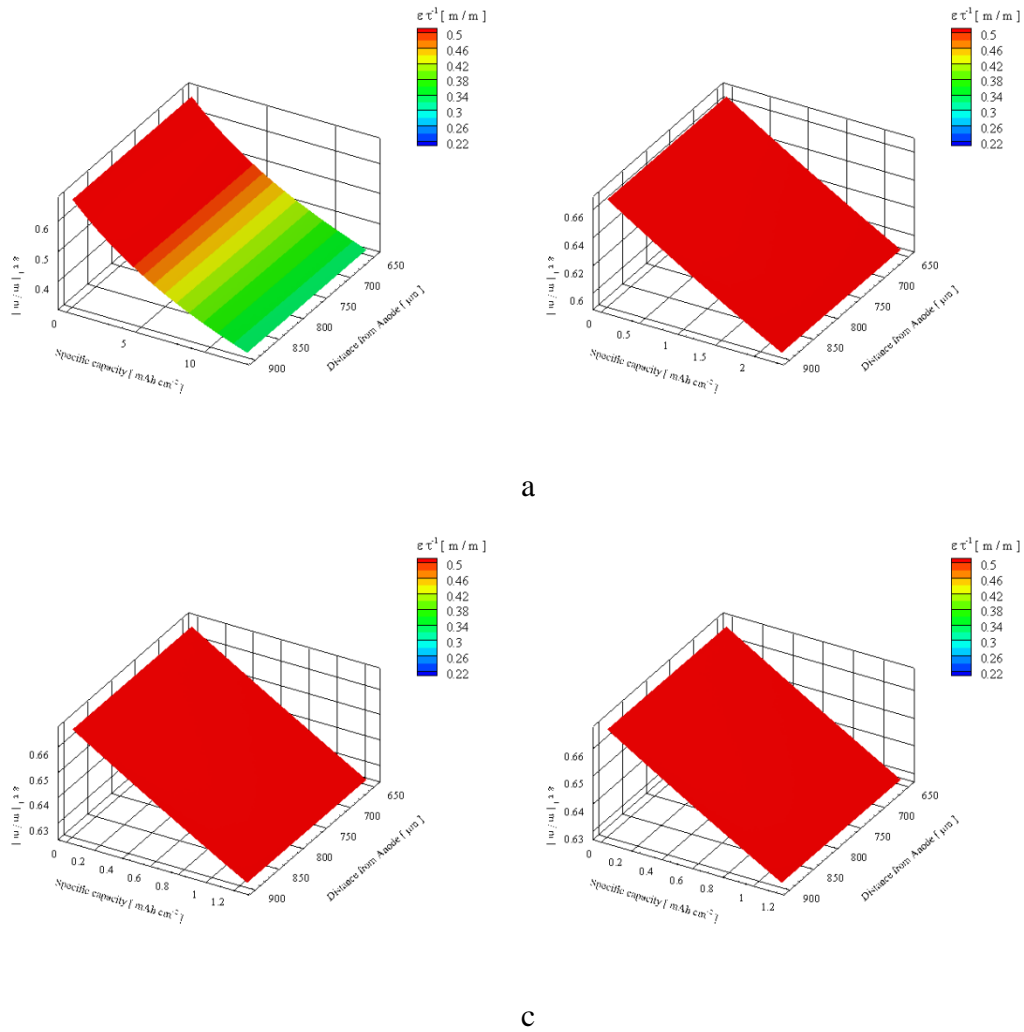
Figure 26. Effective transport coefficient of microstructure with fiber diameter of (a) 0.01 μm (b) 0.1 μm (c) 1 μm and (d) 10 μm.

Porosity value exist between 0 and 1 since a structure can only be completely porous or complete solid, whereas tortuosity is not bounded between values; thus high effective transport coefficient signify a low tortuosity value and low effective transport

coefficient value signify a high tortuosity value. It can be observed that effective transport coefficient for microstructures with fiber diameter of 0.1 μm, 1 μm, and 10 μm remained above 0.6. Effective transport coefficient did decrease for microstructure with fiber diameter of 0.01 μm, which most likely occur due to massive increase in surface area for precipitate to grow. The high effective transport coefficient values for microstructures with fiber diameter of 0.1 μm, 1 μm, and 10 μm eliminated any doubt regarding porous void blockage.

Oxygen kinetics is another argument that can be made against low specific discharge capacity. Since lithium-air battery's electrochemical reaction rely on supply of active material (oxygen), discrepancy between oxygen flux and kinetics will cause early termination. Termination due to decreasing oxygen flux prior to interfacial area passivation is called oxygen starvation. Oxygen starvation, figure 27, is not observed for cathode with fiber diameter of 0.01 μm, 0.1 μm, 1 μm, and 10 μm.

a   b

c   d
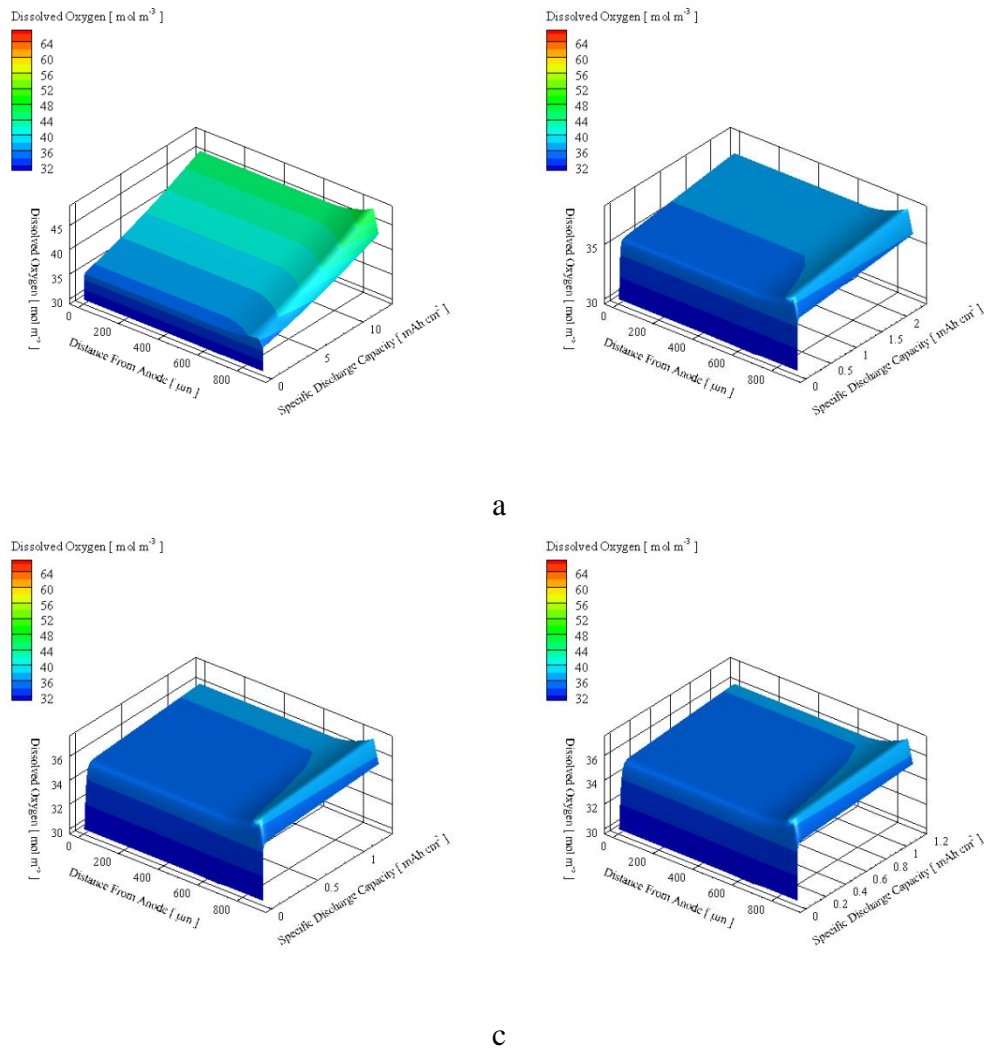
Figure 27. Dissolved oxygen within cathode of microstructure with fiber diameter of (a) 0.01 μm (b) 0.1 μm (c) 1 μm and (d) 10 μm.

It can be observed the concentration of dissolved oxygen within the cathode structure is well above initial concentration of 30 mol m^{-3}, which eliminate the possibility of oxygen starvation.

**4.2 Porosity effect on discharge capacity of lithium air cell**

A stochastic study is conducted on porosity's effect on discharge capacity. A baseline case is conducted at strand diameter of 1 μm, cathode thickness of 250 μm, and current density of 1 A m^{-2}. The specific discharge capacity of the study is shown in figure 28.
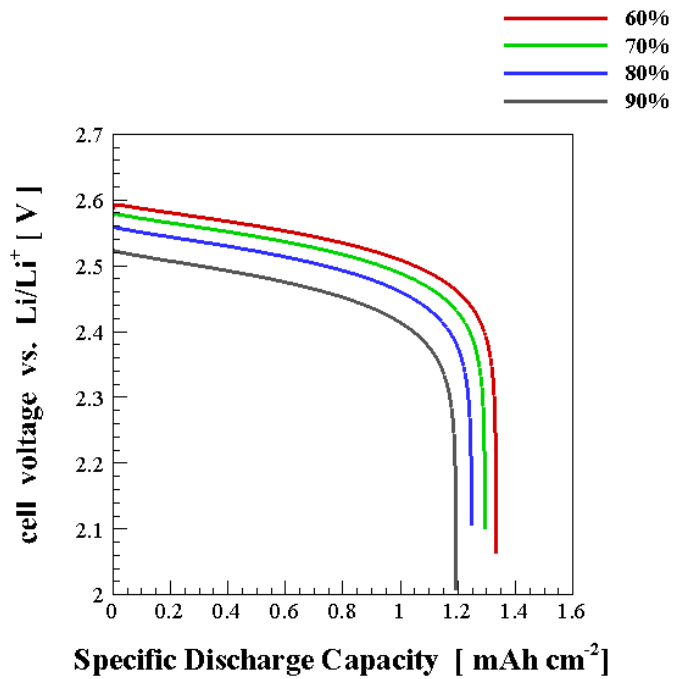
Figure 28. Baseline study of porosity's effect on specific discharge capacity

It can be observed that specific discharge capacity decreases with increasing initial porosity. The decrease in specific discharge capacity is relatively small when compared with the effect fiber diameter has on specific discharge capacity. Figure 29 examine the change in interfacial area with increasing initial porosity and specific discharge capacity.
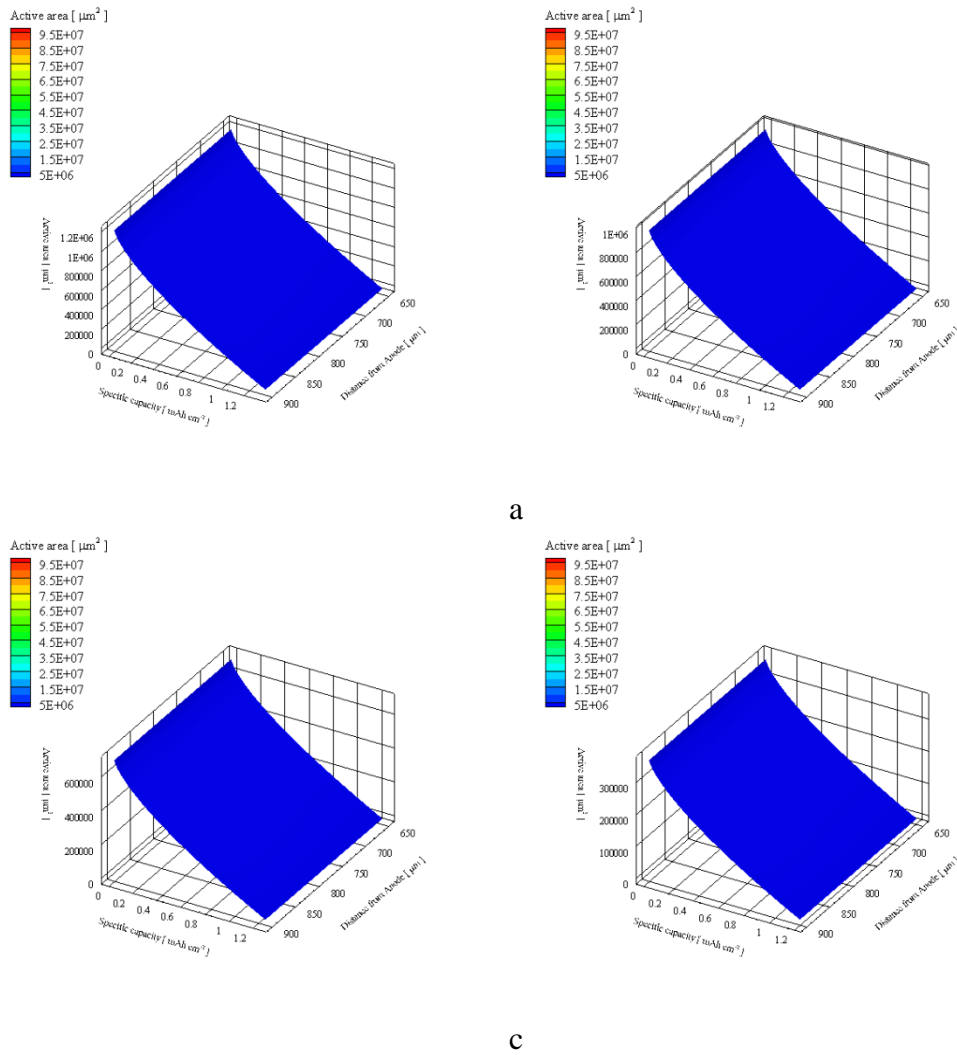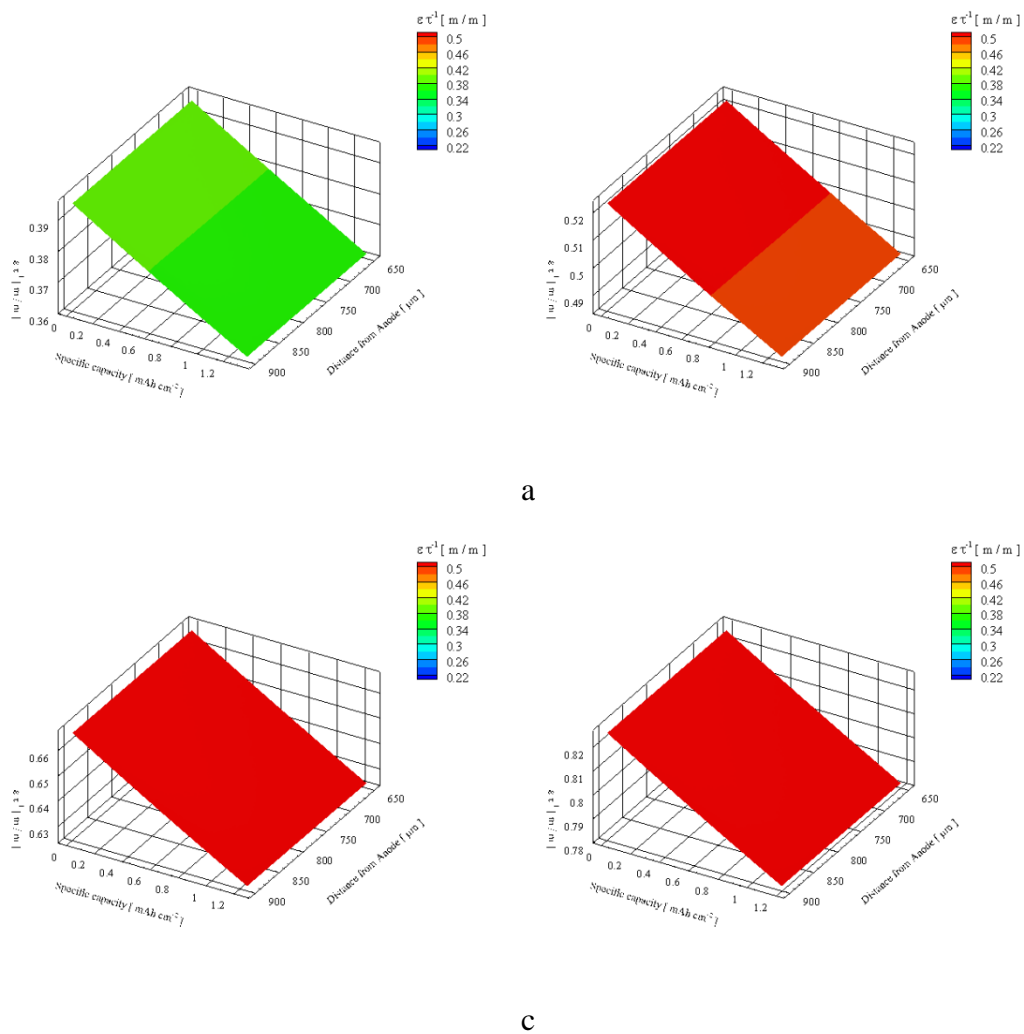
Figure 29. Interfacial area of microstructure with initial porosity of (a) 60% (b) 70% (c) 80% and (d) 90%.

The small decrease in specific discharge capacity is primarily due to the low initial interfacial area for the four microstructure, which started with interfacial areas between 300000 μm^{-2} and 1.2 x 10^6 μm^{-2}. Increase in porosity would alleviate porous void

blockage, thus it is unlikely to be a contributing cause for decrease in specific discharge capacity. Figure 30 examine if initial porosity causes major change to effective transport coefficient of the microstructure.

a   b

c   d

Figure 30. Effectivity transport coefficient of microstructure with initial porosity of (a) 60% (b) 70% (c) 80% and (d) 90%.

It can be observed initial porosity changes the effective transport coefficient of microstructure. Microstructures with initial porosity of 70%, 80%, and 90% have higher effective transport coefficient which correspond to low tortuosity. Although effective transport coefficient of microstructure with initial porosity of 60% is comparatively low, specific discharge capacity termination cannot be attributed to pore blockage. Since the specific discharge capacity is higher than the other three microstructure, it is only logical that interfacial area passivation took place prior to pore blockage.

Oxygen starvation is unlikely since the kinetic of the electro-chemical reaction did not change. As predicted, figure 31, oxygen starvation is not observed for microstructures with initial porosity of 60%, 70%, 80%, and 90%.

a   b

c   d
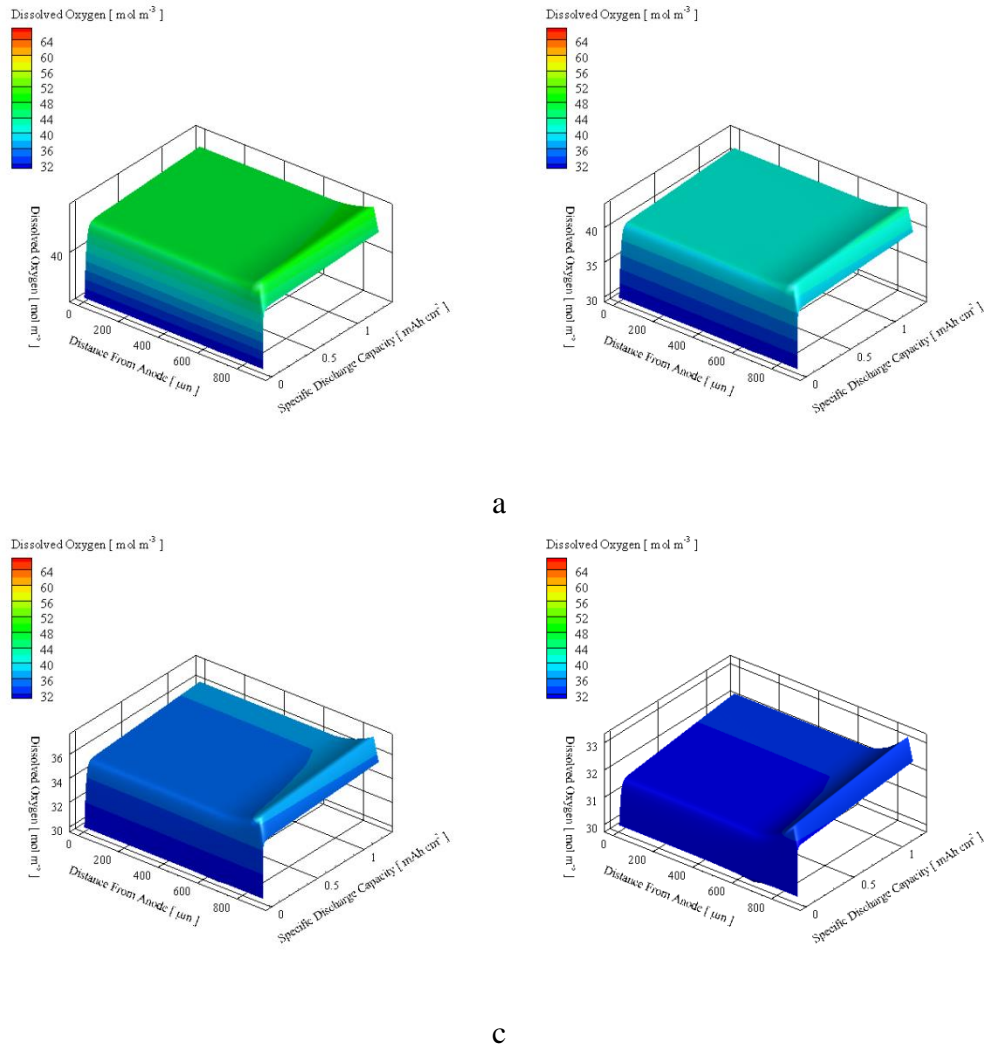
Figure 31. Dissolved oxygen within cathode of microstructure with initial porosity of (a) 60% (b) 70% (c) 80% and (d) 90%.

It can be observed that oxygen concentration dissolved within the cathode steadily increases across the four microstructure. The concentration, however, decreases with

increasing porosity. The value is able to consistently stay above the initial oxygen concentration which suggest a sustainable electro-chemical reaction.
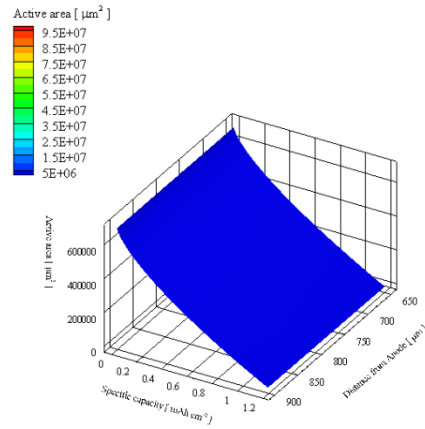
4.3 Apply current density effect on discharge capacity of lithium air cell

Apply current density effect on discharge capacity is drastically different compared to microstructure change. Change in current density affect morphology of the precipitate and kinetics of the reaction. A stochastic study is conducted on current density's effect on discharge capacity. A baseline case is conducted at strand diameter of 1 μm, cathode thickness of 250 μm, and initial porosity of 80%. The specific discharge capacity of the study is shown in figure 32.
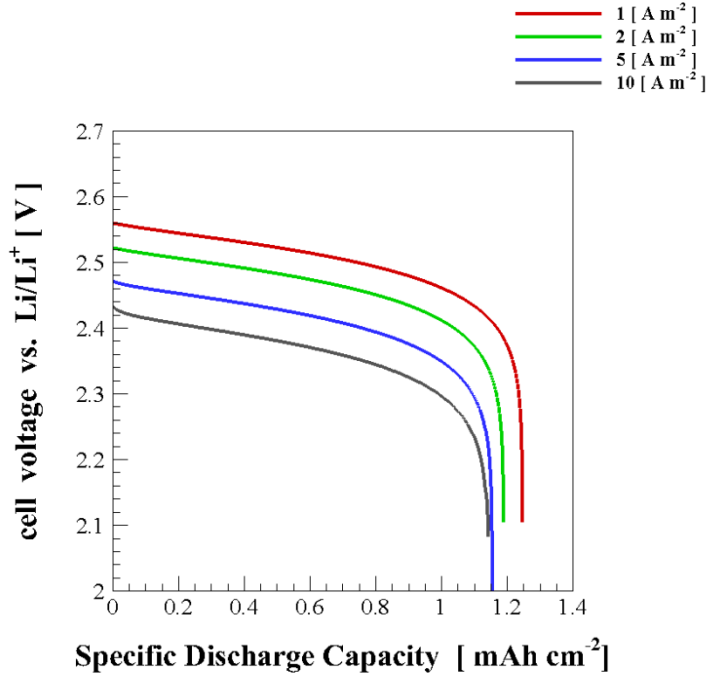
Figure 32. Baseline study of current density's effect on specific discharge capacity

It can be observed that increase of current density decrease discharge capacity, and in the case of 5 A m^{-2}, and 10 A m^{-2}, both scenario achieve the same discharge capacity. Since current density changes deposition preference, active species consumption, and tortuosity of a microstructure, all phenomenon must be investigated prior to a general conclusion on mode of termination. Figure 33 investigates the active area change under the four different apply current density.
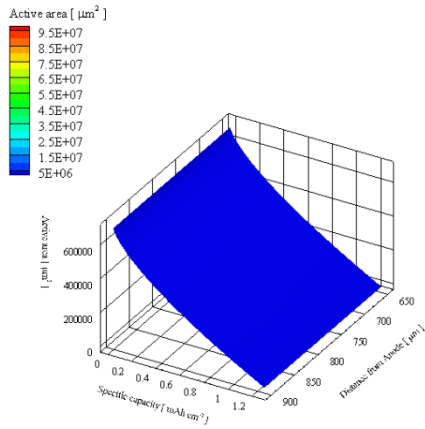
a   b
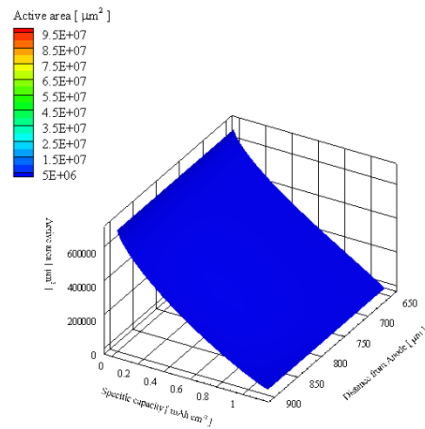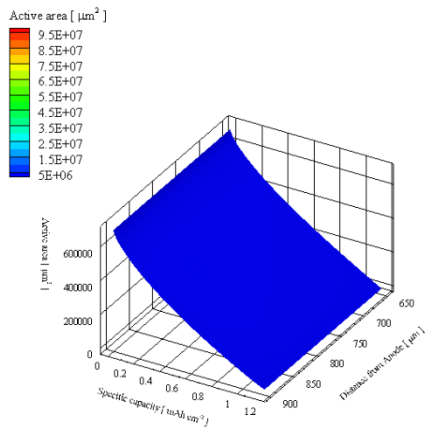
c   d

Figure 33. Interfacial area of microstructure with apply current density of (a) 1 A m^{-2} (b) 2 A m^{-2} (c) 5 A m^{-2} and (a) 10 A m^{-2}.

Since the microstructures used for the three cases are the same, decrease in discharge capacity cannot be the loss of interfacial area prior to discharge. The only noticeable difference is an early termination of interfacial area with apply current density

of 10 A m^{-2}. The complete utilization of interfacial area passivation and early termination is a good indication of early interfacial area passivation. Next mode of lithium-air battery discharge termination is porous void blockage resulting from drastic increase in tortuosity. Figure 34 investigate change in effective transport coefficient of the microstructure under four sets of apply current density.
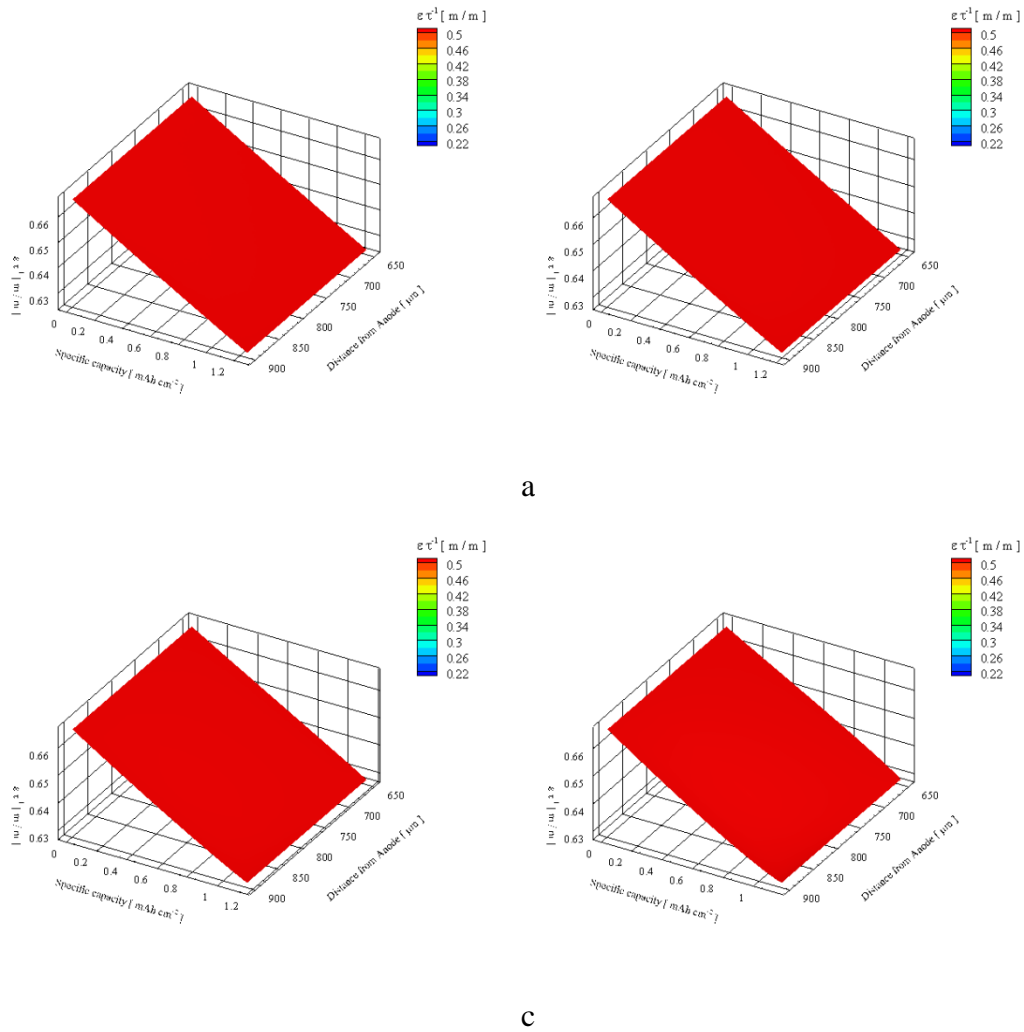
Figure 34. Effectivity transport coefficient of microstructure with apply current density of (a) 1 A m^{-2} (b) 2 A m^{-2} (c) 5 A m^{-2} and (a) 10 A m^{-2}.

It can be observed that effectivity transport coefficient of microstructure remain high, which correspond to a low tortuosity value. Low value of tortuosity suggest interfacial area passivation maybe the cause of decreasing specific discharge capacity.

Since current density increases the kinetic of the reaction, oxygen starvation is more likely to occur, thus a study on dissolved oxygen within cathode structure is warranted. Figure 35 investigate the amount of oxygen dissolved in the cathode with increasing apply current density.
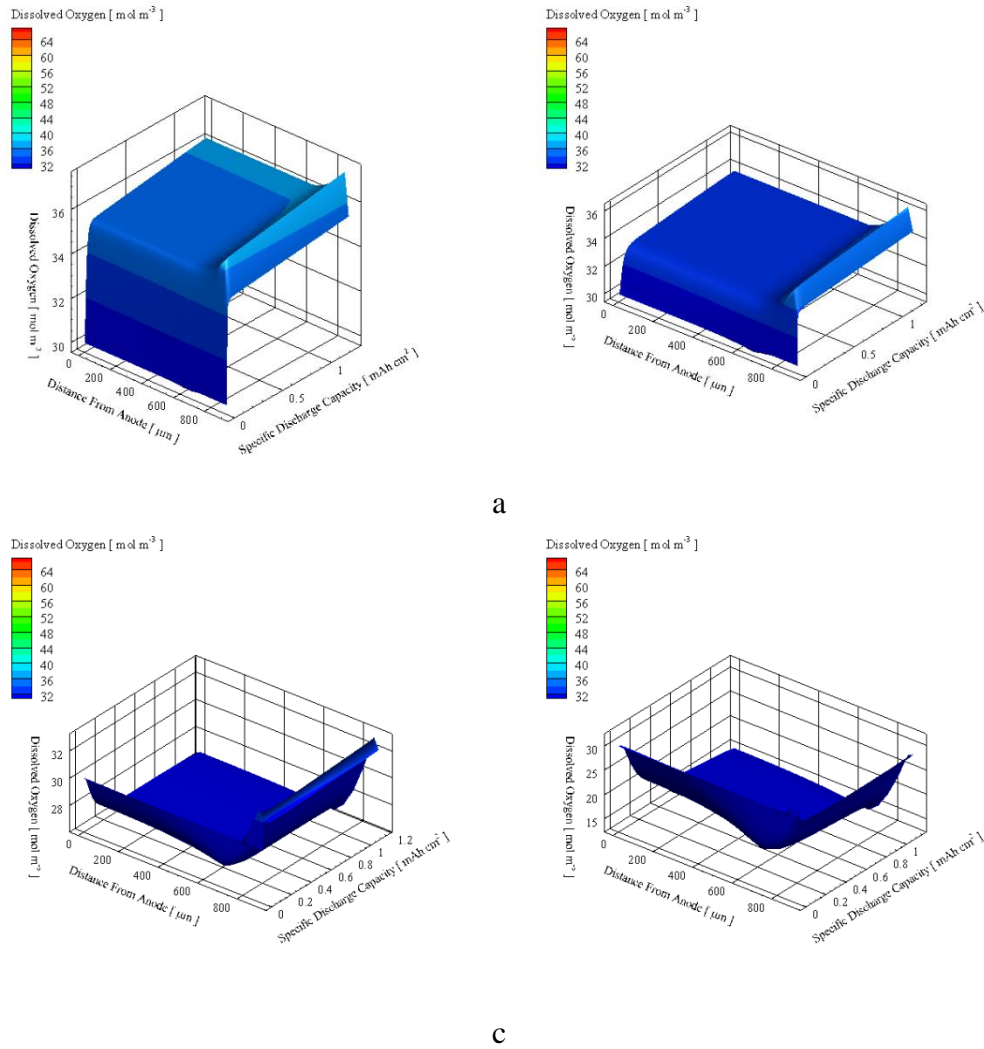
Figure 35. Dissolved oxygen within cathode of microstructure with apply current density of (a) 1 A m^{-2} (b) 2 A m^{-2} (c) 5 A m^{-2} and (a) 10 A m^{-2}.

The increase of current density has a drastic effect on oxygen dissolved in the cathode. At apply current density of 1 A m^{-2} and 2 A m^{-2}, dissolved oxygen maintain above 30 mol m^{-3} throughout the microstructure. At apply current density of 5 A m^{-2} and 10 A

m^{-2}, however, oxygen concentration in the cathode drops below 30 mol m^{-3} with increasing specific discharge capacity. The increase in apply current density increased the rate which lithium ion combined with oxygen. If the diffusion of lithium-ion reaches a point when oxygen diffusion at the cathode-current-interface cannot sustain the electrochemical reaction, it will begin to react with initial oxygen concentration present in the cathode. The increasing difficulty to sustain the kinetics of the electrochemical reaction causes voltage drop.

4.4 Current density's effect on idealized microstructure

At this point, general guideline to the design of a lithium-air battery cathode with significant increase in discharge capacity can be determined. The fiber electrode should be constructed with a low porosity to increase initial interfacial area. The fiber diameter should be constructed at 0.01 μm scale. Increase to fiber diameter by one magnitude of order can potentially decrease specific discharge capacity by one magnitude of order. A general study was composed to study current density effect on microstructure with fiber diameter of 0.01 μm and porosity of 70%. The specific discharge capacity of the study is shown in figure 36.
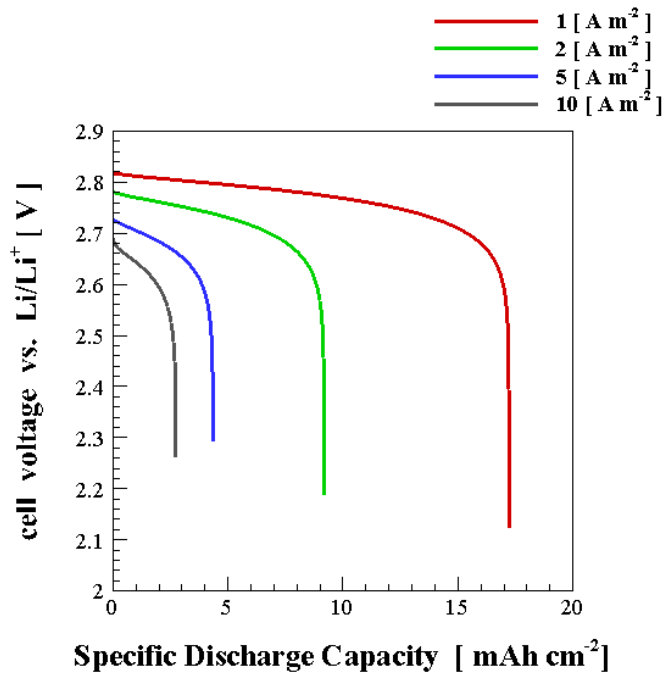
Figure 36. Study of current density's effect on specific discharge capacity

At apply current density of 1 A m^{-2}, the simulation yield a specific discharge capacity of 17 mAh cm^{-2}. The high specific discharge capacity is primarily due to increase of interfacial area for precipitate deposition. The increase of apply current density yield a more distinctive result compared with the baseline study of current density with strand diameter of 1 μm. The significant increase in active surface area will yield a more distinctive result to the root cause of specific discharge capacity fade by current density. Figure 37 investigate the interfacial area change when different apply current density is imposed to the simulation model.

134
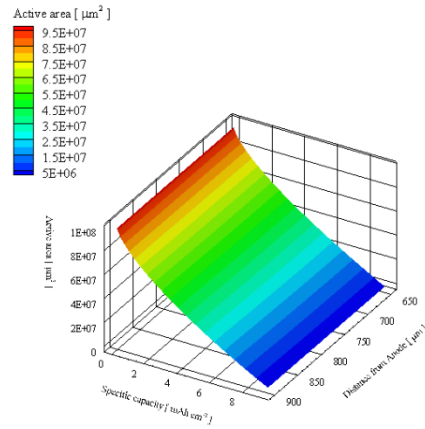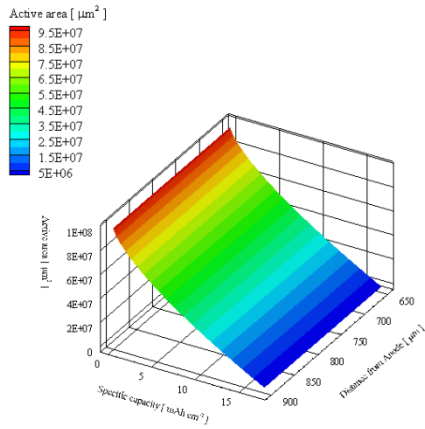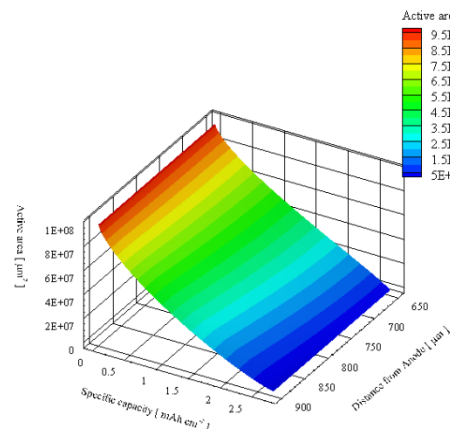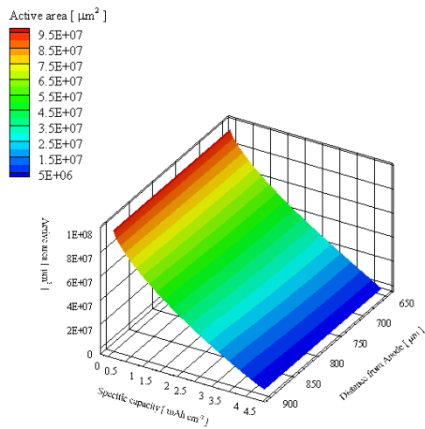
Figure 37. Interfacial area of microstructure with apply current density of (a) 1 A m^{-2} (b) 2 A m^{-2} (c) 5 A m^{-2} and (a) 10 A m^{-2}.

It can be observed that early interfacial area passivation occurred for apply current density of 10 A m^{-2}. The complete utilization of available active area at a small specific capacity suggest the rate of passivation is significantly higher when compared with

different boundary. Complete utilization of interfacial area suggest porous void blockage may not be the primary cause of capacity fade. Figure 38 investigate the change in effective transport coefficient of the cathode.

a

b

c

d
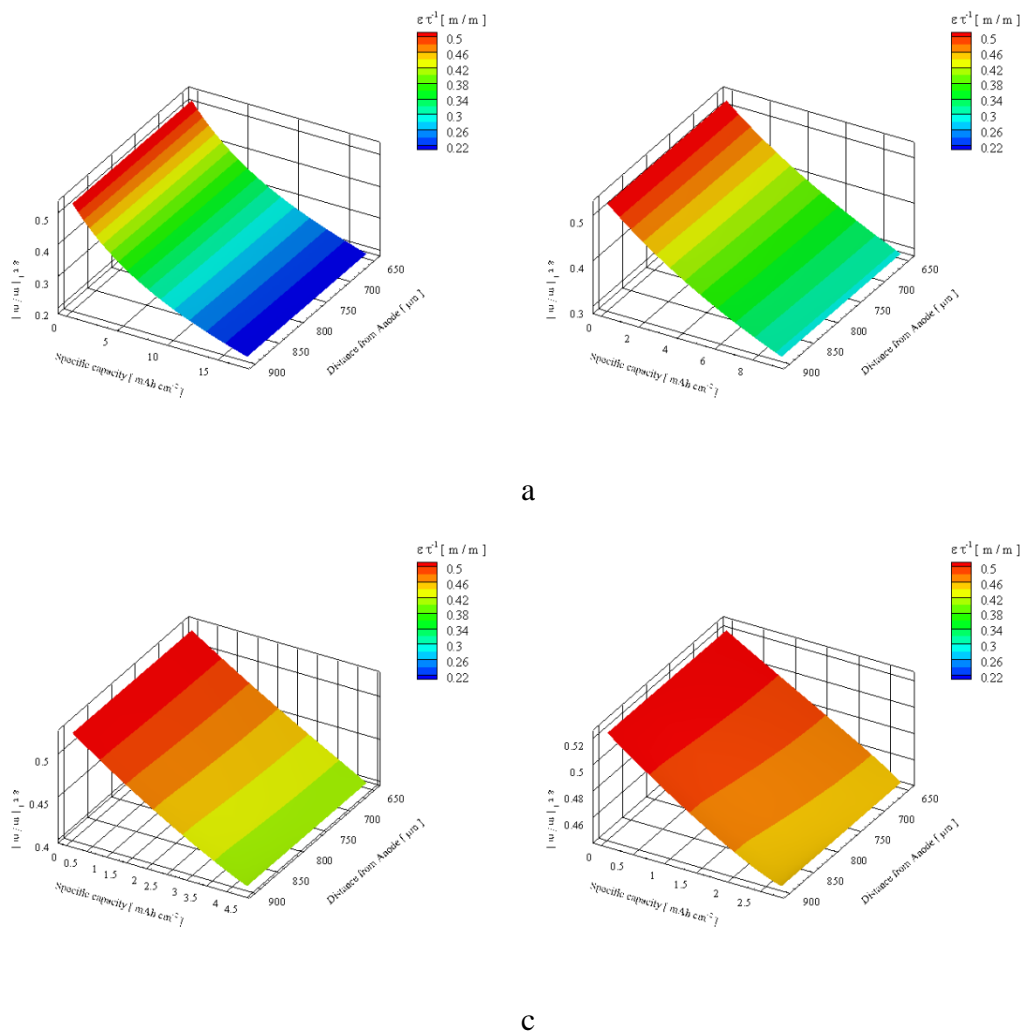
Figure 38. Effectivity transport coefficient of microstructure with apply current density of (a) 1 A m^{-2} (b) 2 A m^{-2} (c) 5 A m^{-2} and (a) 10 A m^{-2}.

It can be observed that the effective transport coefficient of cathode structure with apply current density 1 A m^{-2} decreases more drastically then 2 A m^{-2}, 5 A m^{-2}, and 10 A m^{-2}, which correspond to an increase of tortuosity. The increase of tortuosity is primarily due to high precipitate deposition preference coefficient. The increase likeliness of precipitate's preference to deposit on its own species decreases the overall porosity of the microstructure, and increases tortuosity of the microstructure. At high current density, low precipitate deposition preference coefficient causes precipitate to deposit on active material, which lower the tortuosity of the microstructure prior to interfacial area passivation. The low tortuosity yield a higher effective transport coefficient. The increase in current density increases the kinetic of the reaction; a study on dissolved oxygen within cathode structure is warranted. Figure 39 investigate the amount of oxygen dissolved in the cathode with increasing apply current density.

a   b

c   d
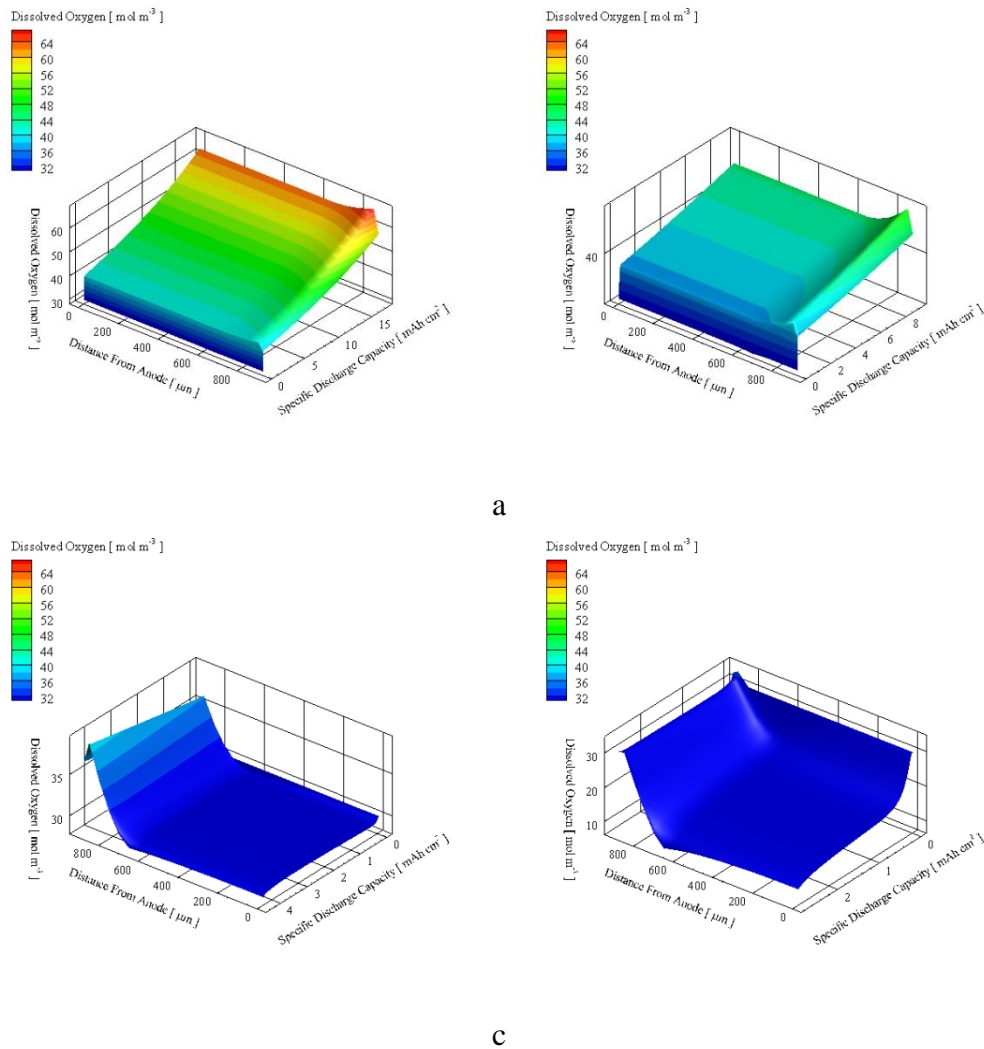
Figure 39. Dissolved oxygen within cathode of microstructure with apply current density of (a) 1 A m^{-2} (b) 2 A m^{-2} (c) 5 A m^{-2} and (a) 10 A m^{-2}.

Similar to the current density baseline result dissolved oxygen decreases with increasing current density. One observable difference is the increase in dissolved oxygen within the cathode as fiber diameter decreases. The increase of oxygen dissolved is most

likely due to the increase of precipitate that stemmed from the increase of interfacial area. The cause for capacity fade with changing current density can be concluded as a combination of interfacial area passivation and oxygen starvation.

5 CONCLUSIONS & FUTURE WORK

It is suffice to say a new method is incepted to model lithium-air battery discharge performance. The combined use of commercial software and internally developed computation code allowed precise control on deposition behavior. Fiber microstructure physics can be controlled on every level with changes to fiber diameter, fiber length, voxel size, domain volume, and initial porosity of the domain. Deposition physics can be controlled with changes to precipitate sizes, and the number of precipitate that can be deposited on in each iteration. The microstructures generated through the internally developed computation code allow microstructure information to be tabulated in a pseudo-time scale.

Calculation of microstructure transport property with each iterative deposition creates a pseudo-time dependent transport property. This is particularly powerful as past modeling technique revolves around fix transport property. The use of fix transport property in discharge performance calculation is flawed since porosity and tortuosity changes with increasing deposition. The combination of data with pseudo-time based transport property and microstructure physics property yields a detail description of deposition physics.

Physics based mathematical correlation of transport property can be extracted with the extensive microstructure data set. Interfacial area and tortuosity can be correlated to precipitation addition, initial porosity, and precipitate deposition preference coefficient.

The combination of the three independent variables incorporate microstructure physics, precipitation deposition physics, and a time scale to describe transport property. Data extracted from Griffith et al's work correlate current density to precipitate deposition preference coefficient. Connection of current density and deposition physics helps quantify an observable phenomenon.

The simulation data accurately replicated the data Griffith et al's publish. The result is rather profound as it confirms the legitimacy of the pseudo-time technique. The model can be utilized to predict lithium-air battery performance, and to optimize lithium-air battery microstructure design.

The results from the current research yield multiple possibility for future work. The precipitate deposition mechanism can be used to include precipitate from side reaction such as Li_2CO_3. Aside from deposition mechanism, the data from increasing initial porosity can be utilized in the electrochemical performance simulation to imitate mechanical degradation of carbon electrode. As carbon material degrades with repeating discharge, initial porosity will slowly increases. Finally, charging of the lithium-air cell and cycling of lithium-air cell can be simulated by alternating the direction of current density applied to the electrochemical simulation model.

REFERENCES

1.   Laboratory, L.L.N., *Estimated US energy consumption in 2015: 97.5 quads*, 2015_United-States_energy, Editor. 2015.

2.   Elton J. Cairns, P.A., *Batteries for electric and hybrid-electric vehicles.* Annual Review of Chemical and Biomolecular Engineering, 2010. **1**: p. 299-320.

3.   Rotem Marom, S.F.A., Nicole Leifer, David Jacob, Doron Aurbach, *A Review of advanced and practical lithium battery materials.* Journal of Material Chemistry, 2011. **21**: p. 9938-9954.

4.   Jun Lu, K.C.L., Yang-Kook Sun, Larry A Curtiss, Khalil Aminea, *Review—understanding and mitigating some of the key factors that limit non-aqueous lithium-air battery performance.* Journal of Electrochemical Society, 2015. **162**(14): p. A2439-A2446.

5.   G. Girishkumar, B.M., A. C. Luntz, S. Swanson, W. Wilcke, *Lithium-air battery: promise and challenges.* The Journal of Physical Chemistry Letters, 2010. **1**: p. 2193-2203.

6.   George Crabtree, M.L., Leon Glicksman, Michael Lubell, David Goldstein, Burton Richter, David Goldston, Maxine Savitz, David Greene, Daniel Sperling, Dan Kammen, *How America can look within to achieve energy security and reduce global warming.* Reviews of Modern Physics, 2008. **80**(4): p. S1-S109.

7.   Naveed Akhtar, W.A., *Prospect, challenges, and latest developments in lithium-air batteries.* International Jorunal of Energy Research, 2014. **39**: p. 303-316.

8.   K.M. Abraham, Z.J., *A polymer electrolyte-based rechargable lithium/oxygen battery.* Journal of Electrochemical Society, 1996. **143**(1): p. 1-5.

9.   Martin Winter, R.J.B., *What are batteries, fuel cells, and supercapacitors?* Chemical Reviews, 2004. **104**(10): p. 4245-4269.

10.   H. H. Eysel, S.T., *Raman spectra peroxides.* Zeitschrift für anorganische und allgemeine Chemie, 1975. **411**(2).

11.   Christopher D. Rahn, C.-Y.W., *Battery system engineering*. 2013: A John Wiley & Sons, Ltd, Publication.

12.   Nobuyuki Imanishi, O.Y., *Rechargable lithium-air batteries: characteristics and prospects.* Materials Today, 2014. **17**(1): p. 24-30.

13.   Moran Balaish, A.K., Yair Ein-Eli, *A critical review on lithium-air battery electrolytes.* Physical Chemistry Chemical Physics, 2014. **16**: p. 2801-2822.

14.   Muhammed M. Ottakam Thotiyl, S.A.F., Zhangquan Peng, and Peter G. Bruce*, *The Carbon Electrode in Nonaqueous Li−O2 Cells.* Journal of American Chemical Society 2013. **135**: p. 494-500.

15.   B. D. McCloskey, A.S., R. Scheffler, D. C. Miller, V. Viswanathan, J. S. Hummelshøj, J. K. Nørskov, A. C. Luntz, *Twin problems of interfacial carbonate formation in nonaqueous Li−O2 Batteries.* The Journal of Physical Chemistry Letters, 2012. **3**: p. 997-1001.

16.   Betar M. Gallant, R.R.M., David G. Kwabi, Jigang Zhou, Lucia Zuin, Carl V. Thompson, Yang Shao-Horn, *Chemical and morphological changes of Li-O2*

battery electrodes upon cycling. Journal of Physical Chemistry C, 2012. **116**: p. 20800-20805.

17.   Stefan A. Freunberger, Y.C., Nicholas E. Drewett, Laurence J. Hardwick, Fanny Barde, Peter G. Bruce, *The lithium-oxygen battery with ether-based electrolytes.* Angewandte Chemie International Edition, 2011. **50**: p. 8609-8613.

18.   Wu Xu, J.H., Mark H. Engelhard, Silas A. Towne, John S. Hardy, Jie Xiao, Ju Feng, Mary Y. Hu, Jian Zhang, Fei Ding, Mark E. Gross, Ji-Guang Zhang, *The stability of organic solvents and carbon electrode in nonaqueous Li-O2 batteries.* Journal of Power Sources, 2012. **215**: p. 240-247.

19.   Arumugam Manthiram, L.L., *Hybrid and aqueous lithium-air batteries.* Advance Energy Material, 2015. **5**(1401302): p. 1-17.

20.   Pascal Hartmann, T.L., Martin R. Busche, Meike Schneider, Marisa Reich, Joachim Sann, Philipp Adelhelm, Jürgen Janek, *Degradation of NASICON-type materials in contact with lithium metal: formation of mixed conducting interphases (MCI) on solid electrolytes.* The Journal of Physical Chemistry C, 2013. **117**: p. 21064-21074.

21.   H. Wang, N.I., A. Hirano, Y. Takeda, O. Yamamoto, *Electrochemical properties of the polyethylene oxideeLi(CF3SO2)2N and ionic liquid composite electrolyte.* Journal of Power Sources, 2012. **219**: p. 22-28.

22.   S. Liu, N.I., T. Zhang, A. Hirano, Y. Takeda, O. Yamamoto, J. Yangb, *Lithium dendrite formation in Li/poly(ethylene oxide)–lithium bis(trifluoromethanesulfonyl)imide and N-methyl-N-propylpiperidinium*

bis(trifluoromethanesulfonyl)imide/Li cells. Journal of Electrochemical Society, 2010. **157**(10): p. A1092-A1098.

23. C. Brissot, M.R., J.N. Chazalviel, S. Lascaud, *Dendritic growth mechanisms in lithium/polymer cells.* Journal of Power Sources, 1999. **81-82**: p. 925-929.

24. Xiang-Wu Zhang, Y.L., Saad A. Khan, Peter S. Fedkiw, *Inhibition of lithium dendrites by fumed silica-based composite electrolytes.* Journal of Electrochemical Society, 2004. **151**(8): p. A1257-A1263.

25. Fu, J., *Super conductivity of glass-ceramics in the system Li2O-Al2O3-TiO2-P2O5.* Solid State Ionics, 1997. **96**: p. 195-200.

26. Fu, J., *Fast Li+ ion conduction in Li2O-(Al2O3 Ga2O3)-TiO2-P2O5 glass-ceramics.* Journal of Material Science, 1998. **33**: p. 1549-1553.

27. Hiromichi Aono, E.S., Yoshihiko Sadaoka, Nobuhito Imanaka, Gin-ya Adachi, *Ionic conductivity of solid electrolytes based on lithium titanium phosphate.* Journal of Electrochemical Society, 1990. **137**(4): p. 1023-1027.

28. Hiromichi Aono, E.S., Yoshihiko Sadaoka, Nobuhito Imanaka, Gin-ya Adachi, *Ionic conductivity of the lithium titanium phosphate (Li1+xMxTi2-x(PO4)3, M = Al, Sc, Y, and La) systems.* Journal of Electrochemical Society, 1989. **136**(2): p. 590-591.

29. K. Arbi, M.A.-T., J. Sanz, *Li mobility in triclinic and rhombohedral phases of the Nasicon-type compound LiZr2(PO4)3 as deduced from NMR spectroscopy.* Journal of Material Chemistry, 2002. **12**: p. 2985-2990.

30. J. Kuwano, N.S., M. Kato, K. Takano, *Ionic conductivity of LiM2(PO4)3 (M = Ti, Zr, Hf) and related compositions.* Journal of Solid State Ionics, 1994. **70/71**: p. 332-336.

31. Katsuhiro Nomura, H.K., *Transport properties of Ba(Zr0.8Y0.2)O3 − δ perovskite.* Solid State Ionics, 2007. **178**: p. 661-665.

32. Ramaswamy Murugan, V.T., Werner Weppner, *Fast lithium ion conduction in garnet-type Li7La3Zr2O12.* Angewandte Chemie International Edition, 2007. **46**: p. 7778-7781.

33. V. Thangadurai, W.W., *Investigations on electrical conductivity and chemical compatibility between fast lithium ion conducting garnet-like Li6BaLa2Ta2O12 and lithium battery cathodes.* Journal of Power Sources, 2005. **142**: p. 339-344.

34. Satoshi Hasegawa, N.I., Tao Zhang, Jian Xie, Atsushi Hirano, Yasuo Takeda, Osamu Yamamoto, *Study on lithium/air secondary batteries—stability of NASICON-type lithium ion conducting glass–ceramics withwater.* Journal of Power Sources, 2009. **189**: p. 371-377.

35. Yunfeng Li, K.H., Yangchuan Xing, *A hybrid Li-air battery with buckypaper air cathode and sulfuric acid electrolyte.* Electrochemica Acta, 2012. **81**: p. 20-24.

36. Kan Huang, Y.L., Yangchuan Xing, *Increasing round trip efficiency of hybrid Li-air battery with bifunctional catalysts.* Electrochimica Acta, 2013. **103**: p. 44-49.

37. Y. Shimonishi, T.Z., P. Johnson, N. Imanishi, A. Hirano, Y. Takeda, O. Yamamoto, N. Sammes, *A study on lithium/air secondary batteries—stability of*

NASICON-type glass ceramics in acid solutions. Journal of Power Sources, 2010. **195**: p. 6187-6191.

38.   Longjun Li, Y.F., Arumugam Manthiram, *Imidazole-buffered acidic catholytes for hybrid Li–air batteries with high practical energy density.* Electrochemistry Communications, 2014. **47**: p. 67-70.

39.   Lide, D.R., *Handbook of chemistry and physics.* 84 ed. 2003.

40.   Jusef Hassoun, F.C., Michel Armand, Bruno Scrosati, *Investigation of the O2 electrochemistry in a polymer electrolyte solid-state cell.* Angewandte Chemie International Edition, 2011. **50**: p. 2999-3002.

41.   J.-F. Colin, V.P., V. Caignaert, M. Hervieu, B. Raveau, *A novel layered titanoniobate LiTiNbO5: topotactic synthesis and electrochemistry versus lithium.* Journal of Inorganic Chemistry, 2006. **45**: p. 7217-7223.

42.   Young Bok Kim, I.T.K., Myeong Jun Song, , *Poly-vinylidene-fluoride/p-benzoquinone gel polymer electrolyte with good performance by redox mediator effect for Li-air battery.* Electrochimica Acta, 2016. **210**: p. 821-828.

43.   Yusong Zhu , S.X., Yi Shi , Yaqiong Yang , Yuyang Hou ,and Yuping Wu, *A composite gel polymer electrolyte with high performance based on poly(vinylidene fluoride) and polyborate for lithium ion batteries.* Advance Energy Material, 2014. **4**(1300647): p. 1-9.

44.   Wei Zhai, H.-j.Z., Long Wang, Xiao-min Liu, Hui Yang, *Study of PVDF-HFP/PMMA blended micro-porous gel polymerelectrolyte incorporating ionic*

liquid [BMIM]BF4 for Lithium ion batteries. Electrochemica Acta, 2014. **133**: p. 623-630.

45.   Shoichi Matsuda, K.H., Shuji Nakanishi, *Efficient Li2O2 formation via aprotic oxygen reduction reaction mediated by quinone derivatives.* The Journal of Physical Chemistry C, 2014. **118**: p. 18397-18400.

46.   Maciej Gali´nski, A.L., Izabela St¸epniak, *Ionic liquid as electrolytes.* Electrochimica Acta, 2006. **51**(26): p. 5567-5580.

47.   K.N. Marsh, J.A.B., R. Lichtenthaler, *Room temperature ionic liquids and their mixtures—a review.* Fluid Phase Equilibria, 2004. **219**: p. 93-98.

48.   Takashi Kuboki, T.O., Takahisa Ohsaki, Norio Takami, *Lithium-air batteries using hydrophobic room temperature ionic liquid electrolyte.* Journal of Power Sources, 2005. **146**: p. 766-769.

49.   Shrihari Sankarasubramanian, J.S., FuminoriMizuno, Nikhilendra Singh, Kensuke Takechi, Jai Prakash, *Enhancement of oxygen reduction reaction rate by addition of water to an oxidatively stable ionic liquid electrolyte for lithium-air cells.* Electrochemistry Communications, 2016. **73**: p. 55-58.

50.   Ji-Guang Zhang, D.W., Wu Xu, Jie Xiao, R.E. Williford, *Ambient operation of Li/Air batteries.* Journal of Power Sources, 2010. **195**: p. 4332-4337.

51.   B. D. McCloskey, D.S.B., R. M. Shelby, G. Girishkumar, A. C. Luntz, *Solvents' critical role in nonaqueous lithium oxygen battery electrochemistry.* the Journal of Physical Chemistry Letters, 2011. **2**: p. 1161-1166.

52. LLC, A.N.P.C., *Ketjenblack EC-600JD powder.* Akzo Nobel Polymer Chemicals LLC.

53. Xiaoming Ren, S.S.Z., Dat T. Tran, Jeffrey Read, *Oxygen reduction reaction catalyst on lithium/air battery discharge performance.* Journal of Material Chemistry, 2011. **21**: p. 10118-10125.

54. Jie Xiao, D.W., Wu Xu, Deyu Wang, Ralph E. Williford, Jun Liu, and Ji-Guang Zhang, *Optimization of air electrode for Li/air batteries.* Journal of Electrochemical Society, 2010. **157**(4): p. A487-A492.

55. S. D. Beattie, D.M.M., S. L. Blair, *High-capacity lithium–air cathodes.* Journal of Electrochemical Society, 2009. **156**(1): p. A44-A47.

56. Lucas D. Griffith, A.E.S.S., John F. Mansfield, Donald J. Siegel, Charles W. Monroe, *Correlating Li/O2 cell capacity and product morphology with discharge current.* Journal of Applied Materials & Interfaces, 2015. **7**: p. 7670-7678.

57. P. Andrei, J.P.Z., M. Hendrickson, E. J. Plichta, *Some possible approaches for improving the energy density of Li-air batteries.* Journal of Electrochemical Society, 2010. **157**(12): p. A1287-A1295.

58. Ukrit Sahapatsombut, H.C., Keith Scott, *Modelling of electrolyte degradation and cycling behaviour in a lithiumeair battery.* Journal of Power Sources, 2013. **243**: p. 409-418.